Title

From Poison to Small-Molecule Probe: Cyanide Self-Assembly on Au{111} for the Development of Room-Temperature Single-Molecule Spectroscopy

Author

Guttentag, Andrew I.

Publication Date

2016

Peer reviewed|Thesis/dissertation

UNIVERSITY OF CALIFORNIA

Los Angeles

From Poison to Small-Molecule Probe: Cyanide Self-Assembly on Au{111} for the Development of Room-Temperature Single-Molecule Spectroscopy

A dissertation submitted in partial satisfaction of the

requirements for the degree Doctor of Philosophy

in Chemistry

by

Andrew Ira Guttentag

2016

ABSTRACT OF THE DISSERTATION

From Poison to Small-Molecule Probe: Cyanide Self-Assembly on Au{111} for the Development of Room-Temperature Single-Molecule Spectroscopy

by

Andrew Ira Guttentag

Doctor of Philosophy in Chemistry

University of California, Los Angeles, 2016

Professor Paul S. Weiss, Chair

Cyanide assembles on Au{111} providing a unique opportunity to understand the coupling between substrate electrons and molecular vibrations. Two factors, the strength of the substrate-molecule coupling and the favorable orientation of the molecular orbitals, directly influence the efficiency of electron transfer across a molecule to the substrate. Inelastic electron tunneling can probe molecule vibrations; the contributions to the tunneling current can be measured at with molecular resolution under ultrastable conditions using a scanning tunneling microscope. Molecular vibrations, most often probed using infrared or Raman spectroscopy,

encode chemical information pertaining to connectivity, composition, and geometry and can be used to monitor chemical reactions and to sense bonding changes due to the local environment. Predicted to have a vibrational resonance with the surface electronic states of gold, cyanide is an ideal small molecule to probe the interactions between electronic structure and vibrations. Exploiting well-known cyanide-gold coordination chemistry, I first characterize both the structural and vibrational properties of monolayers of cyanide on gold that are stable under ambient conditions and demonstrate that the substrate-molecule coupling of cyanide is particularly strong, leading to facile electron transfer between the molecules to the substrate. Following the characterization of the as-adsorbed cyanide system, I discuss how, through a simple thermal annealing process, I induce local electronic, chemical, and structural changes in the cyanide monolayer that can be identified through a blue shift of the C-N bond vibrational energy. Finally, I describe a prototype ambient scanning tunneling microscope that uses the multiplexed signals from Fourier transform infrared spectroscopy through rear illumination via attenuated total internal reflection to test whether the exponentially weighted tunneling current can detect single-molecule vibrations through an atomically sharp tip. This effort contributes to understanding the interactions between electronic structure and molecular vibrations through the use of cyanide coordination chemistry with the long-term goal of creating a generally applicable method of getting single-molecule chemical information while simultaneously acquiring, in space and time, the local environmental structure from the scanning tunneling microscope.

This dissertation of Andrew Ira Guttentag is approved.

Yung-Ya Lin

Yang Yang

Paul S. Weiss, Committee Chair

University of California, Los Angeles

2016

Table of Contents

List of Figures

List of Tables

List of Abbreviations and Symbols

2D	**2-dimensional**
3D	**3-dimensional**
A	**Amp**
Å	**Angström**
α, γ	**characteristic decay constants**
AES	**Auger electron spectroscopy**
AFM	**atomic force microscopy**
ATR	**attenuated total reflection**
Au	**gold**
C	**carbon**
C_2N_2	**cyanogen**
CaF_2	**calcium fluoride**
CHC	**core-hole clock**
cm	**centimeter**
cm^{-1}	**wavenumber**
CN	**cyanide**
CO	**carbon monoxide**
CO_2	**carbon dioxide**
COOH	**carboxylic acid**
CT	**charge transfer**

D	**Debye**
DFT	**density functional theory**
d_p	**penetration depth**
Dx	**change in distance**
E	**electric field**
E_B	**binding energy**
ET	**electron transfer**
eV	**electron volt**
FFT	**fast Fourier transform**
fs	**femtosecond**
FTIR	**Fourier transform infrared**
H	**height**
h	**hour**
H_2O	**water**
HCN	**hydrogen cyanide**
hcp	**hexagonal close-packed**
HeNe	**helium neon**
HRXPS	**high resolution X-ray photoelectron spectroscopy**
Hz	**hertz**
I	**electrical current**
IETS	**inelastic tunneling spectroscopy**
IR	**infrared**
K	**Kelvin**

KCN	**potassium cyanide**
L	**length**
MCT	**mercury cadmium telluride**
n	**index of refraction**
N_2	**nitrogen**
NC-CnHnS	**nitrile-terminated alkanethiolate of linear chain length n**
NEXAFS	**near edge X-ray absorption fine scattering**
nm	**nanometer**
NP	**nanoparticle**
NSOM	**near-field scanning optical microscopy**
O_2	**oxygen**
P	**participator**
pA	**picoamp**
PE	**potential energy**
PET	**participator electron emission time**
PM-IRRAS	**polarization modulation-infrared reflection-absorption spectroscopy**
Pt/Ir	**platinum/irridium**
θ	**incident angle**
θ_c	**critical angle**
RAES	**resonant Auger electron spectroscopy**
s	**second**
S	**sulfur**
SAM	**self-assembled monolayer**

Se	**selenium**
SERS	**surface-enhanced Raman spectroscopy**
SP	**spectator**
STM	**scanning tunneling microscope**
STS	**scanning tunneling microscopy**
TEM	**transmission electron microscopy**
TERS	**tip-enhanced Raman spectroscopy**
τ_{ET}	**electron transfer time**
τ_{core}	**core electron lifetime**
TIR	**total internal reflection**
V	**volt**
W	**width**
XPS	**X-ray photoelectron spectroscopy**
z	**tip-sample separation distance**
ZPD	**zero path difference**

Acknowledgments

The successful completion of my dissertation and subsequent graduation certify that I am now qualified to perform independent research. It has been a seven year roller coaster filled with many moments of doubt and, equally, many moments of satisfaction. As a physical chemistry graduate student I have learned how to persevere, to develop new skills, to accept that I am not always correct, and to listen with an open mind. These learning experiences have forged a strong foundation that I will continue to build upon as set forth on a new adventure as research scientist. Along this path there have been many influential people that have contributed to my successful scientific development.

First, I would like to thank Professor Paul Weiss for the mentorship that was critical to my successful graduate career. He provided insight into the world of academics, a vast amount of resources, and demanded that the generated science meet his high expectations. Though the process of working close with him, I have learned just how much work it takes to create a story that is worth telling. I was taught to think critically, to plan my experiments, and to focus on what we ultimately learn from our science. I also developed an addiction to espresso.

Next, I have to thank the members of the Weiss Group for scientific discussions, a competitive atmosphere that brings out your best, and great food. I am especially thankful for some of the relationships I developed when working some long days and late nights. In particular I would like to thank Dr. Huan Cao, Dr. Jeffrey Schwartz, Dr. Sarawut Cheunkar, Dr. Wei-Ssu Laio, Andrew Serino, John Abendroth, Dr. Liane Slaughter, and Dr. Xiaobin Xu for their support and friendship. I cannot forget to thank Kristopher Barr, who has contributed significantly to many aspects of the work presented in this dissertation, which will be continuing to advance these

projects. I look forward to his success in the future as his passion for science is only rivaled by his passion for Disney.

Now, I will thank of the other important UCLA contributors to my success. Shylo Stiteler, the Master Machinist from the Physics Student Machine Shop, who taught me how to use mills and lathes and to design the parts for my instruments. The instrument presented in Chapter 4 is a direct result of my working with him. I also must thank my committee for their support and advice, which includes Dr. Yung-Ya Lin, Dr. Kendall N. Houk, and Dr. Yang Yang. Dr. Tze-Bin Song, one of Dr. Yang Yang's graduates, was a significant contributor to the spectral results presented in Chapters 2 and 3.

Outside of UCLA, there are collaborators that I need to thank. I will start with Pennsylvania State University Professor David Allara and Heidelberg University Professor Michael Zharnikov along with their graduate students Nichole Sullivan (Penn State) and Tobias Wächter (Heidelberg) who were the inspiration, motivation, and significant contributors to the work pertaining to the self-assembly of cyanide on Au{111}. Helping me to understand Fourier transforms and image analysis is Dr. Jerome Gilles, now at San Diego State University, who helped significantly with the students of the REU program in the summer of 2015. The results of this mathematical analysis is presented in chapter 3 and the appendix.

Of course, I need to thank the relevant funding agencies for their support of my research. This includes the US Department of Energy Grant #DE-SC-1037004 for the resources pertaining to instrument development and the W.M. Keck Foundation for supporting the development of the relevant analytical methods. I also will thank the UCLA Department of Chemistry and Biochemistry for providing the opportunity to teach.

Finally, and most importantly, I need to thank my family – I would not have succeeded without their love and support. They include my brothers Kenneth and Mark who are my partners in crime, but also provide inspiration and compassion when the going gets tough. My mother, Myra, step-mother Linda, and father, Allan, who have to listen to my complaints and talk me out of making stupid decisions. I also thank my in-laws, Lonn and Carol Trost, who gave their support with confidence on the condition that I bleed pinstripes. Because of them, I am a New York Yankees fan for life. Most importantly, I thank my wife Audra who is the most tolerant person in the world, talked me out of quitting on numerous occasions, and is always there when I need someone the most. My daughters, Bryn and Brooklyn, are the most important things in my life, and I hope I can continue to show them, by example, that you can accomplish anything.

Co-author Contributions to Published Work Included in This Dissertation:

Chapter 2 is adapted from a manuscript submitted for publication:

Guttentag, A. I.; Wachter, T.; Barr, K. K.; Abendroth, J. M.; Song, T.-B.; Sullivan, N. F.; Yang, Y.; Zharnikov, M.; Allara, D. L.; Weiss, P. S. "Precious Poison: The Self-Assembly of Cyanide on Au{111}." *in preparation*, **2016**.

Andrew Guttentag developed the project in collaboration with, M. Zharnikov, D. L. Allara, and P. S. Weiss. Experiments were performed by A. I. Guttentag, K. K. Barr; J. M. Abendroth, N. Sullivan, and T.-B. Song. T. Wachter, M. Zharnikov, D. L. Allara performed the photoelectron spectroscopy and analysis for composition, orientation, and electron transfer efficiency. The manuscript was written by A. I. Guttentag with contributions from all co-authors. This work received financial support from the U.S. Department of Energy (DE-SC-0005025).

Chapter 3 is adapted from a manuscript submitted for publication:

Guttentag, A. I.; Barr, K. K.; Song, T.-B.; Bui, K. V.; Fauman, J. N.; Torres, L. F.; Kes, D. D.; Ciomaga, A.; Gilles, J.; Sullivan, N. F.; Yang, Y.; Zharnikov, M.;Allara, D. L.; Weiss, P. S. "Hexagons to Ribbons: Flipping Cyanide on Au{111}." *in preparation*, **2016**.

Andrew Guttentag initiated the projected and developed it in collaboration with all co-authors. J. Gilles, K. A. Ciomaga, Bui, J. Fauman, L. Torres, and D. Kes, performed the image analysis. The manuscript was written by A. I. Guttentag with contributions from all co-authors. This work received financial support from the US Department of Energy (DE-SC-0005025) and the Kavli Foundation.

VITA

Andrew Guttentag received his Bachelor of Science in Engineering degree in 2008 with an emphasis in biochemical engineering and computer science, summa cum laude, from Arizona State University. While at ASU, Andrew researched topics related to the role of the posterior parietal cortex in vision and movement where he helped to develop a virtual reality behavioral control system for monkeys under the mentorship of Dr. Christopher Buneo. Andrew continued his research in 2009 as part of the Motor Systems Laboratory at the Barrow Neurological Institute in Phoenix, Arizona under the mentorship of Dr. Irina Beloozerova and Dr. Trevor Rivers where he developed a rotation matrix algorithm modeling the gaze position of freely walking cats. In the fall of 2009, Andrew continued his academic training with Professor Paul S. Weiss, initially entering the Neuroscience doctorate program at The Pennsylvania State University. When the group moved to the University of Los Angeles, California in 2009, Andrew transferred to the Department of Chemistry and Biochemistry where he helped establish Professor Weiss' new nanoscience laboratory.

PUBLICATIONS

Rivers, T. J.; Sirota, M. G.; **Guttentag, A. I.**; Ogorodnikov, D. A.; Shah, N. A.; Beloozerova, I. N.; "Gaze Shifts and Fixations Dominate Gaze Behavior of Walking Cats." *Neuroscience*, **2014**; *275*: 477-479. doi: 10.1016/j.neuroscience.2014.06.034

Shuster, M. J.; Vaish, A.; Cao, H. H.; **Guttentag, A. I.**; McManigle, J. E.; Gibb, A. L.; Martinez, M. M.; Nezarati, R. M.; Hinds, J. M.; Liao, W.-S.; Weiss, P S; Andrews, A M; "Patterning Small-Molecule Biocapture Surfaces: Microcontact Insertion Printing vs. Photolithography." *Chemical Communications*, **2011**; *47(38)*: 10641-3. doi: 10.1039/C1CC13002A

Guttentag, A. I.; Wächter, T.; Barr, K. K.; Abendroth, J. M.; Song, T.-B.; Sullivan, N.; Yang Y.; Zharnikov, M.; Allara, D. L.; Weiss, P. S. "Precious Poison: The Self-Assembly of Cyanide on Au{111}." *in preparation*, **2016**.

Guttentag, A. I.; Barr, K. K.; Song, T.-B.; Bui, K.; Fauman, J.; Torres, L.; Kes, D.; Sullivan, N.; Ciomaga, A.; Gilles, J.; Zharnikov, M.;Allara, D. L.; Weiss, P. S. "Hexagons to Ribbons: Flipping Cyanide on Au{111}." *in preparation*, **2016**.

PROFESSIONAL PRESENTATIONS

UCLA Physical Chemistry Departmental Student Seminar, February 25, 2016
Department of Chemistry and California NanoSystems Institute, UCLA, Los Angeles, CA 90095, USA
From Poison to Small-Molecule Probe: Cyanide Self-Assembly for the Development of Room-Temperature Single-Molecule Spectroscopy

American Chemical Society Meeting, March 15, 2016
UCLA Showcase, Sunday 13 - Thursday 17 March 2016, San Diego, CA
Precious poison: The self-assembly of cyanide on Au{111}

American Chemical Society Meeting, March 16, 2016
Spring 2016, Surface Characterization & Manipulation for Electronic Applications Symposium, Sunday 13 - Thursday 17 March 2016, San Diego, CA
Precious poison: The self-assembly of cyanide on Au{111}

CHAPTER 1:

Probing Single Molecules:

Scanning Tunneling Microscopy and Molecular Vibrations

1.1 Motivation

Increasing the amount and type of single-molecule level information will advance the goal of nanotechnology to utilize molecules as building blocks and functional components in emerging new technologies. Through this generation of nanoscale information, nanoscientists and engineers will be able to work to manipulate and to fabricate new materials with unprecedented precision. There are three primary mechanisms by which we currently record single-molecule measurements (Figure 1.1), which are the subject of a recent Review. However, as described in the Review, many of these individual measurement methods have challenges that include, but are not limited to, strict sample preparation guidelines, ultrastable experimental conditions, reproducibility, and sometimes ambiguous interpretation of results.[1]

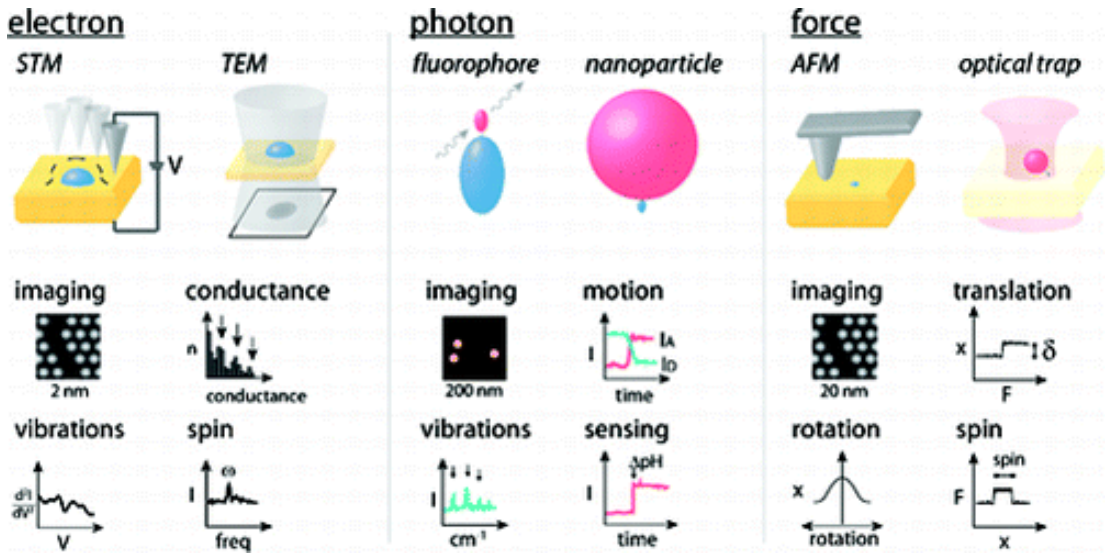

Figure 1.1. The three primary techniques for making single-molecule measurements and the type information they communicate. Adapted with permission from ref 1.

One way to overcome these challenges is by combining measurement techniques that exploit their individual strengths.[1-4] In particular, this dissertation will focus on scanning tunneling microscopy (STM), which has been combined with photons[2,4-7] and force-based[3,8] techniques aimed at taking advantage of the ability to achieve atomic resolution.[1,9] Some examples of the attempts to advance the capabilities of the STM to perform single-molecule measurements include ultrafast scanning,[10,11] the combination with atomic force microscopy (AFM),[3] tip-enhanced Raman spectroscopy (TERS),[12,13] near-field optical microscopy (NSOM),[2,14] and, recently, infrared spectroscopy (IR).[15] Scanning tunneling microscopy, as an independent measurement technique, is ideally suited for probing the electronic and topographic local chemical environment. The integration of additional modalities is aimed at advancing the STM by enabling it to elucidate more chemical information, such as the identity of molecules, at the single-molecule level.[16-18]

1.2 Scanning Tunneling Microscopy and Spectroscopy

The STM, shown in Figure 1.2, was invented by Binnig and Rohrer in 1981,[9] for which they won the Nobel Prize. It is the exponential dependence of the tunneling current generate when an atomically sharp metal tip is brought into close proximity to a metal surface that enables probing of single-molecule and atomic-scale events.[9,19] As an electron-based measurement, the STM is particularly well-suited to probing the electronic structure and changes induced by manipulating the local electronic environment.[1,4,20-23] The measured signal is not purely topographic, but a convolution with the measured electronic structure and can be interpreted as primarily a topographic mapping of the surface when the local density of states is relatively constant. There are two primary modes of operation implemented by control software, constant current – where the measured height of the STM probe tip is adjusted in response to current changes as it scans the

surface, and constant height – where only changes in the tunneling current are measured as a function of lateral position.[24,25] Ultimately, changes in tunneling current, which are on the order of 10^{-12} A, are amplified and converted to generate the microscope image of the surface.

Scanning tunneling spectroscopy (STS) is the primary mechanism by which the STM can generate chemical information pertaining to the molecules on the surface.[1,19,20,26-28] These spectroscopic measurements are typically based on measured contributions to the tunneling current while probing a single position or while scanning the surface.[29,30] Electron-spin measurements,[31,32] molecular conductance,[33-35] and molecular vibrations[22,27,30,36] are all types of chemical information accessible via STS. However, due to the effects of temperature, both, the stability and size, of the STM probe tip (i.e., thermal expansion will result in a loss of resolution) along with broadening of spectral features limits these types of measurements to cryogenic temperatures (~4 K) and ultrahigh vacuum conditions.[22] Inelastic tunneling spectroscopy (IETS), for example, which is a STM method to probe single-molecule vibrations,[30] has a resolution of ~5 cm^{-1} and a wavenumber range of 50–19,000 cm^{-1} that is on par with infrared, Raman, and electron energy loss spectroscopies.[22] However, there are still ambiguities with selection rules that require any changes to be normal to the surface, along with the need for the previously mentioned ultrastable conditions reduces its applicability a general tool.[19,22,27,36] It is the ultimate goal of the work presented in this dissertation to guide the way for developing more generally applicable, room temperature, single-molecule vibrational spectroscopy.

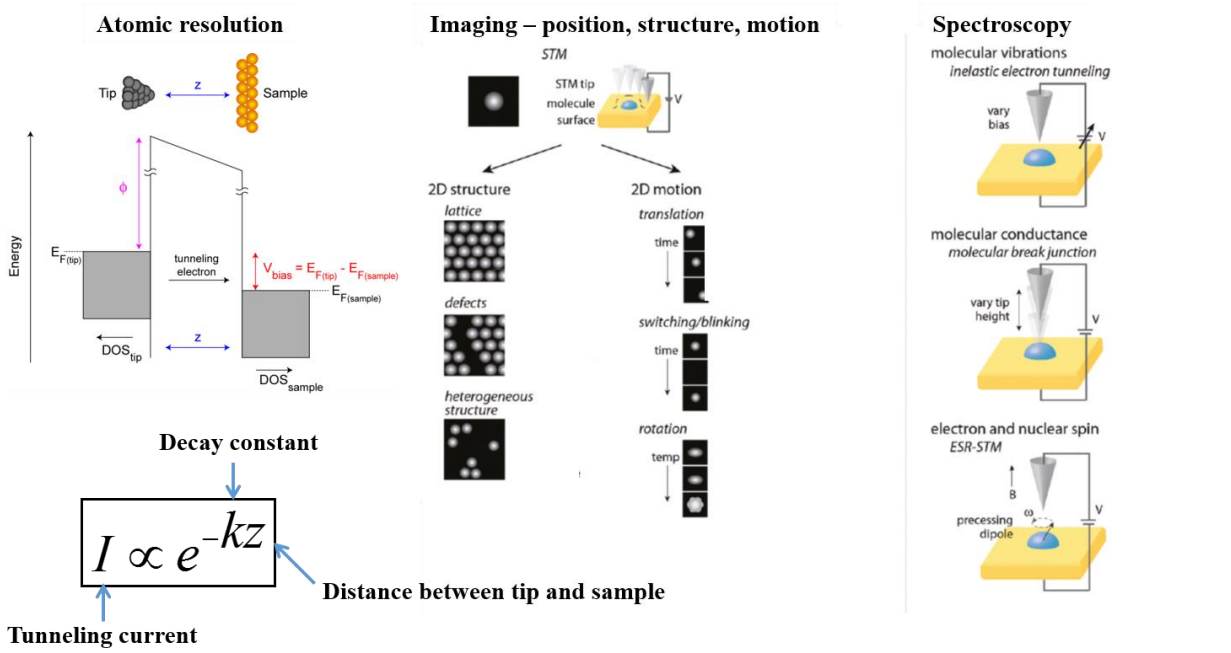

Figure 1.2. A description of scanning tunneling microscopy and spectroscopy. The exponential dependence of the tunneling current enables atomic resolution imaging of surface features. Manipulation of the local electronic environment can reveal chemical information from molecular vibrations, molecular conductance, and electron spin. Modified and adapted with permission from ref 1.

1.3 Molecular Vibrations

The frequency-encoded information contained in molecular vibrations is probed by two primary methods at room temperature, infrared and Raman spectroscopy. The activation of molecular vibrations occurs by two different mechanisms in these noninvasive forms of spectroscopy. In infrared spectroscopy, the activated vibrational modes are the result of direct absorption of a photon of the appropriate energy causing a change in the dipole moment of the molecule. Raman spectroscopy, in comparison, detects vibrations through the inelastic collision of

a photon with a molecule. The resulting vibrational modes are attributed to different modes of the molecules, which are directly influenced by the molecular composition and sensitive to changes in the local environment. Electron energy loss spectroscopy, in which electrons scatter inelastically from a surface with energy reduced by the value of vibrations, has three origins: phonon excitations, electronic excitations, and ionizations.[37] Thus, vibrational spectroscopy becomes a rich source of a variety of chemical information.[15,38-46]

1.3.1 Chemical Information

The chemical information found in molecular vibrations can be used to elucidate the chemical connectivity,[47,48] elemental composition,[43] structure,[40,41] and identity of molecular systems.[42,49] This type of information can be used to monitor chemical reaction,[44,45,50] analyze the function of molecules, and determine the composition of complex molecular assemblies.[43] For example, the function of azobenzene molecular switches was monitored on Au{111} using Raman spectroscopy.[44,45] Another example is the use of infrared spectroscopy to test whether a forbidden reaction of functionalized anthracene molecules occurred when tethered to a surface.[51] In a similar manner, the composition of mixed monolayers of alkanethiols and the effect of the length of carbon backbone was probed through vibrational spectroscopy.[52] Because of the sensitivity to the local chemical environment, knowledge of surface selection rules can be used with grazing angle infrared spectroscopy techniques to determine the orientation of the molecules with respect to a surface.[40,53] In addition to the information retrieved from probing these systems, molecular vibrations also interact with the molecular electronic structure.[22,36,54]

1.3.2 Interactions with Electronic Structure

Molecular vibrations, typically modeled as harmonic oscillators, interact with the electronic structure through the dipole moment and deformation of chemical bonds.[46,49,54] In this manner, molecular vibrations have also been shown to influence electron transport across molecules and even influence chemical reaction pathways.[54] The interactions between molecular vibrations and electronic surface states can affect both, the lifetime and intensity of activated vibrational modes.[54-56] As mentioned earlier, vibrational spectroscopies such as IETS that are performed by the STM, rely on the interaction between electronic structure and vibrations.[22,36] In addition to the fundamental vibrations probed by IR and Raman spectroscopies (100 to 4000 cm^{-1}), vibronics probes the interactions between visible and ultraviolet electromagnetic radiation (14,000 to 50,000 cm^{-1}) and combinations of vibrational and electronic transitions for information pertaining to the intensity of electronic transitions as described by the Franck-Condon Principle.

1.4 Self-Assembled Monolayers

Self-assembled monolayers (SAMs), in which a single layer of molecules is deposited and organizes on a surface, are a common platform for elucidating external influences on molecule structure and function.[17,18,51,53,57-59] The structure and chemistry of a monolayer is determined by the balance of interactions between a 'head' group that directly attaches to the substrate and the 'tail' groups of neighboring molecules. In the common alkanethiol monolayers on Au{111}, as shown in Figure 1.3, these groups are the sulfur 'head', which binds directly to the Au{111} substrate and a saturated hydrocarbon chain as the 'tail'. The balance of the intermolecular forces between the hydrocarbon chains and adsorbate-substrate interactions of the sulfur with the

Au{111} to maximize monolayer stability results in a 30° molecular tilt of the tail groups with respect to the surface along with surface features such as single-atom deep vacancy islands and domain boundaries.[17,57] In comparison, switching the molecular backbone from a linear chain to a bulkier, symmetrical group, such as in carboranethiols, will change the packing density, orientation with respect to the surface, and result in a more uniform, featureless monolayer.[60] Changing the head group,[61,62] including multiple attachment sites, or changing substrates, can also affect the monolayer structure, in some cases inducing molecules to lie down in order to maximize the interaction with the substrate.[57]

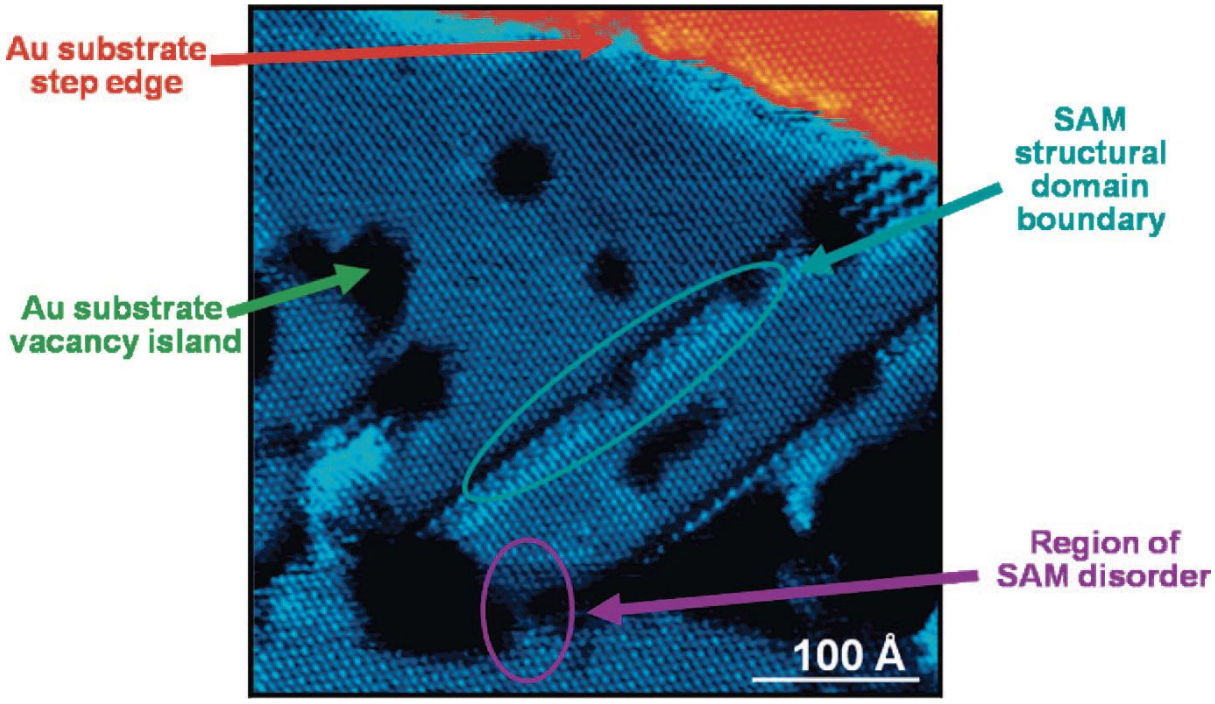

Figure 1.3. Molecular-resolution STM image of the surface features of a typical alkanethiol self-assembled monolayer on Au{111}. Adapted with permission from ref 17.

1.4.1 Isolating Single Molecules

Isolating single molecules in the defects of the monolayer matrix is one illustration where molecular design is important.[18,51,63,64] Surface features such as domain boundaries and single-molecule vacancies, defects in the monolayer, can serve as locations where individual molecules and assemblies can be inserted using the appropriate tethering chemistry and subsequently probed. In this way, single-molecule measurements are possible by positioning the STM probe tip over the molecule of interest and stimulating the molecule either through illumination, mechanical interaction, or the application of an electric field. The defect density and composition monolayer matrix can also be tailored by processing the film[18,57,65] to understand specific interactions such as the effect of hydrogen bonding, steric hindrance, and molecular surface density on molecule reactivity, structure, and function. Thus, rational molecular design can be used to probe and to manipulate the nanoscale environmental with applications that include patterning, sensing, and signal processing.

1.4.2 Molecular Transport Junctions

Molecules in self-assembled monolayers that stand off the surface and probed by the STM are in a configuration where they can be considered to be a molecular transport junction. In this configuration, it is possible to probe the environmental and structural effects on the transport of electrons across a molecule that bridges the two electrodes, the STM probe tip and metal substrate.[54] The geometry dependence on the conductance of molecules arranged in this manner have been demonstrated through the stochastic switching of conjugated phenyleneethynylene oligomers.[21] It was also demonstrated through the switching function of azobenzene molecules, that the composition of the molecule backbone, or 'molecular wire' in this configuration, is a

significant component that can modulate conductivity.[59] More recently, mixed monolayers of molecules with a strong dipole moment have been shown to modulate the band gap of a metal for use as a field-effect transistor.[60] Temperature also directly effects the spacing of energy levels, as demonstrated by the broadening of spectral lines in IETS, and influences molecular conduction efficiency, along with the small structural changes and heat generated by activated molecular vibrations.[22,54] Finally, molecular conductance can be adjusted by manipulating the Fermi level of the substrate through an applied voltage, which can result in a comparison between non-resonant (ground state) and resonant (excited state) electron transport.[54]

1.4.3 Substrate-Molecule Coupling

The immobilization of a molecule on the surface can significantly alter the function of the molecule in comparison to the behavior of the free molecule as found in solution or gas. In general, there are two primary mechanisms by which molecules can 'stick' to a surface. They can either be physisorbed (i.e, van der Waals interaction) or chemisorbed, where the latter requires a chemical reaction. For self-assembled monolayers, the typical point of attachment occurs through the 'head' group, which is a sulfur atom for the commonly used alkanethiol monolayer.[57,61] However, carbon,[62,66] selenium,[53,67-69] and nitrogen[70] are examples of other elements that have been used to tether molecules to a surface.

In all of these cases, the coupling between the molecule and the substrate play critical roles in determining molecular function,[59] mobility, position, and efficiency of charge transfer.[70] Quenching effects from gold substrates inhibit the emission from fluorophores and prevent photo-induced isomerization of switching molecules.[59] Weak substrate-mediated interactions have been shown to influence the rate and type of motion that benzene molecules exhibit on gold

surfaces.[71] Carbon monoxide adsorption onto silver is directly affected by the electronic environment of the substrate, preferentially adsorbing at the minima of the surface electronic standing wave pattern.[72] For electron transfer between a molecule and substrate, both the strength of the coupling between the molecule and substrate along with orientation of the molecular transport orbitals are crucial factors in determining efficiency.[69,70,73-75] In most cases, the interface between the molecule and substrate is buried and difficult to probe, requiring specialized techniques and well-known systems to elucidate key information.[76,77]

1.5 Small-Molecule Probes

Using small molecules with well-known structures and established chemical interactions is one strategy to probe buried interfaces and to understand the complex chemical interactions of larger molecular assemblies.[28,56,71,78-81] Carbon dioxide is one example of a small molecule that has been utilized extensively as a chemical probe.[56,72,80,82] It has been used to probe the interaction between a molecule and the surface electronic structure,[72] and to probe the effect of the surface on molecular vibrations at the single-molecule level.[79] Hydrogen and benzene have been used to demonstrate the ability of the STM to manipulate molecules.[83,84] The well-known structure of benzene has been used to probe the effects of adsorption on molecular structure,[85] motion,[71] and vibrations.[28] One challenge with small-molecule probes is that most of them desorb well below room temperature, limiting their application to cryogenic temperatures. Cyanide is a small molecule[86] with an established coordination chemistry with transition metals.[87-89] It has been utilized in the mining industry to purify gold from the raw ore and the coordination complexes with gold are stable at room temperature.[90] The stability of this complex along with the strong

dipole moment will be leveraged to fabricate stable monolayers at room temperature ideal for probing with vibrational spectroscopic techniques.[12,13,39,50,55,91]

1.6 Characterization

While scanning probe measurements and vibrational spectroscopies are commonly used to characterize self-assembled monolayers, photoelectron spectroscopic techniques can generate complementary information pertaining to composition, orientation, and electron transfer.[92-94] The techniques that are important to this work include X-ray photoelectron spectroscopy (XPS), near edge X-ray absorption fine scattering (NEXAFS), and Auger electron spectroscopy (AES). X-ray photoelectron spectroscopy is a surface sensitive technique that measures electron kinetic energy and number of electrons that are released after irradiating a sample with X-rays to generate information related to the elemental composition of a sample.[94,95] The second technique listed, NEXAFS, is a technique that is more sensitive to the chemical environment of the sample and can generate information pertaining to the fine structure of a molecule in addition to element-specific compositional information. In this technique, the electron beam energy is varied and not fixed as in XPS and the absorption of the X-rays in this technique is sensitive to the bonding environment. By varying the angle from normal to grazing and measuring the absorption coupled with information about the molecular orbitals, NEXAFS can yield information related to the orientation of the molecule.[92,96,97] Auger electron spectroscopy is another surface sensitive measurement technique that uses the relaxation pathways of electrons in an excited atom.[98] A specific method known as the core-hole-clock (CHC) technique quantitatively relates the resonant decay pathway to the non-resonant pathway to determine the speed of electron transfer between molecules in a

SAM to the substrate.[99,100] A combination of these techniques will be used to characterize cyanide self-assembly on Au{111} in chapter 3.

1.7 Perspective

Self-assembled monolayers are a platform to study and to probe nanoscale structures and processes in real time.[17,18,57] The self-assembly of cyanide on Au{111} at room temperature provides an unique platform to develop single-molecule vibration techniques. The combination of TERS and STM has already been explored utilizing the cyanide ion.[13] There is also the potential as a nanomaterial based on novel applications of cyanide coordination and polymerization chemistry.[101-103]

Molecular vibrations are one of the most chemically rich, noninvasive spectroscopic techniques enabling us to probe reaction pathways, elucidate chemical identity, and environmental influences on structure and function.[46,49] Combining vibrational spectroscopy with STM has already enabled probing these effects at the single-molecule level under ultrastable conditions.[22,36] To this end, an infrared scanning tunneling microscope that measures vibrations through thermal expansion has already been published.[15] It is crucial to make this more generally applicable by enabling single-molecule vibrational spectroscopy to be implemented at room temperature. The achievement of this capability will enable the advancement of "bottom-up" fabrication techniques and expand the ability to customize materials with single-molecule level precision.

1.8 Dissertation Overview

This dissertation is composed of five chapters that describe the structural and vibrational characterization, of an ideal system for the development of single-molecule vibrational spectroscopy at room temperature. Chapter 1 serves to provide the background and motivation for this work, describes the primary characterization techniques to probe structure and vibrations at the single-molecule level, and introduces nanoscale assemblies. Chapter 2 introduces the assembly of cyanide on Au{111}, characterizes the orientation and composition of the system, and communicates the strength of the substrate-adsorbate interaction from the efficiency of electron transfer between the cyanide and gold. Chapter 3 discusses the effect of temperature on the structure of the cyanide molecules on Au{111} through the 'flipping' of cyanide molecules through a simple dry annealing process. Chapter 4 then describes the integration of IR light with a horizontal coarse-approach STM in an attenuated total reflection (ATR) geometry that can simultaneously image and acquire vibrational spectra – a first step in testing whether the STM probe tip can detect molecular vibrations at room temperature. Chapter 5 then concludes the dissertation by summarizing the significant results and briefly discussing future prospects for this work.

1.9 References

1. Claridge, S. A.; Schwartz, J. J.; Weiss, P. S. Electrons, Photons, and Force: Quantitative Single-Molecule Measurements from Physics to Biology. *ACS Nano* **2011**, *5*, 693–729.

2. Grafström, S. Photoassisted Scanning Tunneling Microscopy. *J. Appl. Phys.* **2002**, *91*, 1717–1753.

3. Park, J. Y.; Maier, S.; Hendriksen, B.; Salmeron, M. Sensing Current and Forces with SPM. *Mater. Today* **2010**, *13*, 38–45.

4. Bonnell, D. A.; Basov, D. N.; Bode, M.; Diebold, U.; Kalinin, S. V.; Madhavan, V.; Novotny, L.; Salmeron, M.; Schwarz, U. D.; Weiss, P. S. Imaging Physical Phenomena with Local Probes: From Electrons to Photons. *Rev. Mod. Phys.* **2012**, *84*, 1343–1381.

5. Feldstein, M. J.; Vöhringer, P.; Wang, W.; Scherer, N. F. Femtosecond Optical Spectroscopy and Scanning Probe Microscopy. *J. Phys. Chem.* **1996**, *100*, 4739–4748.

6. Carmichael, E. S.; Ballard, J. B.; Lyding, J. W.; Gruebele, M. Frequency-Modulated, Single-Molecule Absorption Detected by Scanning Tunneling Microscopy. *J. Phys. Chem. C* **2007**, *111*, 3314–3321.

7. Mishra, P.; Komeda, T. Visualizing Optoelectronic Processes at the Nanoscale. *ACS Nano* **2015**, *9*, 10540–10544.

8. Braun, K. F.; Hla, S. W. Force Measurement with a Scanning Tunneling Microscope. *Phys. Rev. B* **2007**, *75*, 033406.

9. Chen, C. J. *Introduction to Scanning Tunneling Microscopy*. OUP Oxford: **2008**.

10. Weiss, S.; Botkin, D.; Ogletree, D. F.; Salmeron, M.; Chemla, D. S. The Ultrafast Response of a Scanning Tunneling Microscope. *physica status solidi (b)* **1995**, *188*, 343–359.

11. Steeves, G. M.; Elezzabi, A. Y.; Freeman, M. R. Advances in Picosecond Scanning Tunneling Microscopy via Junction Mixing. *Appl. Phys. Lett.* **1997**, *70*, 1909–1911.

12. Pettinger, B.; Picardi, G.; Schuster, R.; Ertl, G. Surface-Enhanced and STM Tip-Enhanced Raman Spectroscopy of CN^- Ions at Gold Surfaces. *J. Electroanal. Chem.* **2003**, *554–555*, 293–299.

13. Jiang, N.; Foley, E. T.; Klingsporn, J. M.; Sonntag, M. D.; Valley, N. A.; Dieringer, J. A.; Seideman, T.; Schatz, G. C.; Hersam, M. C.; Van Duyne, R. P. Observation of Multiple Vibrational Modes in Ultrahigh Vacuum Tip-Enhanced Raman Spectroscopy Combined with Molecular-Resolution Scanning Tunneling Microscopy. *Nano Letters* **2012**, *12*, 5061–5067.

14. Drezet, A.; Hohenau, A.; Krenn, J. R.; Brun, M.; Huant, S. Surface Plasmon Mediated Near-Field Imaging and Optical Addressing in Nanoscience. *Micron* **2007**, *38*, 427–437.

15. Pechenezhskiy, I. V.; Hong, X.; Nguyen, G. D.; Dahl, J. E. P.; Carlson, R. M. K.; Wang, F.; Crommie, M. F. Infrared Spectroscopy of Molecular Submonolayers on Surfaces by Infrared Scanning Tunneling Microscopy: Tetramantane on Au(111). *Phys. Rev. Lett.* **2013**, *111*, 126101.

16. Moore, A. M.; Weiss, P. S. Functional and Spectroscopic Measurements with Scanning Tunneling Microscopy. *Ann. Rev. Anal. Chem.* **2008**, *1*, 857–882.

17. Weiss, P. S. Functional Molecules and Assemblies in Controlled Environments: Formation and Measurements. *Acc. Chem. Res.* **2008**, *41*, 1772–1781.

18. Claridge, S. A.; Liao, W.-S.; Thomas, J. C.; Zhao, Y.; Cao, H. H.; Cheunkar, S.; Serino, A. C.; Andrews, A. M.; Weiss, P. S. From the Bottom Up: Dimensional Control and Characterization in Molecular Monolayers. *Chem. Soc. Rev.* **2013**, *42*, 2725–2745.

19. Stipe, B. C.; Rezaei, M. A.; Ho, W. Localization of Inelastic Tunneling and the Determination of Atomic-Scale Structure with Chemical Specificity. *Phys. Rev. Lett.* **1999**, *82*, 1724–1727.

20. Müller, F.; Müller, A.-D.; Meissner, O.; Heilmann, A.; Hietschold, M. Enhanced Local Surface Conductivity Measurements by Scanning Tunneling Microscopy. *Rev. Sci. Instrum.* **1997**, *68*, 3104–3107.

21. Donhauser, Z. J.; Mantooth, B. A.; Kelly, K. F.; Bumm, L. A.; Monnell, J. D.; Stapleton, J. J.; Price, D. W.; Rawlett, A. M.; Allara, D. L.; Tour, J. M.; Weiss, P. S. Conductance Switching in Single Molecules through Conformational Changes. *Science* **2001**, *292*, 2303–2307.

22. Hipps, K. W.; Mazur, U. Inelastic Electron Tunneling Spectroscopy. In *Handbook of Vibrational Spectroscopy*, John Wiley & Sons, Ltd: **2006**.

23. Moore, A. M.; Yeganeh, S.; Yao, Y.; Claridge, S. A.; Tour, J. M.; Ratner, M. A.; Weiss, P. S. Polarizabilities of Adsorbed and Assembled Molecules: Measuring the Conductance through Buried Contacts. *ACS Nano* **2010**, *4*, 7630–7636.

24. Bumm, L. A.; Arnold, J. J.; Charles, L. F.; Dunbar, T. D.; Allara, D. L.; Weiss, P. S. Directed Self-Assembly to Create Molecular Terraces with Molecularly Sharp Boundaries in Organic Monolayers. *J. Am. Chem. Soc.* **1999**, *121*, 8017–8021.

25. Mantooth, B. A. *Nanoscopic Analyses: Single Molecule Characterization in Molecular Electronics and Surface Science*. The Pennsylvania State University, University Park, PA **2004**.

26. Stipe, B. C.; Rezaei, M. A.; Ho, W.; Gao, S.; Persson, M.; Lundqvist, B. I. Single-Molecule Dissociation by Tunneling Electrons. *Phys. Rev. Lett.* **1997**, 78, 4410-4413.

27. Stipe, B. C.; Rezaei, M. A.; Ho, W. A Variable-Temperature Scanning Tunneling Microscope Capable of Single-Molecule Vibrational Spectroscopy. *Rev. Sci. Instrum.* **1999**, *70*, 137–143.

28. Pascual, J. I.; Jackiw, J. J.; Song, Z.; Weiss, P. S.; Conrad, H.; Rust, H. P. Adsorbate-Substrate Vibrational Modes of Benzene on Ag(110) Resolved with Scanning Tunneling Spectroscopy. *Phys. Rev. Lett.* **2001**, *86*, 1050–1053.

29. Kirtley, J.; Scalapino, D. J.; Hansma, P. K. Theory of Vibrational Mode Intensities in Inelastic Electron Tunneling Spectroscopy. *Phys. Rev. B* **1976**, *14*, 3177–3184.

30. Lorente, N.; Persson, M. Theory of Single Molecule Vibrational Spectroscopy and Microscopy. *Phys. Rev. Lett.* **2000**, *85*, 2997–3000.

31. Messina, P.; Sigalotti, P.; Lenci, L.; Prato, S.; Gatteschi, D. In *Construction of an ESR-STM for Single Molecular Based Magnets Anchored at Surfaces*, Nanotechnology, 2004. 4th IEEE Conference on, 16-19 Aug. 2004; **2004**; pp 642–644.

32. Balatsky, A. V.; Nishijima, M.; Manassen, Y. Electron Spin Resonance-Scanning Tunneling Microscopy. *Adv. Phys.* **2012**, *61*, 117–152.

33. Natelson, D. Mechanical Break Junctions: Enormous Information in a Nanoscale Package. *ACS Nano* **2012**, *6*, 2871–2876.

34. Xiang, D.; Jeong, H.; Lee, T.; Mayer, D. Mechanically Controllable Break Junctions for Molecular Electronics. *Adv. Mat.* **2013**, *25*, 4845–4867.

35. Florian, S.; Emanuel, L. Break-Junctions for Investigating Transport at the Molecular Scale. *J. Phys. Condens. Matter* **2014**, *26*, 474201.

36. Stipe, B. C.; Rezaei, M. A.; Ho, W. Single-Molecule Vibrational Spectroscopy and Microscopy. *Science* **1998**, *280*, 1732–1735.

37. Ibach, H.; Carette, J. D.; Feuerbacher, B.; Fitton, B.; Froitzheim, H.; Henzler, M.; Kirschner, J.; Roy, D. *Electron Spectroscopy for Surface Analysis*. Springer Berlin Heidelberg: **2012**.

38. Neelakantan, P. Raman Spectrum of Acetonitrile. *Proc. Indian Acad. Sci. - Sect. A* **1964**, *60*, 422–424.

39. Jobe, D. J.; Westaway, K. C. Fourier Transform Infrared Spectroscopy Studies of Cyanide Ion Solutions of Dimethylformamide and Aqueous Dimethylformamide. *Can. J. Chem.* **1993**, *71*, 1353–1361.

40. Hoffmann, H.; Mayer, U.; Brunner, H.; Krischanitz, A. Reflection-Absorption Infrared Spectroscopy of Self-Assembled Monolayers on Gold and Silicon Surfaces. *Vib. Spec.* **1995**, *8*, 151–157.

41. Hostetler, M. J.; Stokes, J. J.; Murray, R. W. Infrared Spectroscopy of Three-Dimensional Self-Assembled Monolayers: N-Alkanethiolate Monolayers on Gold Cluster Compounds. *Langmuir* **1996**, *12*, 3604–3612.

42. Max, P. B.; Scott, A. S.; Louis, J. A. The Infrared Spectra of Nitriles and Related Compounds Frozen in Ar and H_2O. *Astrophys. J* **1997**, *476*, 932.

43. Dunbar, T. D.; Cygan, M. T.; Bumm, L. A.; McCarty, G. S.; Burgin, T. P.; Reinerth, W. A.; Jones, L.; Jackiw, J. J.; Tour, J. M.; Weiss, P. S.; Allara, D. L. Combined Scanning Tunneling Microscopy and Infrared Spectroscopic Characterization of Mixed Surface Assemblies of Linear Conjugated Guest Molecules in Host Alkanethiolate Monolayers on Gold. *J. Phys. Chem. B.* **2000**, *104*, 4880–4893.

44. Zheng, Y. B.; Payton, J. L.; Chung, C.-H.; Liu, R.; Cheunkar, S.; Pathem, B. K.; Yang, Y.; Jensen, L.; Weiss, P. S. Surface-Enhanced Raman Spectroscopy to Probe Reversibly Photoswitchable Azobenzene in Controlled Nanoscale Environments. *Nano Lett.* **2011**, *11*, 3447–3452.

45. Zheng, Y. B.; Payton, J. L.; Song, T.-B.; Pathem, B. K.; Zhao, Y.; Ma, H.; Yang, Y.; Jensen, L.; Jen, A. K. Y.; Weiss, P. S. Surface-Enhanced Raman Spectroscopy To Probe Photoreaction Pathways and Kinetics of Isolated Reactants on Surfaces: Flat versus Curved Substrates. *Nano Letters* **2012**, *12*, 5362–5368.

46. Elliott, A. B. S.; Horvath, R.; Gordon, K. C. Vibrational Spectroscopy as a Probe of Molecule-Based Devices. *Chem. Soc. Rev.* **2012**, *41*, 1929–1946.

47. Gao, P.; Weaver, M. J. Metal-Adsorbate Vibrational Frequencies as a Probe of Surface Bonding: Halides and Pseudohalides at Gold Electrodes. *J. Phys. Chem.* **1986**, *90*, 4057–4063.

48. Bowmaker, G. A.; Kennedy, B. J.; Reid, J. C. Crystal Structures of AuCN and AgCN and Vibrational Spectroscopic Studies of AuCN, AgCN, and CuCN. *Inorg. Chem.* **1998**, *37*, 3968–3974.

49. Siebert, F.; Hildebrandt, P. *Vibrational Spectroscopy in Life Science*. Wiley: **2008**.

50. Senapati, D.; Dasary, S. S. R.; Singh, A. K.; Senapati, T.; Yu, H.; Ray, P. C. A Label-Free Gold-Nanoparticle-Based SERS Assay for Direct Cyanide Detection at the Parts-per-Trillion Level. *Chem. Eur. J.* **2011**, *17*, 8445–8451.

51. Kim, M.; Hohman, J. N.; Cao, Y.; Houk, K. N.; Ma, H.; Jen, A. K.-Y.; Weiss, P. S. Creating Favorable Geometries for Directing Organic Photoreactions in Alkanethiolate Monolayers. *Science* **2011**, *331*, 1312–1315.

52. Rosenbaum, A. W.; Freedman, M. A.; Darling, S. B.; Popova, I.; Sibener, S. J. Surface Vibrations in Alkanethiol Self-Assembled Monolayers of Varying Chain Length. *J. Chem. Phys.* **2004**, *120*, 3880–3886.

53. Hohman, J. N.; Kim, M.; Schüpbach, B.; Kind, M.; Thomas, J. C.; Terfort, A.; Weiss, P. S. Dynamic Double Lattice of 1-Adamantaneselenolate Self-Assembled Monolayers on Au{111}. *J. Am. Chem. Soc.* **2011**, *133*, 19422–19431.

54. Michael, G.; Mark, A. R.; Abraham, N. Molecular Transport Junctions: Vibrational Effects. *J. Phys.: Condens. Matter* **2007**, *19*, 103201.

55. Kunimatsu, K.; Seki, H.; Golden, W. G.; Gordon, J. G.; Philpott, M. R. A Study of the Gold/Cyanide Solution Interface by In Situ Polarization-Modulated Fourier Transform Infrared Reflection Absorption Spectroscopy. *Langmuir* **1988**, *4*, 337–341.

56. Forsblom, M.; Persson, M. Vibrational Lifetimes of Cyanide and Carbon Monoxide on Noble and Transition Metal Surfaces. *J. Chem. Phys.* **2007**, *127*, 154303.

57. Love, J. C.; Estroff, L. A.; Kriebel, J. K.; Nuzzo, R. G.; Whitesides, G. M. Self-Assembled Monolayers of Thiolates on Metals as a Form of Nanotechnology. *Chem. Rev.* **2005**, *105*, 1103–1170.

58. Shuster, M. J.; Vaish, A.; Gilbert, M. L.; Martinez-Rivera, M.; Nezarati, R. M.; Weiss, P. S.; Andrews, A. M. Comparison of Oligo(ethylene glycol)alkanethiols versus n-Alkanethiols: Self-Assembly, Insertion, and Functionalization. *J. Phys. Chem. C* **2011**, *115*, 24778–24787.

59. Pathem, B. K.; Claridge, S. A.; Zheng, Y. B.; Weiss, P. S. Molecular Switches and Motors on Surfaces. *Ann. Rev. Phys. Chem.* **2013**, *64*, 605–630.

60. Kim, J.; Rim, Y. S.; Liu, Y.; Serino, A. C.; Thomas, J. C.; Chen, H.; Yang, Y.; Weiss, P. S. Interface Control in Organic Electronics Using Mixed Monolayers of Carboranethiol Isomers. *Nano Lett.* **2014**, *14*, 2946–2951.

61. Hakkinen, H. The Gold-Sulfur Interface at the Nanoscale. *Nat. Chem.* **2012**, *4*, 443–455.

62. Crudden, C. M.; Horton, J. H.; Ebralidze, I. I.; Zenkina, O. V.; McLean, A. B.; Drevniok, B.; She, Z.; Kraatz, H.-B.; Mosey, N. J.; Seki, T.; Keske, E. C.; Leake, J. D.; Rousina-Webb, A.; Wu, G. Ultra Stable Self-Assembled Monolayers of N-Heterocyclic Carbenes on Gold. *Nat Chem* **2014**, *6*, 409–414.

63. Bumm, L. A.; Arnold, J. J.; Cygan, M. T.; Dunbar, T. D.; Burgin, T. P.; Jones, L.; Allara, D. L.; Tour, J. M.; Weiss, P. S. Are Single Molecular Wires Conducting? *Science* **1996**, *271*, 1705–1707.

64. Cygan, M. T.; Dunbar, T. D.; Arnold, J. J.; Bumm, L. A.; Shedlock, N. F.; Burgin, T. P.; Jones, L.; Allara, D. L.; Tour, J. M.; Weiss, P. S. Insertion, Conductivity, and Structures of Conjugated Organic Oligomers in Self-Assembled Alkanethiol Monolayers on Au{111}. *J. Am. Chem. Soc.* **1998**, *120*, 2721–2732.

65. Weiss, P. S.; Yokota, H.; Aebersold, R.; Engh, G. v. d.; Bumm, L. A.; Arnold, J. J.; Dunbar, T. D.; Allara, D. L. Creating, Tailoring and Using One-Dimensional Interfaces in Two-Dimensional Films. *J. Phys. Condens. Matter* **1998**, *10*, 7703.

66. Joo, S.-W.; Kim, W.-J.; Yun, W. S.; Hwang, S.; Choi, I. S. Binding of Aromatic Isocyanides on Gold Nanoparticle Surfaces Investigated by Surface-Enhanced Raman Scattering. *App. Spec.* **2004**, *58*, 218–223.

67. Monnell, J. D.; Stapleton, J. J.; Jackiw, J. J.; Dunbar, T.; Reinerth, W. A.; Dirk, S. M.; Tour, J. M.; Allara, D. L.; Weiss, P. S. Ordered Local Domain Structures of Decaneselenolate and Dodecaneselenolate Monolayers on Au{111}. *J. Phys. Chem. B.* **2004**, *108*, 9834–9841.

68. Monnell, J. D.; Stapleton, J. J.; Dirk, S. M.; Reinerth, W. A.; Tour, J. M.; Allara, D. L.; Weiss, P. S. Relative Conductances of Alkaneselenolate and Alkanethiolate Monolayers on Au{111}. *J. Phys. Chem. B* **2005**, *109*, 20343–20349.

69. Ossowski, J.; Wächter, T.; Silies, L.; Kind, M.; Noworolska, A.; Blobner, F.; Gnatek, D.; Rysz, J.; Bolte, M.; Feulner, P.; Terfort, A.; Cyganik, P.; Zharnikov, M. Thiolate versus Selenolate: Structure, Stability, and Charge Transfer Properties. *ACS Nano* **2015**, *9*, 4508–4526.

70. Zangmeister, C. D.; Robey, S. W.; van Zee, R. D.; Kushmerick, J. G.; Naciri, J.; Yao, Y.; Tour, J. M.; Varughese, B.; Xu, B.; Reutt-Robey, J. E. Fermi Level Alignment in Self-Assembled Molecular Layers: The Effect of Coupling Chemistry. *J. Phys. Chem. B* **2006**, *110*, 17138–17144.

71. Mantooth, B. A.; Sykes, E. C. H.; Han, P.; Moore, A. M.; Donhauser, Z. J.; Crespi, V. H.; Weiss, P. S. Analyzing the Motion of Benzene on Au{111}: Single Molecule Statistics from Scanning Probe Images. *J. Phys. Chem. C* **2007**, *111*, 6167–6182.

72. Kulawik, M.; Rust, H. P.; Heyde, M.; Nilius, N.; Mantooth, B. A.; Weiss, P. S.; Freund, H. J. Interaction of CO Molecules with Surface State Electrons on Ag(111). *Surf. Sci.* **2005**, *590*, L253–L258.

73. Schnadt, J.; Bruhwiler, P. A.; Patthey, L.; O'Shea, J. N.; Sodergren, S.; Odelius, M.; Ahuja, R.; Karis, O.; Bassler, M.; Persson, P.; Siegbahn, H.; Lunell, S.; Martensson, N. Experimental Evidence for Sub-3-fs Charge Transfer from an Aromatic Adsorbate to a Semiconductor. *Nature* **2002**, *418*, 620–623.

74. Neppl, S.; Bauer, U.; Menzel, D.; Feulner, P.; Shaporenko, A.; Zharnikov, M.; Kao, P.; Allara, D. L. Charge Transfer Dynamics in Self-Assembled Monomolecular Films. *Chem. Phys. Lett.* **2007**, *447*, 227–231.

75. Hamoudi, H.; Neppl, S.; Kao, P.; Schüpbach, B.; Feulner, P.; Terfort, A.; Allara, D.; Zharnikov, M. Orbital-Dependent Charge Transfer Dynamics in Conjugated Self-Assembled Monolayers. *Phys. Rev. Lett.* **2011**, *107*, 027801.

76. Han, P.; Kurland, A. R.; Giordano, A. N.; Nanayakkara, S. U.; Blake, M. M.; Pochas, C. M.; Weiss, P. S. Heads and Tails: Simultaneous Exposed and Buried Interface Imaging of Monolayers. *ACS Nano* **2009**, *3*, 3115–3121.

77. Thomas, J. C.; Schwartz, J. J.; Hohman, J. N.; Claridge, S. A.; Auluck, H. S.; Serino, A. C.; Spokoyny, A. M.; Tran, G.; Kelly, K. F.; Mirkin, C. A.; Gilles, J.; Osher, S. J.; Weiss, P. S. Defect-Tolerant Aligned Dipoles within Two-Dimensional Plastic Lattices. *ACS Nano* **2015**, 9, 4734–4742.

78. McCarley, R. L.; Bard, A. J. Surface Reactions of Gold(111) with Aqueous Cyanide Studied by Scanning Tunneling Microscopy. *J. Phys. Chem.* **1992**, *96*, 7410–7416.

79. Lauhon, L. J.; Ho, W. Single-Molecule Vibrational Spectroscopy and Microscopy: CO on Cu(001) and Cu(110). *Phys. Rev. B* **1999**, *60*, R8525–R8528.

80. Treesukol, P.; Limtrakul, J.; Truong, T. N. Adsorption of Nitrogen Monoxide and Carbon Monoxide on Copper-Exchanged ZSM-5: A Cluster and Embedded Cluster Study. *J. Phys. Chem. B* **2001**, *105*, 2421–2428.

81. Han, P.; Sykes, E. C. H.; Pearl, T. P.; Weiss, P. S. A Comparative Scanning Tunneling Microscopy Study of Physisorbed Linear Quadrupolar Molecules: C_2N_2 and CS_2 on Au{111} at 4 K. *J. Phys. Chem. A* **2003**, *107*, 8124–8129.

82. Piccolo, L.; Loffreda, D.; Cadete Santos Aires, F. J.; Deranlot, C.; Jugnet, Y.; Sautet, P.; Bertolini, J. C. The Adsorption of CO on Au(1 1 1) at Elevated Pressures studied by STM, RAIRS and DFT calculations. *Surf. Sci.* **2004**, *566–568, Part 2*, 995–1000.

83. Weiss, P. S.; Eigler, D. M. What is Underneath? Moving Atoms and Molecules to Find out. In *Nanosources and Manipulation of Atoms Under High Fields and Temperatures: Applications*, Binh, V. T.; Garcia, N.; Dransfeld, K., Eds. Springer Netherlands: Dordrecht, **1993**; pp 213–217.

84. Fernández-Torres, L. C.; Sykes, E. C. H.; Nanayakkara, S. U.; Weiss, P. S. Dynamics and Spectroscopy of Hydrogen Atoms on Pd{111}. *J. Phys. Chem. B* **2006**, *110*, 7380–7384.

85. Weiss, P. S.; Eigler, D. M. Site Dependence of the Apparent Shape of a Molecule in Scanning Tunneling Micoscope Images: Benzene on Pt{111}. *Phys. Rev. Let.* **1993**, *71*, 3139–3142.

86. Keedy, C. R. The Rotational-Vibrational Spectra of HCN and DCN: A Physical Chemistry Experiment. *J. Chem. Educ.* **1992**, *69*, A296.

87. Iguchi, K. Dipole Moment of the HCN Molecule. *J. Chem. Phys.* **1956**, *25*, 217–219.

88. Sun, L.; Crooks, R. M. Indirect Visualization of Defect Structures Contained within Self-Assembled Organomercaptan Monolayers: Combined Use of Electrochemistry and Scanning Tunneling Microscopy. *Langmuir* **1993**, *9*, 1951-1954.

89. Snyders, C. A.; Bradshaw, S. M.; Akdogan, G.; Eksteen, J. J. The Effect of Temperature, Cyanide and Base Metals on the Adsorption of Pt, Pd and Au onto Activated Carbon. *Hydrometallurgy* **2014**, *149*, 132–142.

90. van Deventer, J. S. J.; van der Merwe, P. F. The Effect of Temperature on the Desorption of Gold Cyanide from Activated Carbon. *Thermochim. Acta* **1993**, *221*, 99–113.

91. Beltramo, G. L.; Shubina, T. E.; Mitchell, S. J.; Koper, M. T. M. Cyanide Adsorption on Gold Electrodes: A Combined Surface Enhanced Raman Spectroscopy and Density Functional Theory Study. *J. Electroanal. Chem.* **2004**, *563*, 111–120.

92. Moulder, J. F.; Chastain, J. *Handbook of X-ray Photoelectron Spectroscopy: A Reference Book of Standard Spectra for Identification and Interpretation of XPS Data*. Physical Electronics Division, Perkin-Elmer Corporation: **1992**.

93. Heister, K.; Zharnikov, M.; Grunze, M.; Johansson, L. S. O.; Ulman, A. Characterization of X-ray Induced Damage in Alkanethiolate Monolayers by High-Resolution Photoelectron Spectroscopy. *Langmuir* **2001**, *17*, 8–11.

94. Ratner, B. D.; Castner, D. G. Electron Spectroscopy for Chemical Analysis. In *Surface Analysis – The Principal Techniques*, John Wiley & Sons, Ltd: **2009**; pp 47–112.

95. Zharnikov, M. High-Resolution X-Ray Photoelectron Spectroscopy in Studies of Self-Assembled Organic Monolayers. *J. Electron. Spectrosc. Relat. Phenom.* **2010**, *178–179*, 380–393.

96. Stöhr, J. *NEXAFS Spectroscopy*. Springer: **1992**.

97. Kempgens, B.; Kivimäki, A.; Neeb, M.; Köppe, H. M.; Bradshaw, A. M.; Feldhaus, J. A High-Resolution N 1s Photoionization Study of the Molecule in the Near-Threshold Region. *J. Phys. B At., Mol., Opt.* **1996**, *29*, 5389.

98. Piancastelli, M. N. Auger Resonant Raman Studies of Atoms and Molecules. *J. Electron. Spectrosc. Relat. Phenom.* **2000**, *107*, 1–26.

99. Kao, P.; Neppl, S.; Feulner, P.; Allara, D. L.; Zharnikov, M. Charge Transfer Time in Alkanethiolate Self-Assembled Monolayers via Resonant Auger Electron Spectroscopy. *J. Phys. Chem. C* **2010**, *114*, 13766–13773.

100. Zharnikov, M. Probing Charge Transfer Dynamics in Self-Assembled Monolayers by Core Hole Clock Approach. *J. Electron. Spectrosc. Relat. Phenom.* **2015**, *200*, 160–173.

101. Ahmad, S. The Chemistry of Cyano Complexes of Gold(I) with Emphasis on the Ligand Scrambling Reactions. *Coord. Chem. Rev.* **2004**, *248*, 231–243.

102. Katz, M. J.; Sakai, K.; Leznoff, D. B. The Use of Aurophilic and Other Metal-Metal Interactions as Crystal Engineering Design Elements to Increase Structural Dimensionality. *Chem. Soc. Rev.* **2008**, *37*, 1884–1895.

103. Li, R.; Kobayashi, H.; Tong, J.; Yan, X.; Tang, Y.; Zou, S.; Jin, J.; Yi, W.; Fan, J. Radical-Involved Photosynthesis of AuCN Oligomers from Au Nanoparticles and Acetonitrile. *J. Am. Chem. Soc.* **2012**, *134*, 18286–18294.

CHAPTER 2:

Precious Poison:

The Self-Assembly of Cyanide on Au{111}

2.1 Introduction

A central theme in nanotechnology is to be able to understand and to manipulate materials at the single-molecule level to advance current technologies and to create new technologies. Self-assembled monolayers, in which a single layer of molecules are immobilized on a surface, have often served as platforms for probing the effects of the local environment on molecular structure and function as well as for the development of new materials with distinct physical and chemical properties.[1-8]

Adsorbate-substrate interactions due to immobilization on surfaces strongly influence the function, dynamics, structure, and electronic properties of molecules in SAMs.[9-12] In some cases, as we have demonstrated in our previous work, we can tune the monolayer matrix defect density to affect the function and/or reactivity of molecules that have been tethered to surfaces.[13-18] In other cases, the functional group has been decoupled from the surface through molecular 'spacers' to avoid substrate quenching effects from efficient electron transfer.[13,19] Along with affecting electron transport, coupling between the surface electronic structure and molecular vibrations has been observed to enhance the lifetimes and intensities of vibrational modes.[20,21]

Two primary factors, the strength of the electronic coupling between an adsorbed molecule and substrate and the orientation of the molecular orbitals used during transport directly influence how efficiently an electron is transmitted between molecules to the substrate in SAMs.[22-27] To this end, electron conductance through nitrile-terminated alkanethiol SAMs have been measured to follow an exponential dependence on molecule length with a characteristic decay rate through the application of the core-hole clock method in resonant Auger electron spectroscopy (RAES).[25,28,29] These results have shown that inclusion of a four-carbon backbone results in approximately 100× lower efficiency for transferring electrons to the Au{111} substrate with average times of ~100 fs

when compared with the ~2.5 fs transfer time across only the thiolate head group.[30] These data are consistent with other measures of contact conductance.[23,24,26,31] The results presented in this work represent the extreme case where the sulfur and carbon backbone are entirely removed and only the nitrile functional group is bound to the Au{111} surface.

Often, the substrate-molecule interface is buried and difficult to probe, requiring special techniques that leverage the well-known chemistry and relatively simple structure of small-molecule probes. One such small molecule is CO, which has been used to elucidate the effect of binding sites on adsorbate vibrational modes.[32] Nevertheless, in the case of CO, as with many small molecules that desorb from surfaces well below room temperature, the ambient environment applications are limited. An established coordination chemistry between cyanide and gold[33] has already been leveraged to elucidate the prevalent chemistry, and structure of defects in alkanethiol monolayers,[34,35] to assemble metal-molecule coordination polymers,[36,37] and to probe covalent bond formation between gold atoms,[38] in addition to a component in the fabrication/or synthesis of conductive carbon nitride nanomaterials.[39] The coordination complexes formed between cyanide and gold are stable at room temperature. Our previous attempts to assemble CN on Au{111} failed when cyanogen, C_2N_2, did not dissociate under the conditions used.[40] In recent work, we have shown that processing the following as described here, we can also create monolayers and mixed orientations.(*in preparation*) Isocyanide[41] and carbene[42] systems have already demonstrated the potential for room temperature self-assembly using Au-C as an alternative to the Au-S bond characterizing thiol systems.

In this paper, we report the direct observation of the formation of a cyanide SAM on Au{111} under ambient conditions and probe the strength of the Au-CN coupling. Cyanide assembles into a highly ordered, stable, upright monolayer on Au{111} through the formation of a Au–C bond,

most likely due to the known gold cyanidation reaction,[43] with a similar surface structure to that observed in SAMs of alkanethiols.[4,5,44] Electron-transfer dynamics are measured by RAES using the core-hole clock method and indicate facile transfer from molecule to the Au{111} substrate. We conclude by discussing electronic, vibration, and structural properties as they relate to substrate-molecule coupling strength and future prospects for the CN/Au{111} system as a platform to study the interactions between molecular vibrations and electronic structure.

2.2 Experimental Methods

A Au{111}/mica substrate (150 nm of Au{111}, Agilent Technologies, Santa Clara, CA) is hydrogen flame annealed as described previously to clean the surface and to increase the size of the atomically flat terraces.[4,45] Monolayers of cyanide were prepared for the scanning tunneling microscope (STM) by placing 0.1 mg of solid KCN (≥96%, Sigma Aldrich, St. Louis, MO), without any further purification or treatment, in a glass vial with the Au{111}/mica substrate for 24 h at room temperature. **Caution: KCN is highly toxic and produces the volatile and flammable HCN(*g*) when it reacts with water and oxygen. It should be used with proper personal protective equipment, in a fume hood, and kept out of extreme temperatures.** Afterwards, the Au{111}/mica substrate was removed from the vial with the KCN and allowed to rest in the fume hood for 1 h before being placed in the STM for imaging.

A custom-built, beetle-style STM was used under ambient conditions. All STM images were calibrated against known references: gold step edges for height and a decanethiol on Au{111} SAM matrix for lateral distance measurements. All analyses on STM images were performed using custom software and Matlab.[46,47]

Infrared (IR) spectra was collected using a Thermo-Fisher Nicolet 8700 Interferometer (Thermo-Fisher Scientific, Waltham, MA), and the packaged OMNIC Software (Thermo-Fisher Scientific). The OMNIC software was also used for processing the spectra and identifying peak positions. All samples used for IR measurements were incubated with KCN in the same manner as described for the STM samples. For collecting IR spectra on Au{111} we used custom-made Au{111}/sapphire prism substrates. Prism substrates were 0.5 cm radius, 1 cm height c-cut sapphire half-cylinders with a 2-nm-thick Nb adhesion layer deposited at 0.11 Å/s and a 40-nm-thick layer of Au, which is well below the accepted optical penetration depth for metals in the range of the IR frequencies of interest,[48] deposited at a rate of 0.5 Å/s. A bare Au{111}/sapphire prism sample was used for the background spectrum and an incident angle $\theta = 60° > \theta_c = 34.6°$ as measured from normal to the surface (critical angle calculated using n=1.76 and Snell's Law, $\theta_c = \sin^{-1}(1/n)$).[48] After incubation, both STM and IR samples were directly analyzed without rinsing.

Surface-enhanced Raman spectroscopy (SERS) was performed on a Renishaw confocal Raman microscope (Renishaw, Inc., Hoffman Estates, Illinois) configured with a laser at 514 nm wavelength, using WiRE 3.2 (Renishaw, Inc.) for spectra processing and analysis. Two substrates designed for surface enhancement were used in this work: Au{111}/mica with nanohole arrays and nanostructured Au on glass. The nanohole arrays (175 nm diameter, 300 nm periodicity) on Au{111}/mica were fabricated using a focused ion beam.[49] The nanostructured Au on glass substrates were made by evaporating 50-Å-thick Au at 1 Å/s onto a glass slide and annealing at 400 °C for 24 h. All the SERS substrates were annealed and incubated in the same manner as the STM/IR samples.

The samples were characterized by synchrotron-based XPS, angle-resolved NEXAFS spectroscopy, and RAES. The measurements were performed at room temperature and under ultrahigh vacuum conditions (base pressure < 1.5×10^{-9} mbar). The spectral acquisition time at a particular sample spot was kept sufficiently short to avoid possible damage by the primary X-rays occurring during the measurements.[50,51]

The experiments were performed at the HE-SGM beamline (bending magnet) of the synchrotron storage ring BESSY II in Berlin, Germany and at the D1011 beamline (bending magnet, plane grating monochromator) of the MAX II storage ring at the MAX-IV laboratory in Lund, Sweden. The experimental stations at both facilities were equipped with a Scienta electron energy analyzer (R3000 at HE-SGM and SES200 at D1011) and a partial electron yield (PEY) detector. All experimental adjustments were exactly the same at both beamlines, except for somewhat better energy resolution at D1011 (~70 meV vs. ~0.3 eV at HESGM) and a minor difference in the polarization factor of the primary X-ray light, viz. 91% at HESGM and 95% at D1011. The experiments were repeated several times with the same results within experimental error. Independent sets of samples were used.

X-ray photoelectron spectra were recorded with a normal emission geometry at excitation energies of 350 and 580 eV. Synchotron light was used as the primary X-ray source. The binding energy (E_B) scale of the spectra was referenced to the Au $4f_{7/2}$ peak at a E_B = 84.0 eV.[52] The spectra were fit by symmetric Voigt functions and a Shirley-type background.[43]

The acquisition of the NEXAFS spectra was carried for the carbon and nitrogen regions in the PEY mode with retarding voltages of −150 V and −300 V, respectively. Linearly polarized synchrotron light was used as the primary X-ray source. The incidence angle of X-rays was varied from 90° (***E*** vector in the surface plane) to 20° (***E***-vector near the surface normal) in steps of

10 – 20° to monitor the molecular orientation in the SAMs. This approach is based on the dependence of the cross section of the resonant photoexcitation process on the orientation of the electric field vector of the synchrotron light with respect to the molecular orbital of interest (so-called linear dichroism in X-ray absorption).[53] The energy scale was calibrated by means of the most intense π* resonance of highly oriented pyrolytic graphite at 285.38 eV[54] in combination with the well-known $\Delta h\nu \propto (h\nu)^{3/2}$ behavior of plane grating monochromators.[55]

The RAES spectra were acquired using either a Scienta R3000 electron energy analyzer (BESSY II) or a SCIENTA SES200 spectrometer (Max-lab). The X-ray incidence angle was set to 55° to suppress possible orientational effects;[53] the take-off geometry of the electrons was close to normal emission. Resonant excitation was performed at the nitrogen K-edge, at the position of the π(CN*) resonance. The excitation energy was determined in the preliminary NEXAFS experiments. In addition, non-resonant Auger electron spectra were recorded at an excitation energy of 5-6 eV above the absorption edge. This setting was mimicked from similar experiments on nitrile-substituted SAMs on Au{111}, where it was found to be optimal in order to maximize the signal-to-noise ratio and to avoid appearance of interfering gold photoemission in the spectra.[25] Finally, for every sample, a reference spectrum for the pre-edge excitation was measured. This spectrum was subtracted from the RAES and non-resonant AES spectra to correct them for a contribution of the photoemission which could not be avoided completely.

2.3 Results

2.3.1 Scanning Tunneling Microscopy – Molecular Resolution of Surface Structure

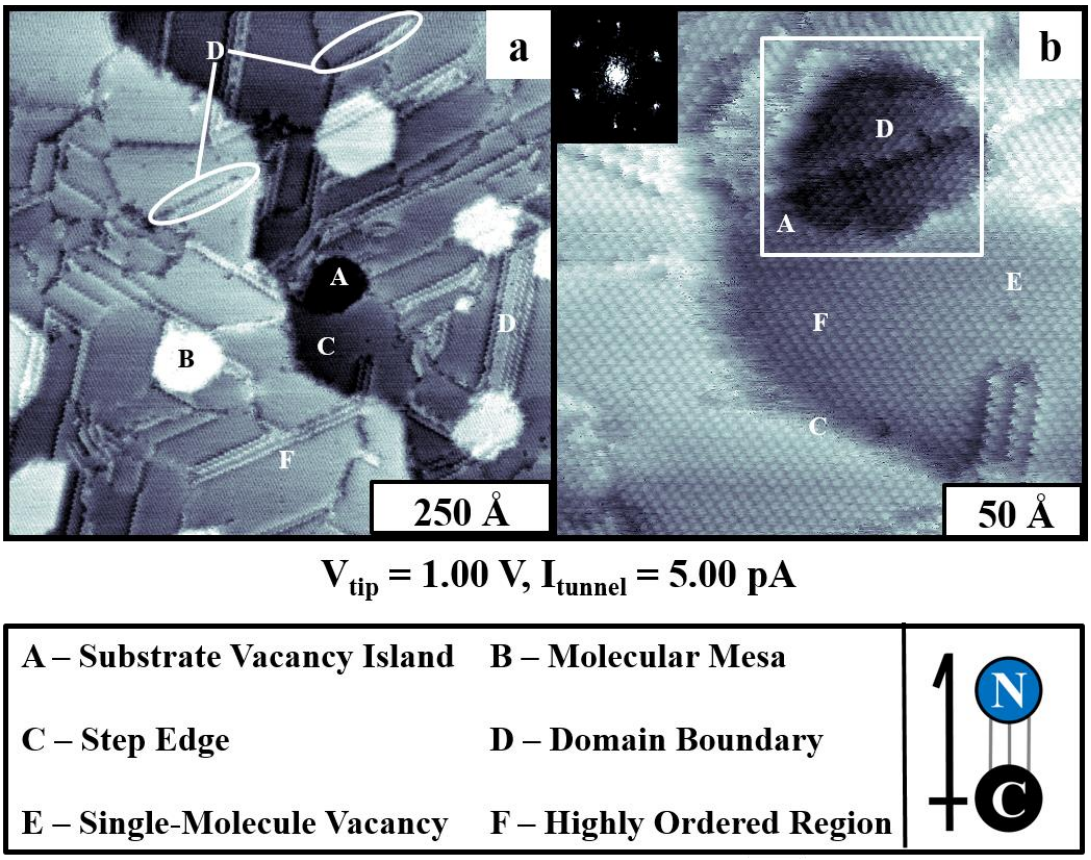

Figure 2.1. Scanning tunneling microscope images of the surface structure of cyanide monolayers on Au{111} at room temperature. (a) The morphology of the cyanide monolayers with representative surface structures denoted by letters A-F in the image and schematic of cyanide with aligned dipole C → N, Positive → Negative). (b) Molecular resolution images and corresponding Fourier transform showing the hexagonally close-packed lattice with nearest neighbor distance of 3.8 ± 0.5 Å.

The STM image in Figure 2.1a shows the structural details of monlayers of cyanide formed from exposure of Au{111} to HCN(g) at room temperature and humidity, most likely due the established gold cyanidation redox reaction that involves water and oxygen.[33,43] In comparison to the relatively featureless AuCN monolayers on Au{111} in solution, which is formed through electrochemical deposition,[56] cyanide molecules deposited in this manner are arranged into numerous, highly ordered domains, one-atom deep substrate vacancy islands, and one-atom high substrate mesas. At this resolution, the surface morphology closely resembles alkanethiol SAMs, which are also observed to form hcp lattices that contain single-substrate-atom deep vacancy islands and domain boundaries.[4,11,44] with the exception of the mesas and the simpler domain boundary structures here. The observed loss of the Au{111} herringbone structure and the appearance of vacancy islands indicate removal of the reconstruction of the underlying gold lattice and the relatively strong molecule-substrate interactions.[4,11,44,57] This change is not surprising; the thiolate Au-S bond reported at ~2 eV[4,44] is weaker than the Au-C bond reported at >2.4 eV[58,59] and the alkanethiol system also removes the reconstruction of the underlying Au{111} lattice.[4,11,44] Note that the existence of a strong dipole of the cyanide molecule,[60] (negative → positive, C→N, see schematic in Figure 2.1) axis is a significant property difference from alkanethiol monolayers on Au{111} that can be leveraged to elucidate dipole-mediated interactions.[23,61,62]

Higher resolution images (Figure 2.1b) reveal the arrangement of individual molecules that are positioned in a hexagonal close-packed arrangement. In addition to the previously mentioned structures, missing single-molecule vacancies can be observed in the molecular lattice. A Fourier transform of the STM image in Figure 2.1b (inset) shows a hexagonal lattice with the first-order reciprocal lattice spots displayed. The distance from the center in Fourier space to one of the frequency modes corresponds to an average measured nearest neighbor distance of 3.8±0.5 Å and

was obtained using measurements from >50 images of different sample regions from >10 different samples. These measurements agree well with reported Au-Au bond spacing in cyanide-gold crystals.[36,38,63] All images were obtained and calibrated against a known SAM of decanethiol on Au{111} before and directly after imaging cyanide to minimize measurement error. Using the calculated nearest neighbor spacing, the Au lattice spacing of 2.89 Å, and the hexagonal close-packed arrangement, the surface packing density for cyanide on Au{111} was calculated to be approximately 1 CN molecule per 1.3 Au atoms. This result closely mirrors the bonding configuration in coordination complexes composed of gold and cyanide where multiple cyanide molecules bind to one gold atom.

The specific rotational orientation of the monolayer with respect to the underlying gold lattice is determined with respect to the close-packed direction of the Au{111} formed along straight step edges.[64] The schematic in Figure 2.2 uses dark circles to represent the space-filling projection of the cyanide molecules on the surface using the spatial measurements from the STM images. We find that at the 20°, -40°, and 80° in-plane rotations with respect to the underlying gold lattice that bound cyanide molecules primarily occupied the two-fold bridge site with the remaining minority aligned with atop positions. The two-fold bridge location has been calculated to be the one of the most stable surface locations based on DFT calculations for cyanide bonding to Au{100}, Au{110}, and Au{111}.[65] These in-plane orientational rotations are identified as black triangles in the STM image included in Figure 2.2 when aligning with monolayer domain boundaries and can be seen to be examples of high symmetry points maintaining the characteristic 60° rotations of the hexagonal close-packed arrangement. In comparison, all other angles introduced binding at three-fold hollow sites, reduced the number of two-fold bridges, and were

observed less frequently than these other rotations in STM images via domain boundary inspection.

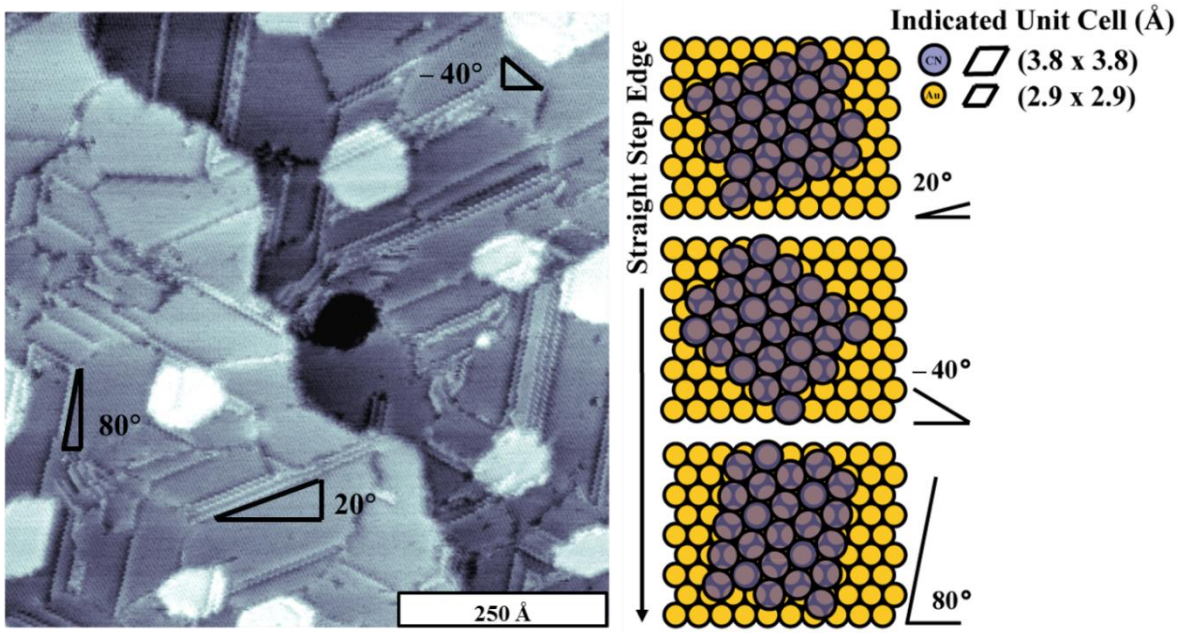

Figure 2.2. Scanning tunneling microscope image of CN on Au{111} as deposited at room temperature and structural schematics. Using the Au close-packed substrate direction with respect to a straight step edge (< 0 1 0 >) we find molecules bind to bridge and atop positions with a (3.8 Å × 3.8 Å) cyanide unit cell at 20°, -40°, and 80° orientations with respect to the unreconstructed underlying gold lattice. The dark, larger circles represent the projection of the cyanide molecules on the smaller circles representing the atoms of the Au{111} lattice. Triangles representing examples of the identified orientations relative to the Au{111} lattice are aligned with cyanide domain boundaries and are identified as high-symmetry directions representative of the hexagonal close-packed arrangement.

2.3.2 X-Ray Photoelectron Spectroscopy — Surface Elemental Analysis

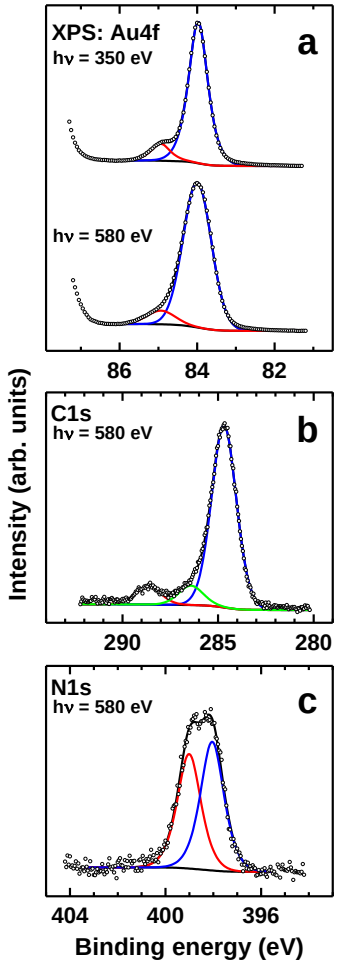

Figure 2.3. Au $4f_{7/2}$ (a), C 1s (b), and N 1s (c) X-ray photoelectron spectra of NC/Au(111) acquired at photon energies of either 350 or 580 eV as marked in the panels (open circles). The spectra are fit and decomposed into individual contributions (thin solid lines). See text for details.

Representative Au $4f_{7/2}$ (a), C 1s (b), and N 1s (c) XPS spectra of NC/Au{111} are shown in Figure 2.3. The Au $4f_{7/2}$ spectra in Figure 2.3 exhibit a weak shoulder at the high E_B side of the main emission, at a E_B of 84.95 eV. The appearance of this shoulder is attributed to the effect of

adsorbed NC, which is strong and, in its extent, is similar to the oxidation of the gold substrate.[66] Significantly, only the topmost layer of the Au{111} substrate is affected, as seen from the direct comparison of the spectra acquired at PEs of 350 and 580 eV in Figure 2.3a. Due to the strong dependence of the sampling depth of XPS on the kinetic energy of photoelectrons,[67] the contribution of the surface as compared to bulk should be much weaker in the latter case and, indeed, the high E_B shoulder decreases significantly in intensity at a PE of 580 eV as compared to 350 eV. Further, the intensity relation between the shoulder and the main emission in the 350 eV spectrum can be compared to the analogous relation in the spectrum of clean Au{111}, where the contributions of the topmost layer and the bulk can be straightforwardly distinguished.[51] Accordingly, the shoulder is indeed exclusively related to the topmost layer of the Au{111} substrate, corresponding, according to its spectral weight, to ca. 0.25 of this layer.

The C 1s XP spectrum of NC/Au{111} in Figure 2.3b exhibits strong emission at ~284.7 eV accompanied by two weak peaks at ~286.4 eV and ~288.65 eV. The dominant emission can be assigned to the adsorbed NC molecules while the low intensity peaks presumably stem from contamination, most likely CO (~286.4 eV) and COOH (~288.65 eV).[68] Such contamination can hardly be avoided considering the ultimate thinness of the NC monolayer and its exposure to ambient in the course of the sample handling. As to dominant emission, note, for comparison, that, as expected, its E_B is much lower than that of the nitrile carbon in SAMs of the nitrile-substituted alkanethiols, NC-$(CH_2)_n$-SH (NC-Cn) on Au{111}, e.g., 286.2 eV at $n = 3$.[30] The lower E_B in the case of NC/Au{111} can be attributed to the direct bonding of NC to the substrate (chemical shift) as well as to more efficient screening of the photoemission hole by the substrate electrons (the screening effect scales according to the Coulomb potential, i.e., is proportional to 1/r).

The N 1s XP spectrum of NC/Au{111} in Figure 2.3c exhibits a broad peak that can be tentatively decomposed into two individual emissions at ~398.1 and ~399.0 eV, with the former emission being more intense. This emission can be unequivocally attributed to the nitrile molecules attached to the substrate over C–Au bond. The E_B of 398.1 eV correlates well with the respective E_B for the NC-alkyl SAMs on Au{111}, viz. 398.84 eV for the NC-C_2H_4S film and 398.98 eV for the NC-C_3H_6S monolayer,[30] being noticeably smaller than these values because of the stronger proximity on nitrile to the substrate in the case of NC/Au{111} (see discussion regarding the C 1s spectrum). The value of ~399.0 eV is even higher than the value of 398.84 eV for the NC-C_2H_4S film on Au{111} suggesting that the respective species are bound only weakly to the substrate, probably in a physisorbed fashion.

2.3.3 Vibrational Spectroscopy – Connectivity

To determine the chemical state and identity of cyanide molecules on Au{111}, we utilized attenuated total internal reflection Fourier transform interferometry (ATR-FTIR). The IR absorption spectrum of Au{111} after exposure to HCN(g) is shown in Figure 2.4. The primary CN stretching mode detected at 2146 cm^{-1} on the Au{111} is in good agreement with spectra for cyanide adsorbed on the surface of gold electrodes in a cyanide solution,[69] is red shifted when compared to the 2200–2300 cm^{-1} range given for the nitrile functional group,[70] and shows the typical blue shift due to substrate coupling from the approximately 2100 cm^{-1} for the free cyanide ion in solution[69,71,72] (see Table 2.1 for comparisons). We observed two small side peaks at 2134 and 2161 cm^{-1} on the Au{111} surface using ATR-FTIR, which is more sensitive to thin films, on either side of the larger, distinct CN stretch at 2146 cm^{-1}. These two additional modes are also likely attributed to the CN stretch, supporting the nitrogen XPS results suggesting different surface

states exist for cyanide molecules on the surface. The asymmetric side peaks are not detected for CN adsorbed on polycrystalline Au[69] most likely because the same amount of order cannot be achieved due to the amorphous nature of the surface.

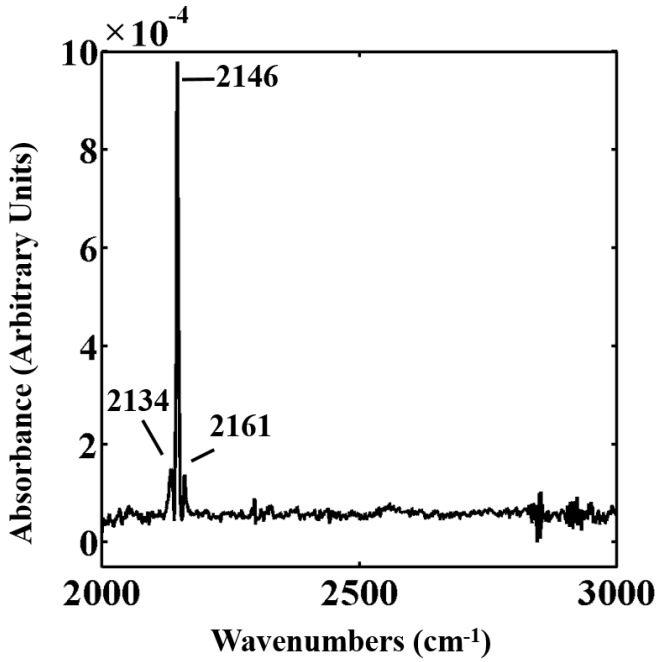

Figure 2.4. The attenuated total reflection Fourier transform infrared spectrum of CN/Au{111} using custom sapphire prism substrates and showing the CN stretch at 2146 cm^{-1} along with two side peaks at 2134 and 2161 cm^{-1}.

No vibrational modes were identified near 3300 cm^{-1} for the CH vibrational mode of the HCN molecule (also shown in Table 2.1).[73] This observation is consistent with deprotonation during monolayer formation. All spectral measurements were recorded with a bare Au surface as a reference that showed no peaks in the region of interest, and peak locations were reproducible over different samples and days.

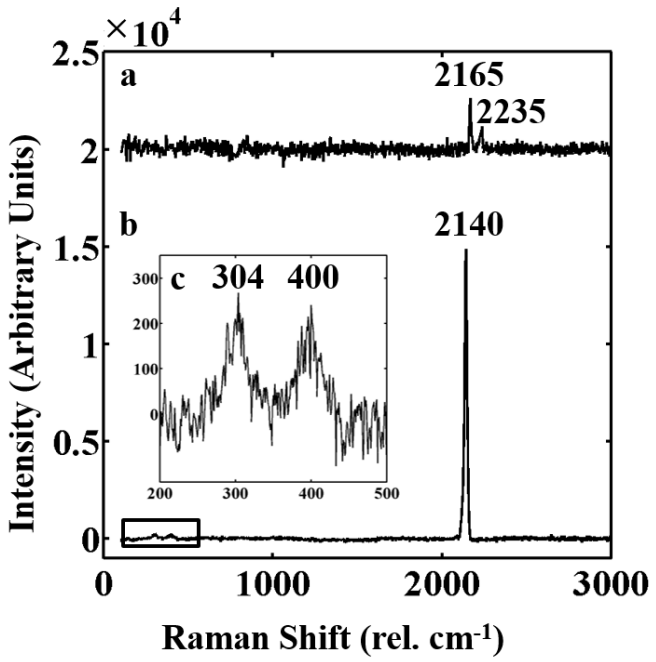

Figure 2.5. (a) Raman spectra of CN monolayers formed on Au{111} using a plasmonic nanohole array and (b) surface-enhanced Raman substrates made of polycrystalline Au nanoparticles evaporated onto glass. (c) The inset shows both the low frequency modes attributed to the substrate-molecule bond, Au-CN bend at 304 cm^{-1} and Au-CN stretch at 400 cm^{-1}, which were only detected on the Au nanoparticles.

Raman spectroscopy was used to detect low-frequency, substrate-adsorbate binding modes and the high-frequency internal stretching mode. The Raman spectra for Au{111} and polycrystalline Au nanoparticles (NPs) after exposure to HCN(g) are shown in Figures 2.5a and 2.5b, respectively. The low-frequency modes detected around 304 and 400 cm^{-1} (see Figure 2.5c inset, Table 2.1 for comparisons) agree well with values reported for a Au-C stretch and a Au-C-N bend for cyanide ions adsorbed both on Au electrode surfaces in cyanide-ion-containing solution[74] and cyanide-coated gold nanoparticles.[72] However, we were only able to detect the low-frequency modes on the custom Au NP SERS surface, as the signal-to-noise ratio was much better on the Au

NPs. The results are further evidence that the cyanide assembles here attached through Au-C bonds, and not through nitrogen, maintaining the typical bonding scheme for carbon-bound nitrile groups and gold-cyanide coordination complexes.[33,38]

Table 2.1. Comparison of the different vibration energies for the cyanide/nitrile group as a ligand at solution and air interfaces.

Substance	CN Triple Bond Stretch (cm^{-1})	CH Single Bond Stretch (cm^{-1})	CN Triple Bond Raman Shift (cm^{-1})	Au-C-N Raman Shift (cm^{-1})	Au-C Raman Shift (cm^{-1})	Ref
CN/Au, solution	2105	N/A	2135	300	380	69, 74
$Au(CN)_2^-$,solution	2146	N/A	2156	294	371	69, 72
AuCN, solid/crystal	2236	N/A	2230	358	598	63
HCN, gas	2089	3312	N/A	N/A	N/A	73
CN^- , solution	2050-2100	N/A	N/A	N/A	N/A	69, 71, 72
CN/Au, air*	2146	None	2140-2165, 2235	304	400	N/A
CN (Nitrile)	2200-2300	2900-3000	2248	N/A	N/A	70, 75

N/A – Not Applicable

****Results presented here***

The high-frequency mode located at 2140 cm^{-1} for the Au NP's detected by Raman compares well with the detected IR mode for the Au{111} substrate, but is blue shifted by 25 cm^{-1} when compared to the peak at 2165 cm^{-1} detected by Raman for CN/Au{111} and red shifted when compared with the 2248 cm^{-1} reported for the Raman spectra of the nitrile functional group.[75] An additional peak, which is further evidence of different cyanide states, was located in the CN/Au{111} spectrum at 2235 cm^{-1}, a value that closely matches values reported for CN in solid

AuCN crystals.[63] We note that all the Raman shifts detected on the polycrystalline Au NPs are blue shifted ~20 cm^{-1} compared to cyanide molecules adsorbed on Au{111}. The results presented here may be more accurate as they are not complicated by dissolving the gold into the surrounding solution or applied electric fields.

2.3.4 Near-Edge X-Ray Fine Scattering Spectroscopy – Molecule Orientation

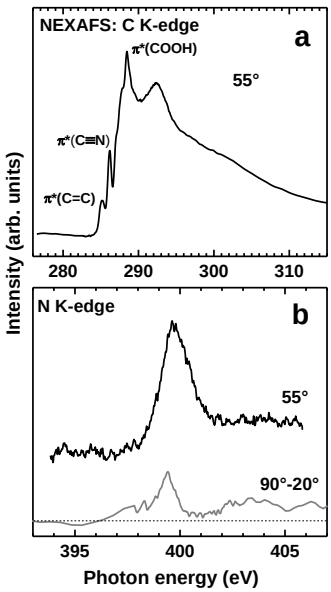

Figure 2.6. C (a) and N (b) K-edge near-edge X-ray fine scattering spectra of NC/Au{111} acquired at an X-ray incident angle of 55° (black solid curves), along with the respective difference between the spectra collected under the normal (90°) and grazing (20°) incidence geometry (gray solid curve in panel b). The characteristic absorption resonances are marked. The horizontal dashed line in panel (b) corresponds to zero intensity.

C and N K-edge NEXAFS spectra of NC/Au{111} acquired at an X-ray incident angle of 55° are presented in Figure 2.6, along with the respective difference between the N K-edge spectra

collected under the normal (90°) and grazing (20°) incidence geometry. Note that the "magic angle", 55° spectra are free of orientational effects and, subsequently, only representative of the electronic structure of the studied systems.[53] In contrast, the difference between the spectra acquired at normal and grazing incidence of X-rays are representative of the molecular orientation, averaged over the probed ensemble, relying on the linear dichroism effect in X-ray absorption.[53]

The C K-edge spectrum of NC/Au{111} in Figure 2.6a exhibits several absorption resonances superimposed onto the absorption edge. These include π*(C=C) resonance at 285.1 eV, the π(C*≡N) resonance at 286.2 eV, and π*(COOH) at 288.5 eV (the assignments were made according to refs 30 and 53). The π*(C=C) and π*(COOH) features stem from contamination while the π(C*≡N) resonance is characteristic of the CN groups and is attributed to two (almost) degenerate, mutually orthogonal π(C≡N) orbitals.[25,27] Its position depends only weakly on the chemical state of the CN group (unless there is π*-π* hybridization with the adjacent functional group)[28] and, in particular, does not vary much across the NC-alkyl/Au{111} series, being 286.8 – 286.9 eV.

The 55° N K-edge spectrum of NC/Au{111} in Figure 2.6b exhibits a characteristic π* resonance of the nitrile group at 399.7 eV. Similar to the π(C*≡N) resonance, it is attributed to two (almost) degenerate, mutually orthogonal π(C≡N) orbitals.[25,27] The presence of this feature as well as the π(C*≡N) resonance at the C K-edge (see above) suggests an upright orientation of the NC moieties in NC/Au{111}. Otherwise, both π(C*≡N) and π(C≡N*) resonances will be quenched through the direct interaction with the substrate and be imperceptible in the spectra. The energy of the π(C≡N*) resonance for NC/Au{111} is quite close to the analogous value for the NC-alkyl SAMs on Au{111}, viz. 399.75 eV (independent of chain length).[30]

The 90°-20° difference spectrum in Figure 2.6b exhibits a pronounced, positive peak at the position of the π(C≡N*) resonance suggesting, in view of the orientation of the respective molecular orbitals (perpendicular to the C≡N axis), an upright orientation of the nitrile groups in NC/Au{111}.

2.3.5 Resonant Auger Electron Spectroscopy – Molecule-Substrate Charge-Transfer Efficiency

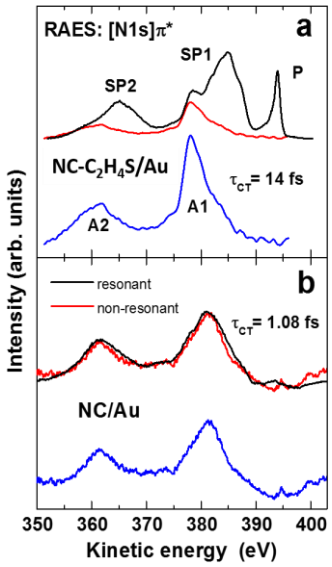

Figure 2.7. [N1s]π* resonant Auger electron spectra (black curves) and non-resonant Auger electron (blue curves) spectra of NC-C_2H_4S/Au (a) and NC/Au{111} (b). The electron transfer contribution in the resonant Auger electron spectra is shown (red curves). P, SP1, and SP2 denote the participator and two spectator features, respectively. A1 and A2 denote two characteristic features in the non-resonant spectra. The derived τ_{ET} are given. The spectra of NC-C_2H_4S/Au are reprinted with permission from ref 30. Copyright (2010) American Chemical Society.

Nitrile groups have been used before as the starting point for electron transfer (ET) through the molecular framework in SAMs on conductive substrates.[12,25,27-30] These functional groups were

attached to the molecular backbone as a tail moiety at the SAM-ambient interface while the molecules were coupled to the substrate, Au{111}, by the thiolate anchors. The ET was triggered by the resonant excitation of the N 1s electron into the π(C≡N*) orbital and monitored by RAES within CHC approach.[76-80] Within this approach, different de-excitation channels of the [N1s]π* state are followed, viz. the emission of the excited electron (participator channel; P), emission of another electron from occupied valence molecular orbital (spectator channel; SP), and ET of the excited electron to the substrate, all accompanied by an interband transition from occupied valence molecular orbital to the N1s hole. The P and SP processes, which are the standard de-exitation routes for RAES, result in one hole (1h) and a two-hole one-electron (2h1e) states, respectively (see ref 29 for details and schematic illustration of the relevant processes). In contrast, the ET scenario results in a 2h state which is almost identical to the final state of non-resonant Auger electron emission processes.[81] Due to the different final states, all the above processes have different spectroscopic signatures in the overall RAES spectrum, which can be distinguished and the ET contribution, P_{ET}, precisely extracted. Consequently, characteristic ET time, τ_{ET}, can be evaluated using the major formula of the CHC approach, viz. $\tau_{ET} = \tau_{core} (1 - P_{ET}) / P_{ET}$, where τ_{ET} is the core-hole lifetime serving as internal clock for the ET process and giving the name to the approach.[77] This lifetime is 6.4 fs for the N1s core hole,[76] providing access to the femtosecond time domain without use of any complex experimental setup relying on pump-probe techniques.

The length of the molecular backbone in the CHC experiments on nitrile-substituted SAMs was varied, with P_{ET} increasing and τ_{ET} decreasing progressively with decreasing backbone length.[28-30] In particular, τ_{ET} varied from 100 ± 26 fs for NC-C_4H_8S/Au to 35 ± 9 fs for NC-C_3H_6S/Au to 14 ± 4 fs for NC-C_2H_4S/Au.[30] Further, in the extrapolated limit of the negligible short backbone, the characteristic time for ET from the NC group directly attached to the thiolate

anchor to the substrate was found to be ~2.3 fs[31] and ~2.8 fs[28] in the independent experiments on different systems, being ~2.5 fs on average. In this context, NC/Au{111} represents a further, even more ultimate case, with the exclusion of the "intermediate" thiolate moiety and direct attachment of the nitrile group to Au{111} with C–Au bond. Under these circumstances, ET to the substrate should be especially efficient, representing, most likely, the major de-excitation channel of the [N1s]π* state.

This is indeed the case, as shown in Figure 2.7, where the [N1s]π* resonant Auger electron spectra (RAES) and corresponding Auger electron spectra (AES) for NC/Au{111} are presented, along with the analogous data for NC-C_2H_4S/Au{111},[25,30] for comparison. The RAES spectra of NC-C_2H_4S/Au{111} are dominated by the SP and P contributions, while the ET part, shown separately, contributes only ~30% of the entire spectral weight. In contrast, the RAES and AES spectra of NC/Au{111} are almost identical suggesting that the former spectra are dominated by the ET contribution, while the SP and P parts are barely perceptible. Taking the RAES spectrum of NC-$C_{16}H_{32}S$/Au{111} as the reference for the purely resonant (autoionization) spectrum[25,30] and non-resonant AES spectrum of NC/Au{111} as representative for the ET process (see above), the RAES spectrum of NC/Au{111} could be decomposed into the SP/P and ET contributions and τ_{ET} can be calculated according to the major formula of the CHC approach (see above). Three independent sets of experiments resulted in τ_{ET} values of 0.25, 1.08, and 1.38 fs, giving 0.9 fs on average. The accuracy of this value is ±0.5 fs from the statistical viewpoint and ±0.25 fs based on the accuracy of the τ_{core} value.[76] The most important fact, however, is the clear dominance of the ET process over the SP/P contributions in the [N1s]π* decay spectrum of NC/Au{111}, suggesting strong coupling of the nitrile moiety to the substrate. Another important result, is an ultimate proof for the CHC approach in its specific application to SAMs, based on the resonantly addressable NC

group.[12,25,27-30] Indeed, as can be expected, the value of τ_{ET} for the direct attachment of the nitrile group to the Au{111} substrate is noticeably smaller than that for any molecular backbone, e.g., 14.4 fs for NC-C_2H_4S/Au[25,30] and 9 ± 3 fs for SAMs of NC-C_6H_4-SH/Au{111},[28] and even smaller than the limit value corresponding to the negligibly short backbone, viz. 2.5 fs.[28,30] Note that the time associated with the ET from the molecular backbone to the substrate over the thiolate anchor can be roughly estimated at 1 fs. This value is well comparable to a characteristic time of ~320 asec observed for ET from an adsorbed sulfur atom to the substrate in the c(4×2)-S/Ru(0001) system.[80] The difference, which is reasonably small, can be explained by band alignment differences, the stronger bonding of the S atoms to the substrate in the latter case, as well as by the different characters of the involved orbitals serving as the starting point for ET in both cases. It is well known that the character of the primary molecular or atomic orbital affects the efficiency of ET.[27,28]

2.4 Discussion of Results — Bonding Scheme and Substrate-Molecule Coupling

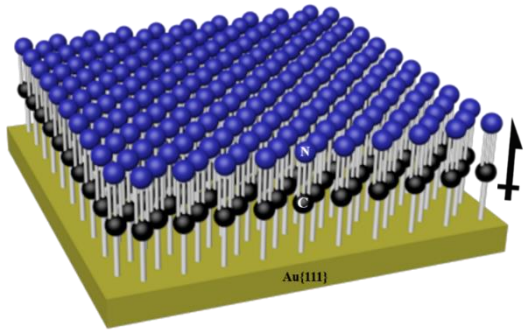

Figure 2.8. Bonding scheme showing cyanide adsorbed on Au{111} as an upright molecule, attached through C, with the positive end of the dipole aligned outward.

Combining our structural and spectroscopic measurements with known Au-cyanide chemistry, we propose a bonding scheme for cyanide monolayers on Au{111}, as shown in Figure 2.8. Assuming that the molecules on the surface organize to maximize intermolecular interactions for monolayer stability, and to offset unfavorable dipole coupling,[69] we propose a bonding scheme where the cyanide molecules are bound via an Au-C bond and are oriented normal to the surface. It should be pointed out that when cyanide is attached to a carbon backbone as a nitrile group it has an inclined orientation measured around 65°[3,30] and suggests that the strength of the substrate-molecule bond overpowers the unfavorable dipole-dipole interactions.

Finally, from the CHC results measuring the ~1 fs charge transfer from the cyanide directly to the gold, as shown schematically in Figure 2.9. We can infer that the electronic coupling is particularly strong between the carbon and gold based on the facile electron transfer. This result directly supports the expected dominance of σ bonding suggested by the increase in CN vibrational frequency. The electron transfer efficiency, coupled with the molecule orientation, is an indication that there is a favorable energetic overlap between the molecular transport orbitals and substrate Fermi level[24] and follows the trend for electron transfer time as a function of the length of the carbon backbone in nitrile functionalized alkanethiol SAMs.[30] In fact, complementary to these results, it has been reported that the conduction efficiency is significantly lower for isocyanide or Au-NC bound, molecules.[31]

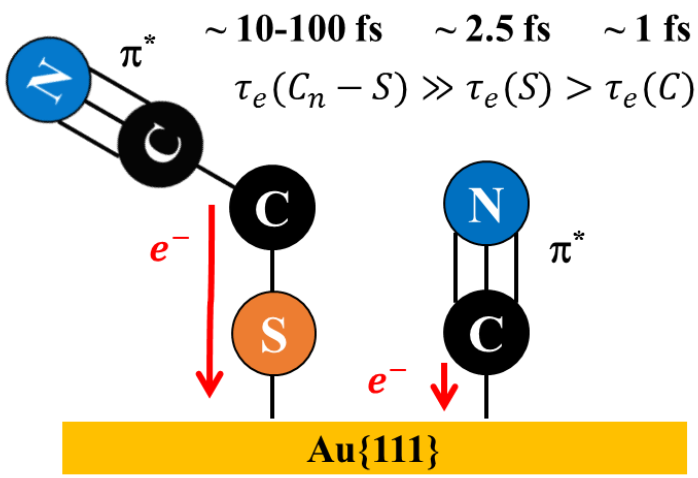

Figure 2.9. Electron transfer across the Au-C bond is extremely efficient at ~1 fs indicating strong electronic coupling between substrate and molecule.

2.5 Conclusions and Prospects

The vibrational and structural characteristics of stable cyanide monolayers on Au{111} are revealed and we show that coupling to the gold substrate is particularly strong, leading to facile electron transfer. Cyanide molecules form a hexagonal close-packed lattice with a nearest neighbor spacing of 3.8 ± 0.5 Å. It was discovered using ATR-FTIR and SERS that the cyanide molecules are attached to the gold through the carbon atom and oriented normal to the surface. The molecular composition and orientation was supported by HRXPS and NEXAFS and we discuss a bonding scheme that compares favorably with the structure observed in the STM images. The CHC method of RAES measured the charge transfer from the cyanide to the gold to be approximately 1 fs, comparable to charge transfer across the sulfur bond of thiols and 100 times faster than when an alkane backbone is present. These results further validate the use of the core-hole clock method for measuring the ultrafast process of electron transfer between molecule and substrate for

self-assembled monolayers. Current research is aimed at exploiting the strong dipole moment of cyanide, molecule orientation, and the strength of the molecule-substrate electronic coupling for probing the interactions between molecular electronic structure and molecular vibrations at room temperature, which is critical to developing more generally applicable single-molecule spectroscopic techniques.

2.6 References

1. Netzer, L.; Iscovici, R.; Sagiv, J. Adsorbed Monolayers versus Langmuir-Blodgett Monolayers—Why and How? II: Characterization of Built-Up Films Constructed by Stepwise Adsorption of Individual Monolayers. *Thin Solid Films* **1983**, *100*, 67–76.

2. Stranick, S. J.; Kamna, M. M.; Krom, K. R.; Parikh, A. N.; Allara, D. L.; Weiss, P. S. Scanning Tunneling Microscopy Studies of Self-Assembled Monolayers of Alkanethiols on Gold. *J. Vac. Sci. Technol. B* **1994**, *12*, 2004–2007.

3. Frey, S.; Shaporenko, A.; Zharnikov, M.; Harder, P.; Allara, D. L. Self-Assembled Monolayers of Nitrile-Functionalized Alkanethiols on Gold and Silver Substrates. *J. Phys. Chem. B* **2003**, *107*, 7716–7725.

4. Love, J. C.; Estroff, L. A.; Kriebel, J. K.; Nuzzo, R. G.; Whitesides, G. M. Self-Assembled Monolayers of Thiolates on Metals as a Form of Nanotechnology. *Chem. Rev.* **2005**, *105*, 1103–1170.

5. Weiss, P. S. Functional Molecules and Assemblies in Controlled Environments: Formation and Measurements. *Acc. Chem. Res.* **2008**, *41*, 1772–1781.

6. Liao, W.-S.; Cheunkar, S.; Cao, H. H.; Bednar, H. R.; Weiss, P. S.; Andrews, A. M. Subtractive Patterning via Chemical Lift-Off Lithography. *Science* **2012**, *337*, 1517–1521.

7. Kim, J.; Rim, Y. S.; Liu, Y.; Serino, A. C.; Thomas, J. C.; Chen, H.; Yang, Y.; Weiss, P. S. Interface Control in Organic Electronics Using Mixed Monolayers of Carboranethiol Isomers. *Nano Lett.* **2014**, *14*, 2946–2951.

8. Abendroth, J. M.; Bushuyev, O. S.; Weiss, P. S.; Barrett, C. J. Controlling Motion at the Nanoscale: Rise of the Molecular Machines. *ACS Nano* **2015**, *9*, 7746–7768.

9. Sykes, E. C. H.; Han, P.; Kandel, S. A.; Kelly, K. F.; McCarty, G. S.; Weiss, P. S. Substrate-Mediated Interactions and Intermolecular Forces between Molecules Adsorbed on Surfaces. *Acc. Chem. Res.* **2003**, *36*, 945–953.

10. Monnell, J. D.; Stapleton, J. J.; Dirk, S. M.; Reinerth, W. A.; Tour, J. M.; Allara, D. L.; Weiss, P. S. Relative Conductances of Alkaneselenolate and Alkanethiolate Monolayers on Au{111}. *J. Phys. Chem. B* **2005**, *109*, 20343–20349.

11. Hakkinen, H. The Gold-Sulfur Interface at the Nanoscale. *Nat. Chem.* **2012**, *4*, 443–455.

12. Ossowski, J.; Wächter, T.; Silies, L.; Kind, M.; Noworolska, A.; Blobner, F.; Gnatek, D.; Rysz, J.; Bolte, M.; Feulner, P.; Terfort, A.; Cyganik, P.; Zharnikov, M. Thiolate versus Selenolate: Structure, Stability, and Charge Transfer Properties. *ACS Nano* **2015**, *9*, 4508–4526.

13. Cygan, M. T.; Dunbar, T. D.; Arnold, J. J.; Bumm, L. A.; Shedlock, N. F.; Burgin, T. P.; Jones, L.; Allara, D. L.; Tour, J. M.; Weiss, P. S. Insertion, Conductivity, and Structures of Conjugated Organic Oligomers in Self-Assembled Alkanethiol Monolayers on Au{111}. *J. Am. Chem. Soc.* **1998**, *120*, 2721–2732.

14. Weck, M.; Jackiw, J. J.; Rossi, R. R.; Weiss, P. S.; Grubbs, R. H. Ring-Opening Metathesis Polymerization from Surfaces. *J. Am. Chem. Soc.* **1999**, *121*, 4088–4089.

15. Saavedra, H. M.; Thompson, C. M.; Hohman, J. N.; Crespi, V. H.; Weiss, P. S. Reversible Lability by in Situ Reaction of Self-Assembled Monolayers. *J. Am. Chem. Soc.* **2009**, *131*, 2252–2259.

16. Saavedra, H. M.; Mullen, T. J.; Zhang, P.; Dewey, D. C.; Claridge, S. A.; Weiss, P. S. Hybrid Strategies in Nanolithography. *Rep. Prog. Phys.* **2010**, *73*, 036501.

17. Kim, M.; Hohman, J. N.; Cao, Y.; Houk, K. N.; Ma, H.; Jen, A. K.-Y.; Weiss, P. S. Creating Favorable Geometries for Directing Organic Photoreactions in Alkanethiolate Monolayers. *Science* **2011**, *331*, 1312–1315.

18. Cao, H. H.; Nakatsuka, N.; Serino, A. C.; Liao, W.-S.; Cheunkar, S.; Yang, H.; Weiss, P. S.; Andrews, A. M. Controlled DNA Patterning by Chemical Lift-Off Lithography: Matrix Matters. *ACS Nano* **2015**, 11439.

19. Kumar, A. S.; Ye, T.; Takami, T.; Yu, B.-C.; Flatt, A. K.; Tour, J. M.; Weiss, P. S. Reversible Photo-Switching of Single Azobenzene Molecules in Controlled Nanoscale Environments. *Nano Lett.* **2008**, *8*, 1644–1648.

20. Gao, P.; Weaver, M. J. Metal-Adsorbate Vibrational Frequencies as a Probe of Surface Bonding: Halides and Pseudohalides at Gold Electrodes. *J. Phys. Chem.* **1986**, *90*, 4057–4063.

21. Michael, G.; Mark, A. R.; Abraham, N. Molecular Transport Junctions: Vibrational Effects. *J. Phys.: Condens. Matter* **2007**, *19*, 103201.

22. Donhauser, Z. J.; Mantooth, B. A.; Kelly, K. F.; Bumm, L. A.; Monnell, J. D.; Stapleton, J. J.; Price, D. W.; Rawlett, A. M.; Allara, D. L.; Tour, J. M.; Weiss, P. S. Conductance

Switching in Single Molecules through Conformational Changes. *Science* **2001**, *292*, 2303–2307.

23. Lewis, P. A.; Inman, C. E.; Maya, F.; Tour, J. M.; Hutchison, J. E.; Weiss, P. S. Molecular Engineering of the Polarity and Interactions of Molecular Electronic Switches. *J. Am. Chem. Soc.* **2005**, *127*, 17421–17426.

24. Zangmeister, C. D.; Robey, S. W.; van Zee, R. D.; Kushmerick, J. G.; Naciri, J.; Yao, Y.; Tour, J. M.; Varughese, B.; Xu, B.; Reutt-Robey, J. E. Fermi Level Alignment in Self-Assembled Molecular Layers: The Effect of Coupling Chemistry. *J. Phys. Chem. B* **2006**, *110*, 17138–17144.

25. Neppl, S.; Bauer, U.; Menzel, D.; Feulner, P.; Shaporenko, A.; Zharnikov, M.; Kao, P.; Allara, D. L. Charge Transfer Dynamics in Self-Assembled Monomolecular Films. *Chem. Phys. Lett.* **2007**, *447*, 227–231.

26. Moore, A. M.; Weiss, P. S. Functional and Spectroscopic Measurements with Scanning Tunneling Microscopy. *Ann. Rev. Anal. Chem.* **2008**, *1*, 857–882.

27. Blobner, F.; Coto, P. B.; Allegretti, F.; Bockstedte, M.; Rubio-Pons, O.; Wang, H.; Allara, D. L.; Zharnikov, M.; Thoss, M.; Feulner, P. Orbital-Symmetry-Dependent Electron Transfer through Molecules Assembled on Metal Substrates. *J. Phys. Chem. Lett.* **2012**, *3*, 436–440.

28. Hamoudi, H.; Neppl, S.; Kao, P.; Schüpbach, B.; Feulner, P.; Terfort, A.; Allara, D.; Zharnikov, M. Orbital-Dependent Charge Transfer Dynamics in Conjugated Self-Assembled Monolayers. *Phys. Rev. Lett.* **2011**, *107*, 027801.

29. Zharnikov, M. Probing Charge Transfer Dynamics in Self-Assembled Monolayers by Core Hole Clock Approach. *J. Electron. Spectrosc. Relat. Phenom.* **2015**, *200*, 160–173.

30. Kao, P.; Neppl, S.; Feulner, P.; Allara, D. L.; Zharnikov, M. Charge Transfer Time in Alkanethiolate Self-Assembled Monolayers via Resonant Auger Electron Spectroscopy. *J. Phys. Chem. C* **2010**, *114*, 13766–13773.

31. Kiguchi, M.; Miura, S.; Hara, K.; Sawamura, M.; Murakoshi, K. Conductance of a Single Molecule Anchored by an Isocyanide Substituent to Gold Electrodes. *Appl. Phys. Lett.* **2006**, *89*, 213104.

32. Lauhon, L. J.; Ho, W. Single-Molecule Vibrational Spectroscopy and Microscopy: CO on Cu(001) and Cu(110). *Phys. Rev. B* **1999**, *60*, R8525–R8528.

33. Ahmad, S. The Chemistry of Cyano Complexes of Gold(I) with Emphasis on the Ligand Scrambling Reactions. *Coord. Chem. Rev.* **2004**, *248*, 231–243.

34. McCarley, R. L.; Bard, A. J. Surface Reactions of Gold(111) with Aqueous Cyanide Studied by Scanning Tunneling Microscopy. *J. Phys. Chem.* **1992**, *96*, 7410–7416.

35. Sun, L.; Crooks, R. M. Indirect Visualization of Defect Structures Contained within Self-Assembled Organomercaptan Monolayers: Combined Use of Electrochemistry and Scanning Tunneling Microscopy. *Langmuir* **1993**, *9*, 1951-1954.

36. Katz, M. J.; Sakai, K.; Leznoff, D. B. The Use of Aurophilic and Other Metal-Metal Interactions as Crystal Engineering Design Elements to Increase Structural Dimensionality. *Chem. Soc. Rev.* **2008**, *37*, 1884–1895.

37. Hu, M.; Belik, A. A.; Imura, M.; Yamauchi, Y. Tailored Design of Multiple Nanoarchitectures in Metal-Cyanide Hybrid Coordination Polymers. *J. Am. Chem. Soc.* **2013**, *135*, 384–391.

38. Kim, K. H.; Kim, J. G.; Nozawa, S.; Sato, T.; Oang, K. Y.; Kim, T. W.; Ki, H.; Jo, J.; Park, S.; Song, C.; Sato, T.; Ogawa, K.; Togashi, T.; Tono, K.; Yabashi, M.; Ishikawa, T.; Kim, J.; Ryoo, R.; Kim, J.; Ihee, H.; Adachi, S.-i. Direct Observation of Bond Formation in Solution with Femtosecond X-Ray Scattering. *Nature* **2015**, *518*, 385–389.

39. Chattopadhyay, S.; Ganguly, A.; Chen, K.-H.; Chen, L.-C. One-Dimensional Group III-Nitrides: Growth, Properties, and Applications in Nanosensing and Nano-Optoelectronics. *Crit. Rev. Solid State Mater. Sci.* **2009**, *34*, 224–279.

40. Han, P.; Sykes, E. C. H.; Pearl, T. P.; Weiss, P. S. A Comparative Scanning Tunneling Microscopy Study of Physisorbed Linear Quadrupolar Molecules: C_2N_2 and CS_2 on Au{111} at 4 K. *J. Phys. Chem. A* **2003**, *107*, 8124–8129.

41. Swanson, S. A.; McClain, R.; Lovejoy, K. S.; Alamdari, N. B.; Hamilton, J. S.; Scott, J. C. Self-Assembled Diisocyanide Monolayer Films on Gold and Palladium. *Langmuir* **2005**, *21*, 5034–5039.

42. Crudden, C. M.; Horton, J. H.; Ebralidze, I. I.; Zenkina, O. V.; McLean, A. B.; Drevniok, B.; She, Z.; Kraatz, H.-B.; Mosey, N. J.; Seki, T.; Keske, E. C.; Leake, J. D.; Rousina-Webb, A.; Wu, G. Ultra Stable Self-Assembled Monolayers of N-Heterocyclic Carbenes on Gold. *Nat. Chem.* **2014**, *6*, 409–414.

43. Senanayake, G. Kinetics and Reaction Mechanism of Gold Cyanidation: Surface Reaction Model via Au(I)–OH–CN Complexes. *Hydrometallurgy* **2005**, *80*, 1–12.

44. Ulman, A. Formation and Structure of Self-Assembled Monolayers. *Chem. Rev.* **1996**, *96*, 1533–1554.

45. Porath, D.; Millo, O.; Gersten, J. I. Scanning Tunneling Microscopy Studies and Computer Simulations of Annealing of Gold Films. *J. Vac. Sci. Technol. B* **1996**, *14*, 30–37.

46. Bumm, L. A.; Arnold, J. J.; Charles, L. F.; Dunbar, T. D.; Allara, D. L.; Weiss, P. S. Directed Self-Assembly to Create Molecular Terraces with Molecularly Sharp Boundaries in Organic Monolayers. *J. Am. Chem. Soc.* **1999**, *121*, 8017–8021.

47. Mantooth, B. A. *Nanoscopic Analyses: Single Molecule Characterization in Molecular Electronics and Surface Science*. The Pennsylvania State University, University Park, PA **2004**.

48. Takashi, W.; Kento, A. Penetration-Depth Characteristics of Evanescent Fields at Metal Attenuated Total Reflection. *Jpn. J. Appl. Phys.* **2005**, *44*, 4272.

49. Zheng, Y. B.; Payton, J. L.; Chung, C.-H.; Liu, R.; Cheunkar, S.; Pathem, B. K.; Yang, Y.; Jensen, L.; Weiss, P. S. Surface-Enhanced Raman Spectroscopy to Probe Reversibly Photoswitchable Azobenzene in Controlled Nanoscale Environments. *Nano Lett.* **2011**, *11*, 3447–3452.

50. Heister, K.; Zharnikov, M.; Grunze, M.; Johansson, L. S. O.; Ulman, A. Characterization of X-ray Induced Damage in Alkanethiolate Monolayers by High-Resolution Photoelectron Spectroscopy. *Langmuir* **2001**, *17*, 8–11.

51. Zharnikov, M. High-Resolution X-Ray Photoelectron Spectroscopy in Studies of Self-Assembled Organic Monolayers. *J. Electron. Spectrosc. Relat. Phenom.* **2010**, *178–179*, 380–393.

52. Moulder, J. F.; Chastain, J. *Handbook of X-ray Photoelectron Spectroscopy: A Reference Book of Standard Spectra for Identification and Interpretation of XPS Data*. Physical Electronics Division, Perkin-Elmer Corporation: **1992**.

53. Stöhr, J. *NEXAFS Spectroscopy*. Springer: **1992**.

54. Batson, P. E. Carbon-1s Near-Edge-Absorption Fine Structure in Graphite. *Phys. Rev. B* **1993**, *48*, 2608–2610.

55. Domke, M.; Mandel, T.; Puschmann, A.; Xue, C.; Shirley, D. A.; Kaindl, G.; Petersen, H.; Kuske, P. Performance of the High-Resolution SX700/II Monochromator. *Rev. Sci. Instrum.* **1992**, *63*, 80–89.

56. Yamada, T.; Sekine, R.; Sawaguchi, T. Ultrahigh-Vacuum Multitechnique Study of AuCN Monolayers on Au(111) Formed by Electrochemical Deposition. *J. Chem. Phys.* **2000**, *113*, 1217–1227.

57. Han, P.; Weiss, P. S. Electronic Substrate-Mediated Interactions. *Surf. Sci. Rep.* **2012**, *67*, 19–81.

58. Wang, X.-B.; Wang, Y.-L.; Yang, J.; Xing, X.-P.; Li, J.; Wang, L.-S. Evidence of Significant Covalent Bonding in $Au(CN)_2^-$. *J. Am. Chem. Soc.* **2009**, *131*, 16368–16370.

59. Liu, H.-T.; Xiong, X.-G.; Diem Dau, P.; Wang, Y.-L.; Huang, D.-L.; Li, J.; Wang, L.-S. Probing the Nature of Gold–Carbon Bonding in Gold–Alkynyl Complexes. *Nat. Comm.* **2013**, *4*.

60. Smyth, C. P.; McAlpine, K. B. The Dipole Moments of Phosgene, Hydrogen Cyanide and Certain Substituted Methanes. *J. Am. Chem. Soc.* **1934**, *56*, 1697–1700.

61. Thomas, J. C.; Schwartz, J. J.; Hohman, J. N.; Claridge, S. A.; Auluck, H. S.; Serino, A. C.; Spokoyny, A. M.; Tran, G.; Kelly, K. F.; Mirkin, C. A.; Gilles, J.; Osher, S. J.; Weiss, P. S. Defect-Tolerant Aligned Dipoles within Two-Dimensional Plastic Lattices. *ACS Nano* **2015**, 9, 4734–4742.

62. Schwartz, J. J.; Mendoza, A. M.; Wattanatorn, N.; Zhao, Y.; Nguyen, V. T.; Spokoyny, A. M.; Mirkin, C. A.; Baše, T.; Weiss, P. S. Surface Dipole Control of Liquid Crystal Alignment. *J. Am. Chem. Soc.* **2016**, *138*, 5957–5967.

63. Bowmaker, G. A.; Kennedy, B. J.; Reid, J. C. Crystal Structures of AuCN and AgCN and Vibrational Spectroscopic Studies of AuCN, AgCN, and CuCN. *Inorg. Chem.* **1998**, *37*, 3968–3974.

64. Dameron, A. A.; Charles, L. F.; Weiss, P. S. Structures and Displacement of 1-Adamantanethiol Self-Assembled Monolayers on Au{111}. *J. Am. Chem. Soc.* **2005**, *127*, 8697–8704.

65. Beltramo, G. L.; Shubina, T. E.; Mitchell, S. J.; Koper, M. T. M. Cyanide Adsorption on Gold Electrodes: A Combined Surface Enhanced Raman Spectroscopy and Density Functional Theory Study. *J. Electroanal. Chem.* **2004**, *563*, 111–120.

66. Yan, C.; Gölzhäuser, A.; Grunze, M.; Wöll, C. Formation of Alkanethiolate Self-Assembled Monolayers on Oxidized Gold Surfaces. *Langmuir* **1999**, *15*, 2414–2419.

67. Ratner, B. D.; Castner, D. G. Electron Spectroscopy for Chemical Analysis. In *Surface Analysis – The Principal Techniques*, John Wiley & Sons, Ltd: **2009**; pp 47–112.

68. Cebula, I.; Lu, H.; Zharnikov, M.; Buck, M. Monolayers of Trimesic and Isophthalic Acid on Cu and Ag: The Influence of Coordination Strength on Adsorption Geometry. *Chem. Sci.* **2013**, *4*, 4455–4464.

69. Kunimatsu, K.; Seki, H.; Golden, W. G.; Gordon, J. G.; Philpott, M. R. A Study of the Gold/Cyanide Solution Interface by In Situ Polarization-Modulated Fourier Transform Infrared Reflection Absorption Spectroscopy. *Langmuir* **1988**, *4*, 337–341.

70. Max, P. B.; Scott, A. S.; Louis, J. A. The Infrared Spectra of Nitriles and Related Compounds Frozen in Ar and H_2O. *Astrophys. J* **1997**, *476*, 932.

71. Jobe, D. J.; Westaway, K. C. Fourier Transform Infrared Spectroscopy Studies of Cyanide Ion Solutions of Dimethylformamide and Aqueous Dimethylformamide. *Can. J. Chem.* **1993**, *71*, 1353–1361.

72. Senapati, D.; Dasary, S. S. R.; Singh, A. K.; Senapati, T.; Yu, H.; Ray, P. C. A Label-Free Gold-Nanoparticle-Based SERS Assay for Direct Cyanide Detection at the Parts-per-Trillion Level. *Chem. Eur. J.* **2011**, *17*, 8445–8451.

73. Keedy, C. R. The Rotational-Vibrational Spectra of HCN and DCN: A Physical Chemistry Experiment. *J. Chem. Educ.* **1992**, *69*, A296.

74. Pettinger, B.; Picardi, G.; Schuster, R.; Ertl, G. Surface-Enhanced and STM Tip-Enhanced Raman Spectroscopy of CN^- Ions at Gold Surfaces. *J. Electroanal. Chem.* **2003**, *554–555*, 293–299.

75. Neelakantan, P. Raman Spectrum of Acetonitrile. *Proc. Indian Acad. Sci. - Sect. A* **1964**, *60*, 422–424.

76. Kempgens, B.; Kivimäki, A.; Neeb, M.; Köppe, H. M.; Bradshaw, A. M.; Feldhaus, J. A High-Resolution N 1s Photoionization Study of the Molecule in the Near-Threshold Region. *J. Phys. B At., Mol., Opt.* **1996**, *29*, 5389.

77. Brühwiler, P. A.; Karis, O.; Mårtensson, N. Charge-Transfer Dynamics Studied Using Resonant Core Spectroscopies. *Rev. Mod. Phys.* **2002**, *74*, 703–740.

78. Schnadt, J.; Bruhwiler, P. A.; Patthey, L.; O'Shea, J. N.; Sodergren, S.; Odelius, M.; Ahuja, R.; Karis, O.; Bassler, M.; Persson, P.; Siegbahn, H.; Lunell, S.; Martensson, N. Experimental Evidence for Sub-3-fs Charge Transfer from an Aromatic Adsorbate to a Semiconductor. *Nature* **2002**, *418*, 620–623.

79. de Jong, M. P.; Friedlein, R.; Sorensen, S. L.; Öhrwall, G.; Osikowicz, W.; Tengsted, C.; Jönsson, S. K. M.; Fahlman, M.; Salaneck, W. R. Orbital-Specific Dynamic Charge Transfer from Fe(II)-Tetraphenylporphyrin Molecules to Molybdenum Disulfide Substrates. *Phys. Rev. B* **2005**, *72*, 035448.

80. Fohlisch, A.; Feulner, P.; Hennies, F.; Fink, A.; Menzel, D.; Sanchez-Portal, D.; Echenique, P. M.; Wurth, W. Direct Observation of Electron Dynamics in the Attosecond Domain. *Nature* **2005**, *436*, 373–376.

81. Piancastelli, M. N. Auger Resonant Raman Studies of Atoms and Molecules. *J. Electron. Spectrosc. Relat. Phenom.* **2000**, *107*, 1–26.

CHAPTER 3:

Hexagons to Ribbons:

Flipping Cyanide on Au{111}

3.1 Introduction

Directing the self-organization of molecular systems requires understanding the effects of changing the basic parameters and external stimuli, such as temperature, electrical potential, and illumination on molecular and intermolecular structure and function.[1-5] Self-assembled monolayers are a common system to test these effects, which can result in both physical and chemical changes.[6-9] Similar to thiols and selenols, carbon-bound molecules have been shown to form ordered monolayers on gold substrates.[10-14] The strength of the Au-C bond is similar in strength to the Au-S and Au-Se bonds.[13,14] There is significant interest in understanding how temperature affects the organization,[6,15-17] conductivity,[17] adsorption,[18] stability,[13,19] and molecular reactivity[20] of self-assembled monolayers, which are critical in effectively tailoring molecular design for research and applications in nanotechnology.[4,21,22]

Monolayer structures can be elucidated through vibrational spectroscopy,[10,23-26] molecular-resolution imaging,[27-30] and complementary techniques. Even relatively small shifts of vibration peaks can be sources of significant information pertaining to the morphology,[24,31] structure,[10,32-35] composition, and defects of self-assembled monolayers.[24,36,37] To this end, we have fabricated and probed the vibrational spectra and structures of monolayers of cyanide molecules on Au{111}.[7,38] In this work, we report the structure and orientation for annealed cyanide monolayers on Au{111}, report changes in the vibrational spectra, and propose mixed bonding schemes to explain the appearance of 'ribbons' consisting of rows of cyanide molecules.

Initially, cyanide molecules deposited at room temperature assemble on Au{111} in a hexagonally close-packed lattice attached through the carbon atom, that are oriented primarily normal to the surface.[38] Cyanide has a strong dipole moment of 2.8 D that makes it ideal as a small-molecule probe.[39,40] In our previous work we adsorbed cyanogen (C_2N_2) on Au{111}, but it

did not dissociate under the conditions used.[41] Here, we were able to deposit CN on Au{111} and to induce a structural change upon a simple dry thermal annealing process.

3.2 Results and Discussion

3.2.1 Surface Structure Characterization of Thermally Annealed CN/Au{111}

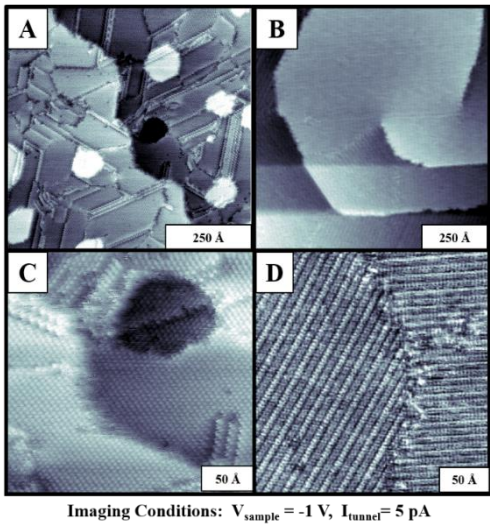

Figure 3.1. Scanning tunneling microscope images of (A) hexagonally close-packed (hcp) CN/Au{111} as-deposited under ambient conditions and (B) the thermally induced ribbon structure formed by dry annealing for over 18 h at ~100 °C. The order in the annealed structure is long range (on the order of tens of nanometers) with the ribbon domains taking on various rotational orientations relative to one another on the surface. Once annealed, the surface never returns to the original hcp arrangement. (C,D) Molecular-resolution images of the as-adsorbed and thermally annealed lattices, respectively. We note tip-change imaging artifacts in (B) that did not disrupt the topography.

Cyanide molecules deposited on Au{111} from exposure to HCN(*g*) under atmospheric conditions order in a hexagonal close-packed lattice (hcp) at room temperature.[38] Figure 3.1A shows the structural details of cyanide monolayers, obtained under standard ambient conditions by STM, which include surface features such as vacancy islands, protruding islands, and multiple highly ordered domains. In this cyanide on Au{111} structure, the measured nearest-neighbor spacing is 3.8 ± 0.5 Å.[38]

After heating as-adsorbed CN/Au{111} samples to 100 °C for over 18 h, the original surface features are completely replaced, as shown in Figure 3.1B, with ribbon-like structural domains that are typically larger, spanning tens to hundreds of nanometers, than those observed prior to thermal annealing, which are on the order of 1–10 nm. Closer inspection of the surface structure reveals the changes at the molecular level from the initial CN/Au{111} hcp lattice, shown in Figure 3.1C, to the new ribbon arrangement, shown in Figure 3.1D. Two common defects found in the ribbon system are highlighted in Figure 3.1D, molecular-level disruptions of the individual ribbon 'stripes' and domain boundaries between regions of different surface orientation. Once converted, the ribbon structure has not been observed to return to the hcp lattice, and has been stable for imaging for several months using standard storage conditions (i.e., in a dark, dry, sealed container).

Annealing up to 60 °C for over 18 h induced no observable change in the as-adsorbed CN/Au{111} hcp lattice, while annealing to 100 ± 5 °C induces ribbon formation, usually to completion. Using this same temperature window, ribbon emergence is typically observed after 6 h when both structures can be observed, as in Figure 3.2A, to coexist on the surface. Single-molecule resolution of this system with STM, in Figure 3.2B, shows both the hcp lattice in the top right corner and the emergence of the ribbon region in the bottom left with isolated

molecule features appearing in both regions that are not part of the respective lattices. Importantly, annealing for over 18 h does not affect the ribbon structure; annealing periods of 24 h were typically used to ensure complete conversion. However, annealing at temperatures above 105 °C for 18–24 h generally results in deterioration of the sample. This observation agrees with the established temperature dependence of gold dissolution, which reports the decomposition of cyanide in aqueous solutions with gold at temperatures above 100 °C,[42-44] however, the thermal decomposition for polymeric AuCN complexes has been reported to occur at temperatures above 350 °C.[45] Thus, it is possible that restructuring competes with the predicted decomposition mechanism in which the as-adsorbed CN/Au{111} is hydrolyzed by atmospheric water vapor.[42]

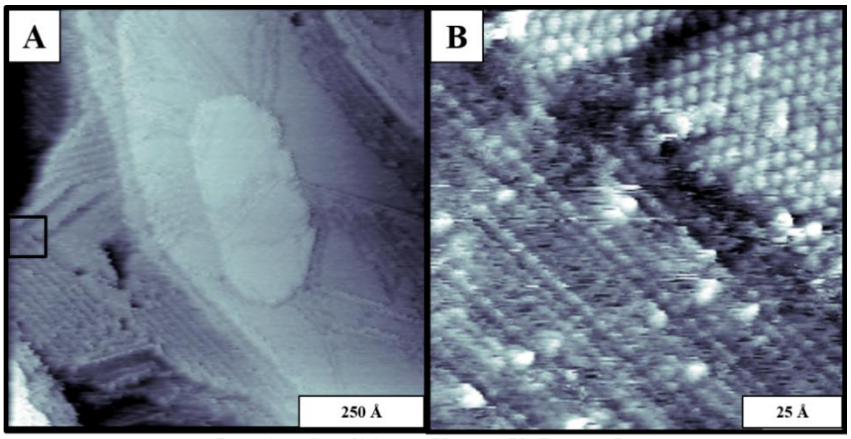

Imaging Conditions: V_{tip} = 1 V, I_{tunnel}= 5 pA

Figure 3.2. (A) The transition from hexagonally close-packed to ribbon structure was imaged after 6 h exposure to ~100 °C. (B) A higher resolution image highlights a region with both (upper right) hexagonally close-packed and (lower left) ribbon structure regions.

Segmentation analysis,[46-49] which takes into account all information in the images, was used to highlight the information pertaining to the ribbon orientation of the annealed CN/Au{111} system. Ribbon domains were observed to be rotationally offset from one another separated by topologically distinct boundaries as shown in Figure 3.3A, a STM image of annealed CN/Au{111}. Information based on the analysis of detected Fourier modes (see Appendix for Supplementary Information) reveals, as shown in Figures 3.3B and 3.3C, the orientations of the different domains, identifies the domain boundaries, and detects Au{111} step edges. The measured angles between the different ribbon domains are all calculated to be multiples of 60° indicating that ribbon direction is significantly influenced by the hexagonal symmetry of the underlying gold substrate.

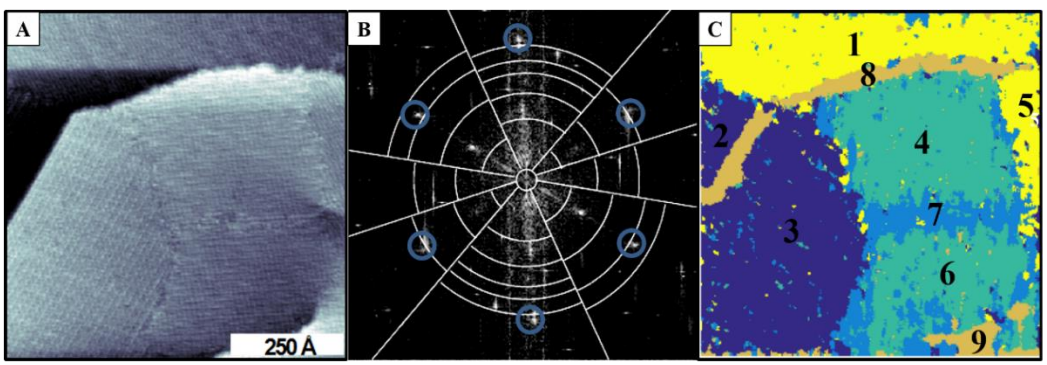

Imaging Conditions: V_{sample} = -1 V, I_{tunnel} = 5 pA

Figure 3.3. (A) A scanning tunneling microscope image of the annealed CN/Au{111} with six separate ribbon domains with three different relative rotations of the ribbon direction. (B) The associated segmented image partitioned in the Fourier domain highlighting the three different orientations. (C) Regions 1–6 represent ribbon regions with each color indicating a ribbon region of a different rotational orientation. Region 7 is a ribbon domain boundary, and regions 8, 9 are step edges. Ribbon orientations are relatively offset by rotations of multiples of 60° following the hexagonal close-packed symmetry of the underlying gold lattice.

Segmentation analysis was further utilized on the molecular-resolution STM image in Figure 3.4A to isolate the three distinct regions shown in Figure 3.4B that compose the ribbons.[46-49] The regions identified as 1 and 2 in the segmented image are two separate ribbon regions that are offset by 120°. Region 3 is an example of a typical domain boundary between two orientation domains observed to be a topographically distinct molecular region. Within region 1, three distinct rows compose the ribbon features along with disordered portions disrupting the continuity of the ribbons. These disordered molecular regions are similar in structure to the molecules observed in the domain boundary.

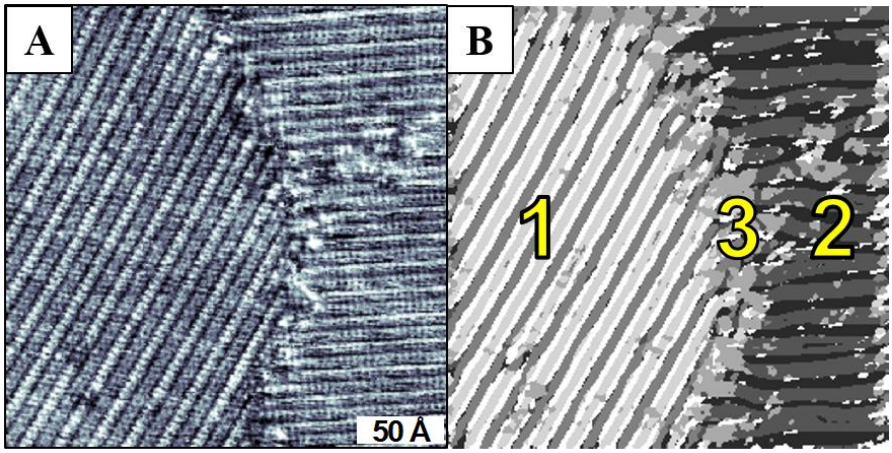

Imaging Conditions: V_{sample} = -1 V, I_{tunnel}= 5 pA

Figure 3.4. (A) Scanning tunneling microscope image of the region of thermally annealed CN/Au{111} with a domain boundary separating rotational domains. (B) Segmentation analysis results showing the domain boundary (3) and the rotational domains (1 and 2).

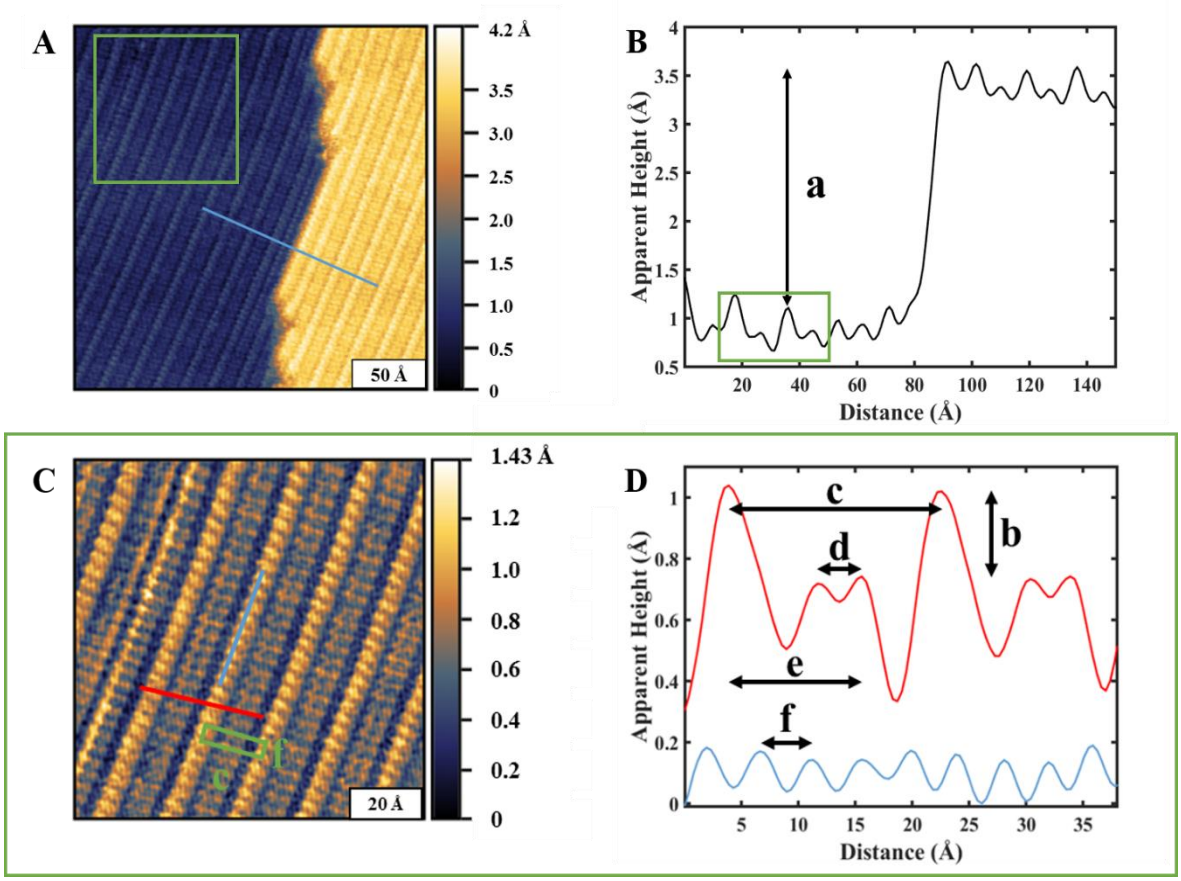

Figure 3.5. (A,C) Scanning tunneling microscope images of the ribbon structures of annealed CN on Au{111} (false colored to highlight the relative apparent height differences and lateral distances). (B) Surface profile shown as the blue line in (A) showing the apparent height variations of the ribbon structure of annealed CN on Au{111} and a step edge, which is used as an internal reference. (C) A higher resolution image of the area indicated in (A) with the unit cell shown as the green box. (D) Corresponding surface profiles along and across the rows shown in (B,D). Letters a-f correspond to the measured distances summarized in Table 3.1. Imaging conditions: V_{sample} = -1 V, I_{tunnel} = 5 pA.

Table 3.1. Measured distances for annealed CN/Au{111} corresponding to the profiles

Feature	Lateral Distance (Å)	Apparent Height (Å)
a	-	2.39 ± 0.09
b	-	0.33 ± 0.09
c	18.1 ± 0.1	-
d	3.5 ± 0.4	-
e	11.5 ± 0.2	-
f	3.8 ± 0.4	-

Positions of the molecules within the different ribbon regions were analyzed to develop a structural model. The STM images in Figure 3.5, along with corresponding surface profiles, were used to generate the lattice spacing and apparent height information summarized in Table 3.1. Figures 3.5A and 3.5B show the expected apparent height of a typical step edge on the Au{111} surface. Using this as an internal reference, the relative apparent height difference between two adjacent rows of the ribbons measures at 0.33±0.09 Å. This measurement is close to the published experimental and calculated results for the difference between Au-C and Au-N bond lengths in solid, crystalline AuCN, in which the Au-C bond is reported as longer.[50] Lateral distances for the ribbon structure are also summarized in Table 3.1, and correspond to letters a-f from the profiles of Figure 3.5C shown in Figure 3.5D. Note that all of the observed lateral distances are within experimental error of the lattice constant we measured for the initial as-adsorbed CN/Au{111} and take into account at least 10 independent samples using over 50 images suggesting that the upright orientations of the molecules are maintained. This result is further supported by vibrational spectroscopic results discussed below.

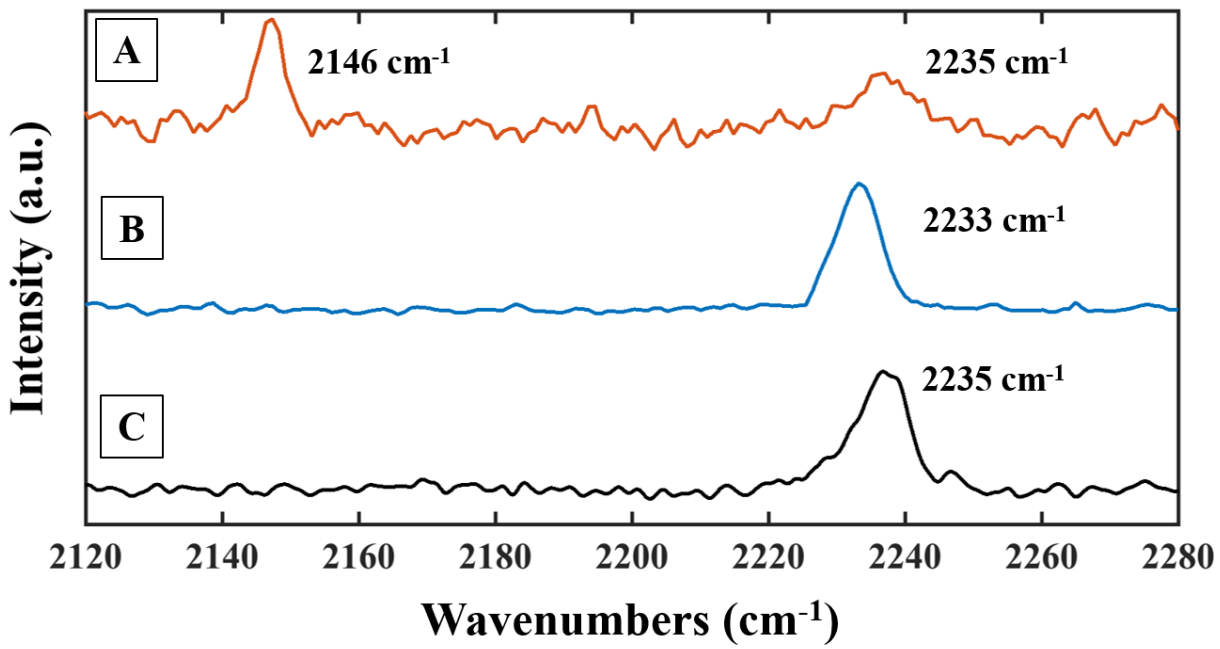

Figure 3.6. Attenuated total reflection infrared spectra of CN/Au{111} (A) after 6 h of thermal annealing at 100 °C and (B) after 24 h of thermal annealing at ~100 °C. (C) Polarization modulation-infrared absorption spectroscopy for CN/Au/Si after 24 h of thermal annealing at 100 °C.

The vibrational structure was analyzed to construct a structural model for annealed cyanide SAMs on Au{111}. The process of annealing monolayers of CN on Au{111} results in a blue shift of the frequency of the CN vibration. Cyanide molecules initially adsorbed on Au{111} at room temperature exhibit a peak at 2146 cm^{-1} using attenuated total reflection-infrared spectroscopy (ATR-IR), which was in good agreement with the typical blue shift expected from the free cyanide ion in solution.[38,40,51] The character of the Au-CN bond is typically considered to be of partially covalent character in gold-cyanide coordination complexes with the bond strength exceeding that of Au-S.[7,13,52,53] Alkanethiol SAMs exhibit mobility on the surface,[7,54] and the same can be suggested for cyanide monolayers. After 6 h of heating at 100 °C, the spectrum in Figure 3.6A

shows a new peak at 2235 cm^{-1} along with original as-adsorbed peak. The new peak is within the expected range for highly covalent Au-C bound CN.[38,50,55] Additional heating, typically after 18 h, generates a spectrum as seen in Figure 3.6B where the original peak has disappeared. Interestingly, the IR spectrum did not contain a separate measurable peak for the weaker Au-NC bound molecules, and no other peaks were observed in regions indicating new bond formation. Breaking the CN bond and/or desorption of the CN molecules from the surface would result in complete loss of the detected vibrational mode in the region of interest. As described below, surface-enhanced Raman spectroscopy is able to detect the additional spectral features.

The orientation of the cyanide molecules in the annealed system was determined through the use polarization-modulation infrared spectroscopy (PM-IRRAS). The selection rules for PM-IRRAS require that only the interaction with dipoles oriented normal to the surface will be detected.[56] Because of challenges due to rigidity and the thinness of the molecular layer and specular reflection from the flatness of the Au{111}, we used polycrystalline Au/Si (as opposed to Au on mica for STM measurements) for PM-IRRAS measurements (see Supplementary Information in Appendix). Figure 3.6C shows the PM-IRRAS spectra for annealed CN/Au{111}, along with ATR-IR spectra for the as-adsorbed and annealed cyanide monolayers. Apart from the small deviation (2 cm^{-1}) between the annealed ATR-IR and PM-IRRAS, the spectra were in good agreement indicating that bonding interpretations based on spectral analysis should be valid for both systems. After thermal annealing, the results suggest that the molecules are oriented normal to the surface.

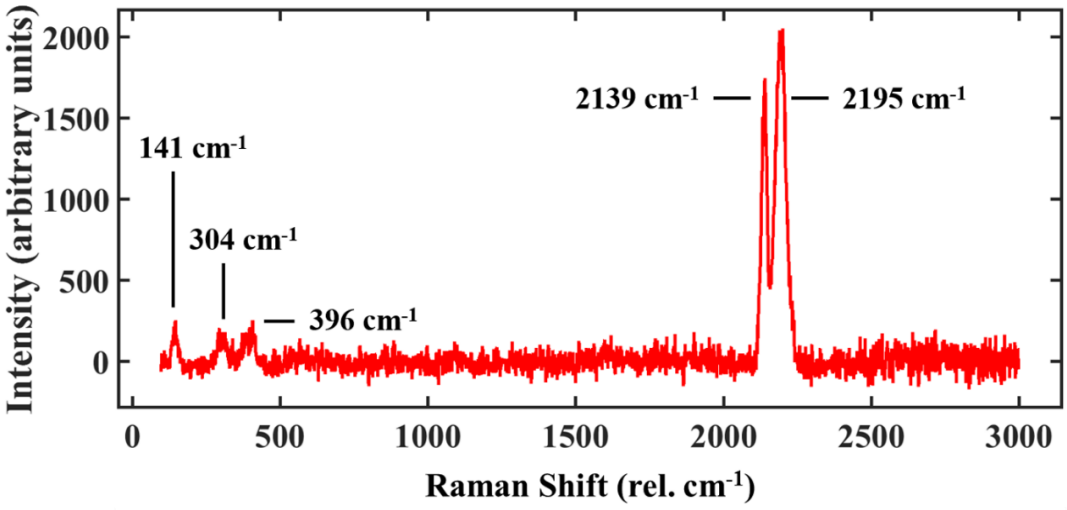

Figure 3.7. Raman spectrum showing both the low and high frequency modes of CN/Au{111} after thermal annealing for over 24 h at ~100 °C. The most important aspects of the spectrum are the new peaks at 141 and 2195 cm^{-1} without loss of the vibrations that are also detected on the as-adsorbed sample.

Substrate-adsorbate modes for cyanide bound to gold surfaces are found in the low frequency region, ~100-500 cm^{-1}, of the Raman spectrum.[50,53] The surface-enhanced Raman spectra of cyanide SAMs on Au{111} after annealing for 24 h at 100 °C are shown in Figure 3.7 with the typical vibrational modes, also observed in the as-deposited monolayers, which are known to be characteristic of Au-CN bonding. The values of 304 and 396 cm^{-1}, representing the Au-CN stretch and Au-CN bend, are red shifted by 10 cm^{-1} in comparison to the initial as-adsorbed cyanide.[50,53,57,58] An additional low frequency peak is observed at 141 cm^{-1}, a value that is close to the Au-NC vibrational frequency reported for the Au-NC containing hexagonally bundled, linear AuCN chains of the solid crystal.[50] Furthermore, a second, blue-shifted peak is observed in the region of the CN vibrational frequency at 2195 cm^{-1}, which is also close to the reported value for

the same crystalline structure (see Supplementary Information in Appendix Figure A6 for a comparison with the as-deposited system).[50]

3.2.2 Bonding Model for Annealed Cyanide Bonding on Au{111}

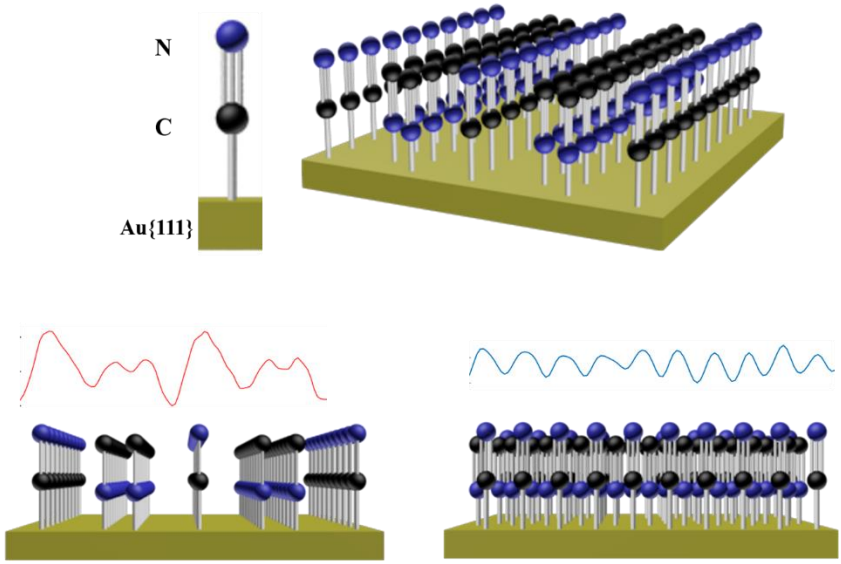

Figure 3.8. Proposed bonding scheme for annealed cyanide SAMs on Au{111} composed of a mixture of Au-CN and Au-NC bound molecules. Surface profiles that match the scanning tunneling microscope image shown in Figure 3.5 are aligned with the schematic for comparison.

Combining the structural and vibrational characterization, we propose a bonding scheme, shown in Figure 3.8, to describe the annealed CN/Au{111} ribbon structure. The alternating regions of oppositely oriented molecules were constructed using the 0.33 Å different in relative height to match the measurement that closely matches the reported distance difference between longer Au-C and shorter Au-N bond lengths in the AuCN crystal.[50] In the annealed structure, two rows of Au-CN are separated on each side from a row of Au-NC by a single-molecule-wide

vacancy row (bottom left of Figure 3.8). In this arrangement, the molecules maintain the pre-annealing lattice spacing[38] and match the measured unit cell containing three molecules (3.8 Å × 18.1 Å) shown previously in Figure 3.5C.

In nitrile SAMs on Au{111}, unfavorable dipole-dipole interactions are minimized when the functional group assumes an orientation almost parallel to the substrate enabling a tip-to-tail configuration.[1,14,59,60] Dipole-dipole interactions between inverted adjacent rows would be favorable after the inversion of the cyanide molecules from Au-CN to Au-NC, but the other energetics have to be considered as well. Only calculations on infinite, linear AuCN chains of the crystalline structure have reported the Au-NC vibrational frequency.[50] Also consistent with this model is the higher frequency CN vibration that is typically associated with a significantly covalent bonding environment, which is reported for gold-cyanide complexes, frequently found in nitriles, and reported for solid, crystalline AuCN.[50,55,61-63]

3.3 Conclusions and Prospects

Cyanide monolayers that are initially hexagonally close-packed when deposited at room temperature form a ribbon structure after thermal annealing for over 18 h at 100 °C on Au{111}. In this arrangement, molecules assume positions in 'striped' regions with stripes that follow the hexagonal symmetry of the underlying gold substrate. Images of annealed CN/Au{111} reveal regions within the ribbons that have a relative height difference that is in agreement with calculated and experimentally determined differences between bond lengths of the longer Au-CN and shorter Au-NC bonding schemes.[50] Infrared spectroscopic measurements indicate the CN vibration shifts from 2146 to 2233 cm^{-1} while maintaining an upright orientation. Surface-enhanced Raman spectroscopy reveals an *additional* substrate-adsorbate bonding mode that is consistent with the

observed Au-N bonding mode in linear AuCN crystalline chains along with a doublet in the high frequency region, suggesting another chemical state exists that we attribute to Au-NC. Ribbon regions of similar apparent height measures in multiples of the cyanide molecule lattice constant of ~3.8 Å. We conclude by proposing a bonding scheme consisting of a mixed monolayer of upright cyanide and isocyanide molecules on the surface that is the result of a thermally induced process crystallizing the surface similar to what is found in solid AuCN. Such control of orientation may ultimately be of use in templating the growth of one- and two-dimensional materials on substrates.[64,65]

3.4 Experimental Methods

3.4.1 Monolayer Preparation

Au{111}/mica substrates (150 nm of Au{111}, Agilent Technologies) are hydrogen flame annealed as described previously to clean the surface and to increase the size of the atomically flat terraces.[7,66] Monolayers of cyanide were prepared for STM measurements by placing 0.1 mg of solid KCN (≥96%, Sigma Aldrich) stored in a desiccator, without any further purification or treatment, in a glass vial with the Au{111}/mica substrate for 24 h at room temperature.[38] **Caution: KCN is highly toxic and produces the volatile and flammable HCN(*g*) when it reacts with water and oxygen. It should be used with proper personal protective equipment, in a fume hood, and kept out of extreme temperatures.** Afterwards, the Au{111}/mica substrate was transferred to the vial with the KCN, transferred to a clean glass vial, and allowed to rest in the fume hood for 1 h before being placed in an oven for annealing at 100 °C for either 6 h, 18 h, or 24 h. Following annealing, the samples are allowed to cool to room temperature and placed directly into the STM for imaging without further treatment.

3.4.2 Scanning Tunneling Microscopy

A custom-built, Besocke-style STM was used under standard ambient conditions using custom cut Pt/Ir tips (80:20).[16,67] All STM images were calibrated against known references: Au{111} step edges for height and a decanethiol on Au{111} matrix for lateral distance measurements.[16] Unless otherwise specified, all samples were held at -1 V bias with a 5 pA tunneling current and image resolution of 256 × 256 pixels.

3.4.3 Infrared Spectroscopy

Infrared spectroscopy was collected using a Thermo-Fisher Nicolet 8700 Interferometer (Thermo-Fisher Scientific, Waltham, MA) and the packaged OMNIC Software (Thermo-Fisher Scientific). The OMNIC software was also used for processing the spectra and identifying peak positions. All IR samples were incubated with KCN and annealed in the same manner as described for the STM samples. The entire beam path was purged with flowing N_2 and a liquid-nitrogen-cooled mercury cadmium telluride detector was used to record spectra with a resolution of 2 cm^{-1}. Polarization-modulation infrared reflection absorption spectroscopy used custom Au/Cr/Si samples with an 80° grazing incident angle. Shown in the supplementary material in the Appendix (Figure A5) is the evidence that the spectral feature related to the CN bond vibrational frequency is the same on Au{111} and polycrystalline Au/Cr/Si. Silicon substrates were deposited with a 10-nm Cr adhesion layer deposited at 3Å/s and a 100-nm-thick layer of Au also deposited also at 3 Å/s. For collecting infrared spectrum on Au{111}, we used custom-made Au{111}/sapphire prism substrates. Prism substrates were 0.5-cm radius, 1-cm-high sapphire c-cut half-cylinders with a 2-nm-thick Nb adhesion layer deposited at 0.11 Å/s and a 40-nm-thick layer of Au, which is well below the optical penetration depth for metals in the range of the IR frequencies of interest,

deposited at a rate of 0.5 Å/s. A bare Au{111}/sapphire prism sample was used for the background spectrum and an incident angle $\theta = 60° > \theta_c = 34.6°$ as measured relative to surface normal (the critical angle is calculated using n=1.76). After incubation and annealing, both STM and IR samples were directly analyzed without rinsing.

3.4.4 Raman Spectroscopy

Surface-enhanced Raman spectroscopy (SERS) was performed on a Renishaw confocal Raman microscope (Renishaw, Inc., Hoffman Estates, Illinois) configured with a laser at 514 nm wavelength, using WiRE 3.2 (Renishaw, Inc.) for spectral processing and analysis. Two substrates designed for surface enhancement were used in this work: Au{111}/mica with nanohole arrays and nanostructured Au on glass. The nanohole arrays (175 nm diameter, 300 nm periodicity) on Au{111}/mica were fabricated using a focused ion beam.[25] The nanostructured Au on glass substrates were made by evaporating 50 Å thick Au at 1 Å/s onto a glass slide and annealing at 400 °C for 24 h. All the SERS substrates were incubated with solid KCN and annealed in the same manner as the STM/IR samples.

3.4.5 Image Analysis

All image analyses were performed with either our custom software,[67] Gwyddion (http://gwyddion.net/), or Matlab. The segmentation utilizing the empirical wavelet transform and variational methods as described in the supplementary information. The empirical wavelet toolbox is available online through the Mathworks file exchange, "Empirical Wavelet Toolbox". [46-48]

3.5 References

1. Heister, K.; Zharnikov, M.; Grunze, M.; Johansson, L. S. O.; Ulman, A. Characterization of X-ray Induced Damage in Alkanethiolate Monolayers by High-Resolution Photoelectron Spectroscopy. *Langmuir* **2001**, *17*, 8–11.

2. Weiss, P. S. Functional Molecules and Assemblies in Controlled Environments: Formation and Measurements. *Acc. Chem. Res.* **2008**, *41*, 1772–1781.

3. Han, P.; Weiss, P. S. Electronic Substrate-Mediated Interactions. *Surf. Sci. Rep.* **2012**, *67*, 19–81.

4. Pathem, B. K.; Claridge, S. A.; Zheng, Y. B.; Weiss, P. S. Molecular Switches and Motors on Surfaces. *Ann. Rev. Phys. Chem.* **2013**, *64*, 605–630.

5. Abendroth, J. M.; Bushuyev, O. S.; Weiss, P. S.; Barrett, C. J. Controlling Motion at the Nanoscale: Rise of the Molecular Machines. *ACS Nano* **2015**, *9*, 7746–7768.

6. Yamada, R.; Wano, H.; Uosaki, K. Effect of Temperature on Structure of the Self-Assembled Monolayer of Decanethiol on Au(111) Surface. *Langmuir* **2000**, *16*, 5523–5525.

7. Love, J. C.; Estroff, L. A.; Kriebel, J. K.; Nuzzo, R. G.; Whitesides, G. M. Self-Assembled Monolayers of Thiolates on Metals as a Form of Nanotechnology. *Chem. Rev.* **2005**, *105*, 1103–1170.

8. Moore, A. M.; Yeganeh, S.; Yao, Y.; Claridge, S. A.; Tour, J. M.; Ratner, M. A.; Weiss, P. S. Polarizabilities of Adsorbed and Assembled Molecules: Measuring the Conductance through Buried Contacts. *ACS Nano* **2010**, *4*, 7630–7636.

9. Zhang, Z.; Kim, H.; Noh, J.; Ahn, Y.; Son, J. Y.; Jang, J. Thermal Curing of a Self-Assembled Monolayer at the Nanoscale. *Nanoscale* **2016**, *8*, 1133–1139.

10. Joo, S.-W.; Kim, W.-J.; Yun, W. S.; Hwang, S.; Choi, I. S. Binding of Aromatic Isocyanides on Gold Nanoparticle Surfaces Investigated by Surface-Enhanced Raman Scattering. *App. Spec.* **2004**, *58*, 218–223.

11. Monnell, J. D.; Stapleton, J. J.; Jackiw, J. J.; Dunbar, T.; Reinerth, W. A.; Dirk, S. M.; Tour, J. M.; Allara, D. L.; Weiss, P. S. Ordered Local Domain Structures of Decaneselenolate and Dodecaneselenolate Monolayers on Au{111}. *J. Phys. Chem. B.* **2004**, *108*, 9834–9841.

12. Swanson, S. A.; McClain, R.; Lovejoy, K. S.; Alamdari, N. B.; Hamilton, J. S.; Scott, J. C. Self-Assembled Diisocyanide Monolayer Films on Gold and Palladium. *Langmuir* **2005**, *21*, 5034–5039.

13. Crudden, C. M.; Horton, J. H.; Ebralidze, I. I.; Zenkina, O. V.; McLean, A. B.; Drevniok, B.; She, Z.; Kraatz, H.-B.; Mosey, N. J.; Seki, T.; Keske, E. C.; Leake, J. D.; Rousina-Webb, A.; Wu, G. Ultra Stable Self-Assembled Monolayers of N-Heterocyclic Carbenes on Gold. *Nat Chem* **2014**, *6*, 409–414.

14. Ossowski, J.; Wächter, T.; Silies, L.; Kind, M.; Noworolska, A.; Blobner, F.; Gnatek, D.; Rysz, J.; Bolte, M.; Feulner, P.; Terfort, A.; Cyganik, P.; Zharnikov, M. Thiolate versus Selenolate: Structure, Stability, and Charge Transfer Properties. *ACS Nano* **2015**, *9*, 4508–4526.

15. Parikh, A. N.; Allara, D. L.; Azouz, I. B.; Rondelez, F. An Intrinsic Relationship between Molecular Structure in Self-Assembled n-Alkylsiloxane Monolayers and Deposition Temperature. *J. Phys. Chem.* **1994**, *98*, 7577–7590.

16. Bumm, L. A.; Arnold, J. J.; Charles, L. F.; Dunbar, T. D.; Allara, D. L.; Weiss, P. S. Directed Self-Assembly to Create Molecular Terraces with Molecularly Sharp Boundaries in Organic Monolayers. *J. Am. Chem. Soc.* **1999**, *121*, 8017–8021.

17. Hohman, J. N.; Kim, M.; Schüpbach, B.; Kind, M.; Thomas, J. C.; Terfort, A.; Weiss, P. S. Dynamic Double Lattice of 1-Adamantaneselenolate Self-Assembled Monolayers on Au{111}. *J. Am. Chem. Soc.* **2011**, *133*, 19422–19431.

18. Chen, D.; Sarid, D. Temperature Effects of Adsorption of C_{60} Molecules on Si(111)-(7 X 7) Surfaces. *Phys. Rev. B.* **1994**, *49*, 7612–7619.

19. Delamarche, E.; Michel, B.; Kang, H.; Gerber, C. Thermal Stability of Self-Assembled Monolayers. *Langmuir* **1994**, *10*, 4103–4108.

20. Schönherr, H.; Feng, C.; Shovsky, A. Interfacial Reactions in Confinement: Kinetics and Temperature Dependence of Reactions in Self-Assembled Monolayers Compared to Ultrathin Polymer Films. *Langmuir* **2003**, *19*, 10843–10851.

21. Furst, E. M. Directed Self-Assembly. *Soft Matter* **2013**, *9*, 9039–9045.

22. Han, P.; Akagi, K.; Federici Canova, F.; Shimizu, R.; Oguchi, H.; Shiraki, S.; Weiss, P. S.; Asao, N.; Hitosugi, T. Self-Assembly Strategy for Fabricating Connected Graphene Nanoribbons. *ACS Nano* **2015**, *9*, 12035–12044.

23. Hoffmann, H.; Mayer, U.; Brunner, H.; Krischanitz, A. Reflection-Absorption Infrared Spectroscopy of Self-Assembled Monolayers on Gold and Silicon Surfaces. *Vib. Spec.* **1995**, *8*, 151–157.

24. Dunbar, T. D.; Cygan, M. T.; Bumm, L. A.; McCarty, G. S.; Burgin, T. P.; Reinerth, W. A.; Jones, L.; Jackiw, J. J.; Tour, J. M.; Weiss, P. S.; Allara, D. L. Combined Scanning Tunneling Microscopy and Infrared Spectroscopic Characterization of Mixed Surface Assemblies of Linear Conjugated Guest Molecules in Host Alkanethiolate Monolayers on Gold. *J. Phys. Chem. B.* **2000**, *104*, 4880–4893.

25. Zheng, Y. B.; Payton, J. L.; Chung, C.-H.; Liu, R.; Cheunkar, S.; Pathem, B. K.; Yang, Y.; Jensen, L.; Weiss, P. S. Surface-Enhanced Raman Spectroscopy to Probe Reversibly Photoswitchable Azobenzene in Controlled Nanoscale Environments. *Nano Lett.* **2011**, *11*, 3447–3452.

26. Jiang, N.; Foley, E. T.; Klingsporn, J. M.; Sonntag, M. D.; Valley, N. A.; Dieringer, J. A.; Seideman, T.; Schatz, G. C.; Hersam, M. C.; Van Duyne, R. P. Observation of Multiple Vibrational Modes in Ultrahigh Vacuum Tip-Enhanced Raman Spectroscopy Combined with Molecular-Resolution Scanning Tunneling Microscopy. *Nano Letters* **2012**, *12*, 5061–5067.

27. Stranick, S. J.; Parikh, A. N.; Tao, Y. T.; Allara, D. L.; Weiss, P. S. Phase Separation of Mixed-Composition Self-Assembled Monolayers into Nanometer Scale Molecular Domains. *J. Phys. Chem.* **1994**, *98*, 7636–7646.

28. Poirier, G. E. Characterization of Organosulfur Molecular Monolayers on Au(111) using Scanning Tunneling Microscopy. *Chem. Rev.* **1997**, *97*, 1117–1128.

29. Han, P.; Kurland, A. R.; Giordano, A. N.; Nanayakkara, S. U.; Blake, M. M.; Pochas, C. M.; Weiss, P. S. Heads and Tails: Simultaneous Exposed and Buried Interface Imaging of Monolayers. *ACS Nano* **2009**, *3*, 3115–3121.

30. Hohman, J. N.; Zhang, P.; Morin, E. I.; Han, P.; Kim, M.; Kurland, A. R.; McClanahan, P. D.; Balema, V. P.; Weiss, P. S. Self-Assembly of Carboranethiol Isomers on Au{111}: Intermolecular Interactions Determined by Molecular Dipole Orientations. *ACS Nano* **2009**, *3*, 527–536.

31. Hostetler, M. J.; Stokes, J. J.; Murray, R. W. Infrared Spectroscopy of Three-Dimensional Self-Assembled Monolayers: N-Alkanethiolate Monolayers on Gold Cluster Compounds. *Langmuir* **1996**, *12*, 3604–3612.

32. Dubois, L. H.; Nuzzo, R. G. Synthesis, Structure, and Properties of Model Organic Surfaces. *Ann. Rev. Phys. Chem.* **1992**, *43*, 437–463.

33. Allara, D. L.; Parikh, A. N.; Rondelez, F. Evidence for a Unique Chain Organization in Long Chain Silane Monolayers Deposited on Two Widely Different Solid Substrates. *Langmuir* **1995**, *11*, 2357–2360.

34. Pascual, J. I.; Jackiw, J. J.; Song, Z.; Weiss, P. S.; Conrad, H.; Rust, H. P. Adsorbate-Substrate Vibrational Modes of Benzene on Ag(110) Resolved with Scanning Tunneling Spectroscopy. *Phys. Rev. Lett.* **2001**, *86*, 1050–1053.

35. Rosenbaum, A. W.; Freedman, M. A.; Darling, S. B.; Popova, I.; Sibener, S. J. Surface Vibrations in Alkanethiol Self-Assembled Monolayers of Varying Chain Length. *J. Chem. Phys.* **2004**, *120*, 3880–3886.

36. Haensch, C.; Hoeppener, S.; Schubert, U. S. Chemical Modification of Self-Assembled Silane Based Monolayers by Surface Reactions. *Chem. Soc. Rev.* **2010**, *39*, 2323–2334.

37. Elliott, A. B. S.; Horvath, R.; Gordon, K. C. Vibrational Spectroscopy as a Probe of Molecule-Based Devices. *Chem. Soc. Rev.* **2012**, *41*, 1929–1946.

38. Guttentag, A.; Wächter, T.; Barr, K.; Abendroth, J. M.; Song, T.-B.; Yang, Y.; Allara, D. L.; Zharnikov, M.; Weiss, P. S. Precious Poision: The Self-Assembly of Cyanide on Au{111}. *unpublished* **2016**.

39. Iguchi, K. Dipole Moment of the HCN Molecule. *J. Chem. Phys.* **1956**, *25*, 217–219.

40. Keedy, C. R. The Rotational-Vibrational Spectra of HCN and DCN: A Physical Chemistry Experiment. *J. Chem. Educ.* **1992**, *69*, A296.

41. Han, P.; Sykes, E. C. H.; Pearl, T. P.; Weiss, P. S. A Comparative Scanning Tunneling Microscopy Study of Physisorbed Linear Quadrupolar Molecules: C_2N_2 and CS_2 on Au{111} at 4 K. *J. Phys. Chem. A* **2003**, *107*, 8124–8129.

42. van Deventer, J. S. J.; van der Merwe, P. F. The Effect of Temperature on the Desorption of Gold Cyanide from Activated Carbon. *Thermochim. Acta* **1993**, *221*, 99–113.

43. Cherevko, S.; Zeradjanin, A. R.; Topalov, A. A.; Keeley, G. P.; Mayrhofer, K. J. J. Effect of Temperature on Gold Dissolution in Acidic Media. *J. Electrochem. Soc.* **2014**, *161*, H501–H507.

44. Snyders, C. A.; Bradshaw, S. M.; Akdogan, G.; Eksteen, J. J. The Effect of Temperature, Cyanide and Base Metals on the Adsorption of Pt, Pd and Au onto Activated Carbon. *Hydrometallurgy* **2014**, *149*, 132–142.

45. Akhtar, M. N.; Isab, A. A.; Hassan, A. Thermal Decomposition of Trialkyl/Arylphosphine Gold(I) Cyanide Complexes. *J. Therm. Anal. Cal.* **2000**, *61*, 119–125.

46. Gilles, J. Empirical Wavelet Transform. *Trans. Sig. Proc.* **2013**, *61*, 3999–4010.

47. Gilles, J.; Heal, K. A Parameterless Scale-Space Approach to find Meaningful Modes in Histograms — Application to Image and Spectrum Segmentation. *IJWMIP* **2014**, *12*, 1450044.

48. Gilles, J.; Tran, G.; Osher, S. 2D Empirical Transforms. Wavelets, Ridgelets, and Curvelets Revisited. *SIAM J Imaging Sci.* **2014**, *7*, 157–186.

49. Bui, K.; Fauman, J.; Kes, D.; Torres, L. Image Segmentation using Variational Methods and Wavelet Transforms. *unpublished*.

50. Bowmaker, G. A.; Kennedy, B. J.; Reid, J. C. Crystal Structures of AuCN and AgCN and Vibrational Spectroscopic Studies of AuCN, AgCN, and CuCN. *Inorg. Chem.* **1998**, *37*, 3968–3974.

51. Jobe, D. J.; Westaway, K. C. Fourier Transform Infrared Spectroscopy Studies of Cyanide Ion Solutions of Dimethylformamide and Aqueous Dimethylformamide. *Can. J. Chem.* **1993**, *71*, 1353–1361.

52. Hakkinen, H. The Gold-Sulfur Interface at the Nanoscale. *Nat. Chem.* **2012**, *4*, 443–455.

53. Beltramo, G. L.; Shubina, T. E.; Mitchell, S. J.; Koper, M. T. M. Cyanide Adsorption on Gold Electrodes: A Combined Surface Enhanced Raman Spectroscopy and Density Functional Theory Study. *J. Electroanal. Chem.* **2004**, *563*, 111–120.

54. Ulman, A. Formation and Structure of Self-Assembled Monolayers. *Chem. Rev.* **1996**, *96*, 1533–1554.

55. Max, P. B.; Scott, A. S.; Louis, J. A. The Infrared Spectra of Nitriles and Related Compounds Frozen in Ar and H_2O. *Astrophys. J* **1997**, *476*, 932.

56. Buffeteau, T.; Desbat, B.; Turlet, J. M. Polarization Modulation FT-IR Spectroscopy of Surfaces and Ultra-thin Films: Experimental Procedure and Quantitative Analysis. *App. Spec.* **1991**, *45*, 380–389.

57. Pettinger, B.; Picardi, G.; Schuster, R.; Ertl, G. Surface-Enhanced and STM Tip-Enhanced Raman Spectroscopy of CN^- Ions at Gold Surfaces. *J. Electroanal. Chem.* **2003**, *554–555*, 293–299.

58. Senapati, D.; Dasary, S. S. R.; Singh, A. K.; Senapati, T.; Yu, H.; Ray, P. C. A Label-Free Gold-Nanoparticle-Based SERS Assay for Direct Cyanide Detection at the Parts-per-Trillion Level. *Chem. Eur. J.* **2011**, *17*, 8445–8451.

59. Hautman, J.; Bareman, J. P.; Mar, W.; Klein, M. L. Molecular Dynamics Investigations of Self-Assembled Monolayers. *J. Chem. Soc. Faraday Trans.* **1991**, *87*, 2031–2037.

60. Frey, S.; Shaporenko, A.; Zharnikov, M.; Harder, P.; Allara, D. L. Self-Assembled Monolayers of Nitrile-Functionalized Alkanethiols on Gold and Silver Substrates. *J. Phys. Chem. B* **2003**, *107*, 7716–7725.

61. Neelakantan, P. Raman Spectrum of Acetonitrile. *Proc. Indian Acad. Sci. - Sect. A* **1964**, *60*, 422–424.

62. Kunimatsu, K.; Seki, H.; Golden, W. G.; Gordon, J. G.; Philpott, M. R. A Study of the Gold/Cyanide Solution Interface by In Situ Polarization-Modulated Fourier Transform Infrared Reflection Absorption Spectroscopy. *Langmuir* **1988**, *4*, 337–341.

63. Wang, X.-B.; Wang, Y.-L.; Yang, J.; Xing, X.-P.; Li, J.; Wang, L.-S. Evidence of Significant Covalent Bonding in $Au(CN)_2^-$. *J. Am. Chem. Soc.* **2009**, *131*, 16368–16370.

64. Bhimanapati, G. R.; Lin, Z.; Meunier, V.; Jung, Y.; Cha, J.; Das, S.; Xiao, D.; Son, Y.; Strano, M. S.; Cooper, V. R.; Liang, L.; Louie, S. G.; Ringe, E.; Zhou, W.; Kim, S. S.; Naik, R. R.; Sumpter, B. G.; Terrones, H.; Xia, F.; Wang, Y.; Zhu, J.; Akinwande, D.; Alem, N.;

Schuller, J. A.; Schaak, R. E.; Terrones, M.; Robinson, J. A. Recent Advances in Two-Dimensional Materials beyond Graphene. *ACS Nano* **2015**, *9*, 11509–11539.

65. Zhang, H. Ultrathin Two-Dimensional Nanomaterials. *ACS Nano* **2015**, *9*, 9451–9469.

66. Porath, D.; Millo, O.; Gersten, J. I. ScanningTunneling Microscopy Studies and Computer Simulations of Annealing of Gold Films. *J. Vac. Sci. Technol. B* **1996**, *14*, 30–37.

67. Mantooth, B. A. *Nanoscopic Analyses: Single Molecule Characterization in Molecular Electronics and Surface Science*. The Pennsylvania State University, University Park, PA **2004**.

CHAPTER 4:

Fourier Transform Infrared Scanning Tunneling Microscopy (FTIR-STM)

4.1 Introduction

The STM enables the probing of nanoscale events, but it is limited in the capability to provide chemical information on adsorbates.[1-4] The STM measures electronic and topographic information when a conductive probe tip is moved towards a conductive sample until the wave functions of the tip and the sample overlap.[1,2] The application of a bias well below the work function of the conductor enables electrons tunneling from the sample to the tip or vice versa. This current (*I*) is exponentially dependent on the tip–sample distance, z, and a characteristic decay constant, as shown in Equation 4.1.[1] Equation 4.1 indicates that there is approximately one order of magnitude tunneling current decrease for every 0.1 nm increase in the tip-sample distance based on typical work functions and decay constants. Thus, the exponential sensitivity to distance results in single–molecule to atomic resolution.[1] As an example, STM images have resolved surface morphologies of SAMs such as lattice structures, defect sites, and step edges.[2,4-8]

$$I = I_0 e^{-\gamma z} \qquad (4.1)$$

Molecular vibrations can reveal information about the electronic state and identity of a molecule, which can be used to understand single-molecule chemistry.[6,9-12] Characteristic frequencies can be used to identify functional groups and geometric isomers.[13,14] Since vibrations are sensitive to the environment, changes in measured spectra communicate intrinsic information on the system of interest,[15] i.e., transient states and kinetics.[16,17] Inelastic tunneling spectroscopy detects vibrational modes of molecules by the inelastic scattering of electrons from molecules, resulting in opening new tunneling channels and thereby increasing (or decreasing) tunneling current. This method is a STM-based single-molecule vibrational spectroscopy that requires low

temperatures (~4 K), ultrastable conditions, and has special selection rules, making it a technique with limited applicability.[18-23] On the other hand, vibrational spectroscopies, such as Raman and IR absorption, provide non-invasive, universal methods to probe specific chemical information, such as functional group identity.[15] Raman spectroscopy uses inelastic scattering of incident photons that excites or de-excites a molecular vibration. In the other technique, it is the absorption of a photon at IR wavelengths that excites a molecular vibration. However, the current spatial resolution of these vibrational spectroscopies is typically on the order of microns, which cannot resolve individual molecules.[6,9,12,13,16,24,25]

Similar to the STM tunneling current, the intensity of an evanescent field has an exponential dependence on the distance from an interface, Z (normal to the interface in the plane of incidence), associated with the penetration depth, d_p. These relationships are shown in Equations 4.2 and 4.3 and the penetration depth can be estimated by the skin depth.[26,27] The penetration depth for a thin gold film to an incident IR source with a 1 micron wavelength is estimated to be approximately 100 nm.[27-29] The advantage of the total internal reflection (TIR) configuration is the excitation from the back of the sample through an attenuated total reflection (ATR) crystal. This minimizes thermal effects on the tip such as expansion and drift, which are associated with direct irradiation.[1]

$$E = E_0 e^{-\alpha Z} \quad (4.2)$$

$$\propto = d_p^{-1} = \frac{2\pi}{\lambda}\sqrt{n_1^2 \sin^2\theta - n_2^2} \quad (4.3)$$

Here, we provide schematics and experimental design considerations for the development of an ambient, general method to measure single-molecule vibrations. As shown in Figure 4.1, a modified STM will be configured with total TIR geometry to enable infrared photon absorption through evanescent coupling in order to minimize the interaction with the STM probe tip. Total internal reflection geometry is described by Snell's Law, which defines a critical angle, θ_c, in terms of the ratio of the refraction indices n_1 and n_2 as in Equation 4.4. Beyond this critical angle, total internal reflection will occur and generate an evanescent field to excite molecules on the surface.[26]

$$\theta_c = \sin^{-1}\left(\frac{n_2}{n_1}\right) \quad (4.4)$$

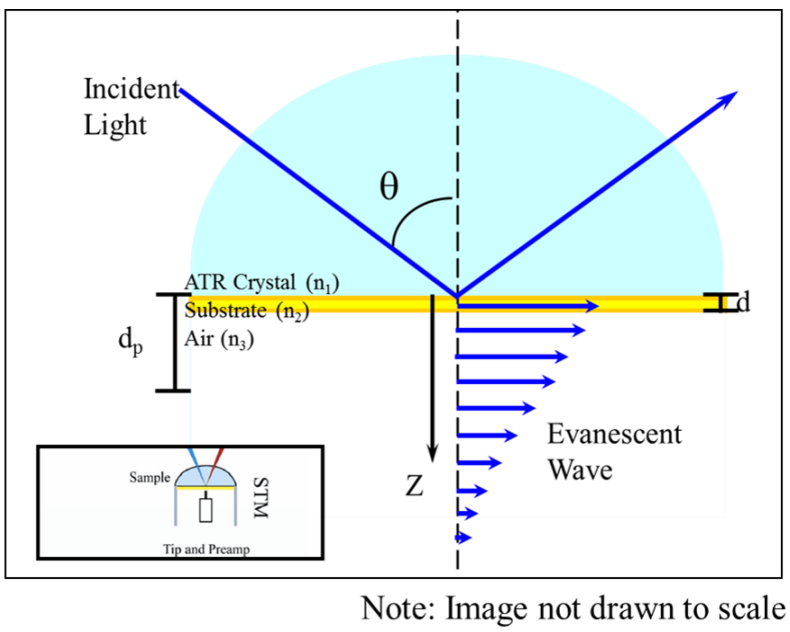

Figure 4.1. Configuration for total internal reflection geometry and parameters for estimating the critical angle and penetration depth. The inset shows how this arrangement avoids direct illumination of the scanning tunneling microscope probe tip.

4.2 Experimental Setup/Instrument Design

4.2.1. Optical Set-Up and Infrared Source

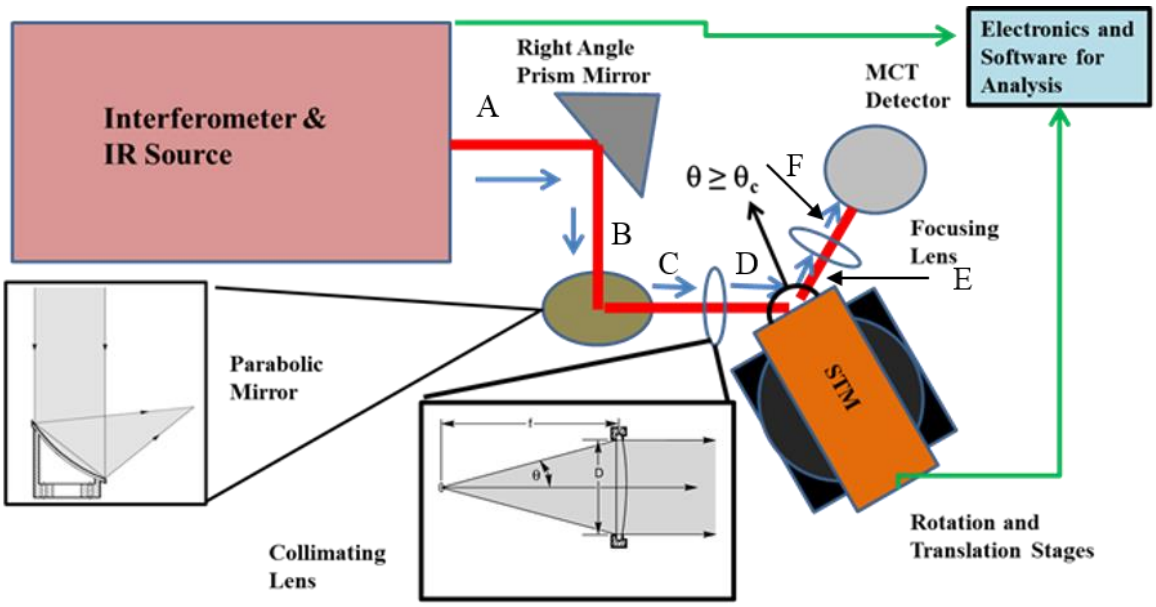

Figure 4.2. Optical set-up and components using an interferometer as the source and directing the light onto the sample loaded into a horizontal coarse-approach scanning tunneling microscope.

The complete optical design and experimental set-up for the instrument is shown in Figures 4.2 and 4.3. This set-up takes into consideration the rear illumination to minimize interaction with the STM probe tip and utilizes Fourier transform interferometry for rapid spectral acquisition (~1s) to minimize the effects of drift. Contributions to the tunneling current can be recorded in real time, and then mathematically transformed into the frequency domain. In this geometry, we utilize a combination of mirrors and lenses to collimate and focus the infrared light before it reaches the sample in Kreschmann-Raether attenuated total internal reflection geometry and is subsequently focused onto a mercury cadmium telluride (MCT) detector (Thermo-Fisher

Scientific, Waltham, MA). The molecules in the tunneling junction will be excited by the generated evanescent wave at the dielectric interface when the incident angle exceeds the critical angle (see Equation 4.4).

Table 4.1. Distances for the optical schematic shown in Figure 4.2. The critical angle for a sapphire prism substrate is given below the table.

Optical Path	Distance (cm) (±0.6 cm)
A	21.6
B	24.1
C	9.5
D	15.2
E	10.2
F	1.3

$$\boldsymbol{\theta} \geq \boldsymbol{\theta_c} = 34.6^{\mathbf{o}}$$

In more detail, the letters A-F in Figure 4.2 represent the optical path, starting from the IR source. The source is a Nicolet 6700 spectrometer (Thermo-Fisher Scientific) that delivers broadband spectral emission with an approximate range of 800–4000 cm^{-1}. An aluminum right angle prism mirror (Thorlabs Inc., Newton, NJ) reflects the IR light exiting the beam port of the interferometer 90° onto a 2" off-axis gold parabolic mirror (Thorlabs Inc.). At this point, the IR light is again reflected 90° towards focal point of the off-axis parabolic mirror which overlaps with the focal point of the first convex CaF_2 lens (Thorlabs Inc.) for collimation of the beam to the desired cross sectional area of ~1 cm^2. After focusing and collimation, the IR light is directed onto the sample at an angle exceeding the critical angle as required for the generation of the evanescent wave. In this particular case where the substrate is a gold coated sapphire prism, an incident angle

$\theta = 60° > \theta_c = 34.6°$ as measured from normal to the surface (critical angle calculated using n=1.76) is used.[30] After reflection from the rear of the sample, the IR light is collected and focused onto the MCT detector using another CaF_2 lens (Thorlabs, Inc.). All optical path distance A-F are summarized in Table 4.1.

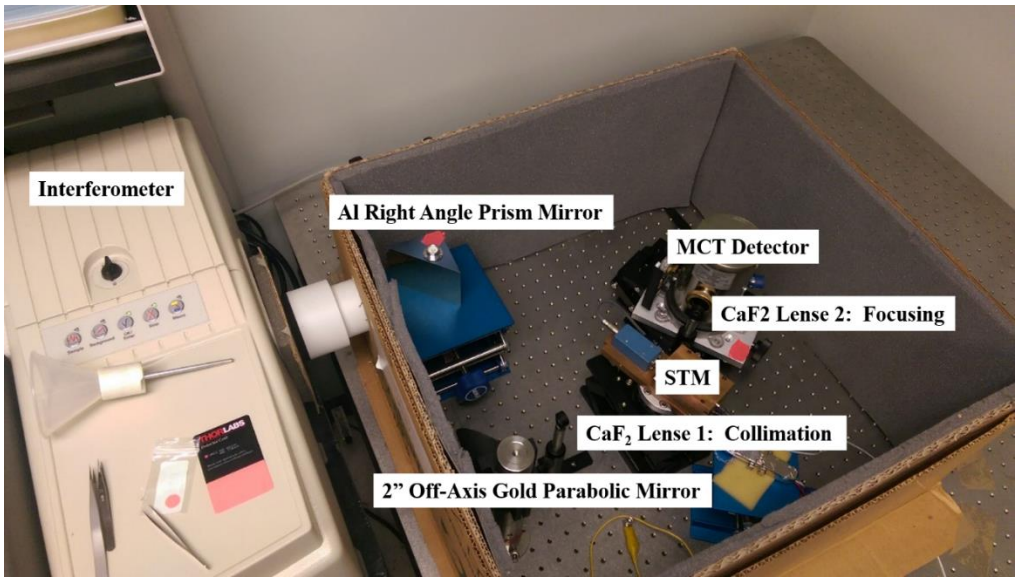

Figure 4.3. Photograph of the actual scanning tunneling microscope that matches the optical set up shown in Figure 4.2.

It is important to direct, to collimate, and to focus the infrared light from the FTIR interferometer before it reaches the sample that is housed in the horizontal coarse-approach STM. It is also optimal to minimize the number of components and keep the path length short to avoid complications that arise from beam dispersion. Chromatic aberration is another consideration, and a reason to use mirrors whenever possible. In the optical scheme shown in Figure 4.2, two mirrors and one lens are used prior to the incident beam reaching the sample. Collimation ensures that the rays of the incident beam are predominantly parallel, ensuring that the angle of incidence is as

accurate as possible for the entire light beam. This is a crucial component to ensure that the entire beam exceeds the critical angle and maximizes the optical intensity for the generated evanescent wave. The final lens focuses the reflected beam from the sample onto the detector to maximize the measured signal for spectral analysis and comparison with the signal measured by the STM probe tip. Figure 4.3 is a photograph of the actual instrument and optical set-up as described.

4.2.2. Optical Alignment with the Scanning Tunneling Microscope

Alignment of the STM and the incident IR light beam is crucial to ensuring the evanescent wave is generated in the region of the sample directly under the STM probe tip. To achieve this, the STM is mounted on a rotation stage (Newport Corp., Irvine, CA) where the pivot point is directly below the desired illumination point on the sample, which is aligned with STM probe tip. First, the STM is rotated such that the STM probe tip is perfectly aligned with the incoming IR light beam and this will be the 0° incident angle that is orthogonal to the surface (see inset in Figure 4.4). The visible red alignment laser from the interferometer should be illuminating the sample region directly in front of the STM probe tip. Next, adjust the rotation stage such that the angle of incidence is equal to, or greater than, the calculated critical angle (~35° for a sapphire prism substrate, 60° is used in the current set up and Figure 4 inset). If done correctly, the red alignment laser will illuminate the ATR prism as shown in the photograph in Figure 4.4. After alignment is complete, the second CaF_2 lens may need some slight adjustment to ensure the reflected beam is focused onto the MCT detector. The intensity of the reflected beam can be monitored using the accompanying OMNIC Software (Thermo-Fisher Scientific) for the interferometer.

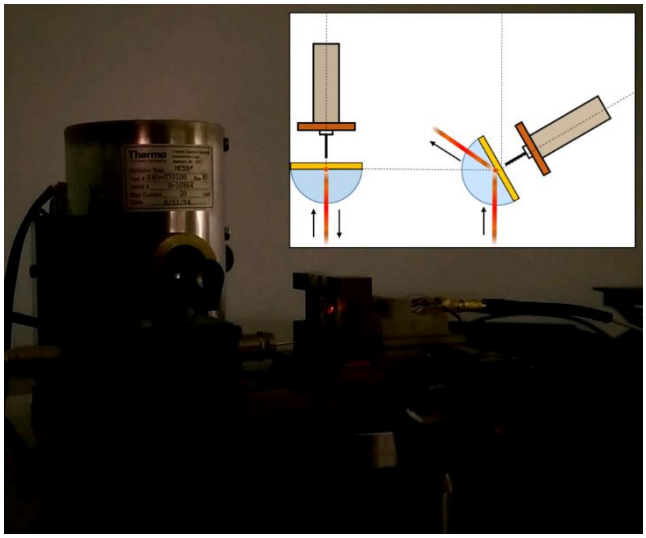

Figure 4.4. Photograph of the actual scanning tunneling microscope after alignment. The inset is a schematic illustrating the alignment procedure where the scanning tunneling microscope probe tip is in line with the incoming infrared light beam. The scanning tunneling microscope head is then rotated about the pivot point, which is the back sample location where the incident beam is reflected. An incident angle of 60° is used in this set up.

4.3 Instrument Design Schematics and Construction

4.3.1 Scanning Tunneling Microscope Exoskeleton and Coarse-Approach Head

The STM exoskeleton consists of a copper Faraday cage that serves to protect and to isolate the sensitive STM head, linear, coarse approach mechanism, and sample holder. The photograph in Figure 4.5 show this exoskeleton is mounted on another metal piece that serves as a holder/guide for the preamplifier and point of attachment to a micrometer precision rotational stage (Newport Corp.). Assembly of the STM exoskeleton is straightforward, only requiring the constructed components to be screwed together to form the complete unit measuring 6” × 2” × 3” (L × W × H).

In this design, the final assembly will enable easy optical access to the sample in a horizontal orientation in comparison to the typical vertical mechanism of our custom besocke style STM heads.

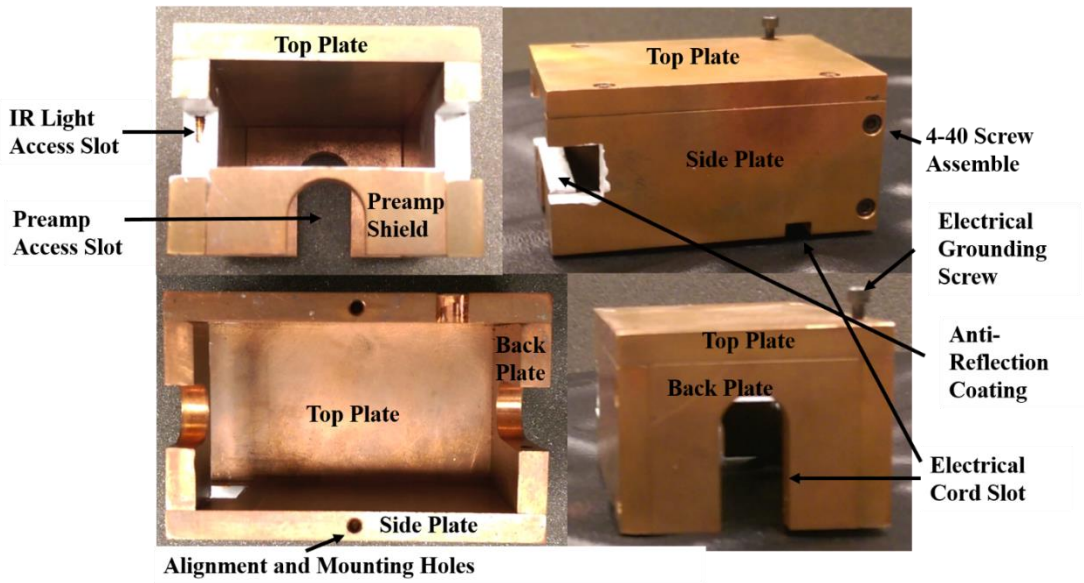

Figure 4.5. Photograph of the copper Faraday 'box' cover.

A copper 'box' top serving as the Faraday cage covers the entire STM head, fits on top of the bottom mounting plate, and uses the sample holder posts as guides. The exoskeleton is constructed from a copper top plate (2" × 3" × .25"), two side plates (1.25" × 3" × .25"), and a back plate (1.25" × 1.5" × .25") with cord slot, and a preamplifier copper shield. Three of the plates, the rear plate, and the front preamplifier shield are assembled using ¼" long, 4-40 socket head screws to assemble the copper 'box'. The 4th copper slab is used as the 'box' bottom to completely electronically isolate the STM head (the complete box top is shown in Figure 4.5) when connected to the common ground. A second cord slot is cut into the wall copper plate that is aligned with the connection points for the microslider coarse approach mechanism. Finally, two

rectangular copper posts with two milled slots serve to hold the plastic sample holder. One rectangular slot is milled parallel to the long axis of the copper posts to easily slide the sample holder into position (shown in Figure 4.6) and another rectangular slot is milled perpendicular to the post at the height of the ATR crystal/sample substrate to allow light to reach the sample.

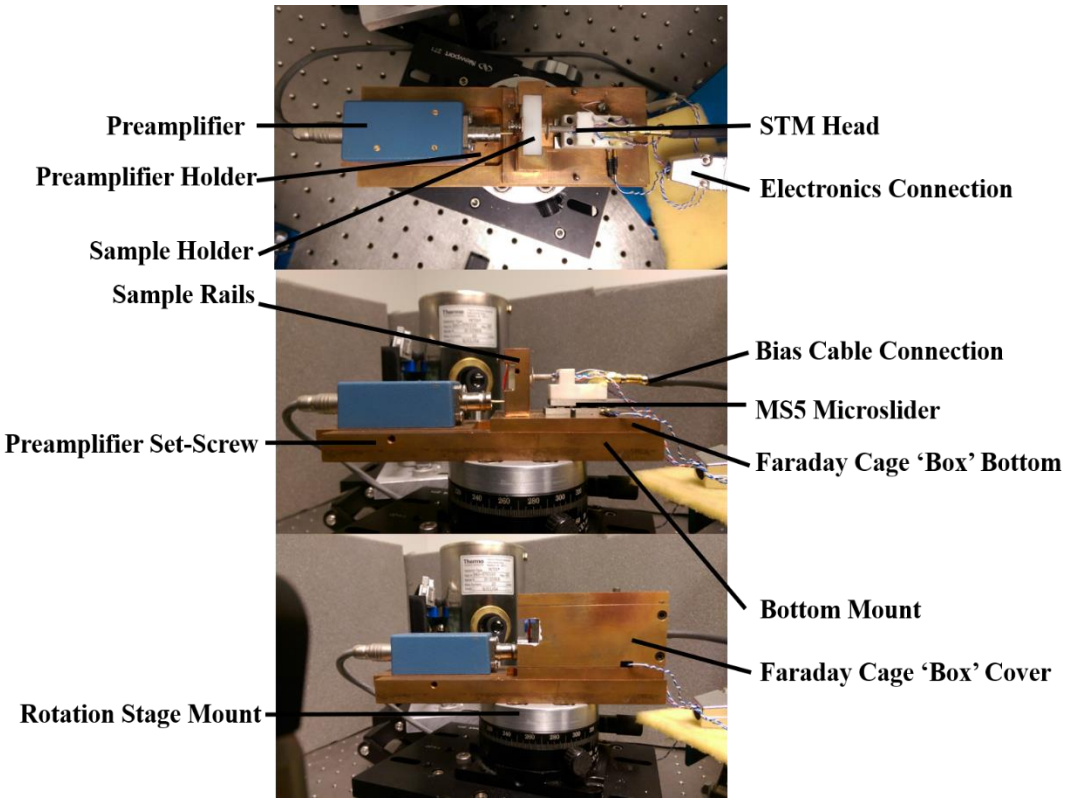

Figure 4.6. Photograph of the assembled scanning tunneling microscope exoskeleton attached to the bottom mount with preamplifier.

The entire copper exoskeleton is then mounted on a larger (6" × 2" × .5") rectangular copper plate using two steel dowel rods for alignment and attachment. This larger rectangular copper plate has a (1.5" × 6" × .25") pocket milled into one half for holding and guiding the preamplifier. A set screw is milled into the side of the bottom exoskeleton at the midpoint of the

pocket, and aligns with the copper plate (3" × 1.25" × .25") that holds the preamplifier for securement. The preamplifier used to measure the tunneling current is a high-gain transresistance amplifier IVP-300 (RHK Technology, Troy, MI), which provides a 10^9 V/A gain. In this manner, the preamplifier is isolated from environmental vibrations through direct coupling with the STM head and optical table. Electromagnetic noise that can be picked up by the spring loaded 'pin' attachment is isolated using a copper plate on the front of the Faraday 'box'. Some paint is used on the top of the preamp shield to prevent interference from scattered light. The entire exoskeleton, with STM head, is shown assembled in Figure 4.6 both, with and without, the copper 'box' top.

The horizontal, coarse approach STM head is shown in Figure 4.7 along with a schematic of the tip assembly. All of the STM head components are attached (Krazy Glue, Columbus, OH) to a Macor base (Corning Inc., Corning, NY), that serves as a mount on a single MS 5 Micro Piezo Slide (Omicron NanoTechnology GmbH, Taunusstein, Germany). The MS 5 Micro Piezo Slide has a maximum travel length of 5mm and can be tuned to have a step size between 40–400 nm. A maximum load-bearing capacities for the horizontal position, as used here, is 300 g. A piezoelectric scan tube (EBL Products, East Hartford, CT) supports the tip assembly and enables precise 3D movement of the STM probe tip. The custom-built tip assembly, commonly used in our laboratory,[5,31] consists of a copper grounding plate and two coaxial stainless steel syringe tubes (Small Parts, Miramar, Fl) separated by an insulating layer (Small Parts). The inner tube diameter (24-gauge is used here) must be large enough to allow the tip wire (Pt/Ir 80:20 wire, 0.25 mm diameter, Alfa Aesar, Ward Hill, MA) to be inserted. Typically, this inner syringe tube is and insulating layer is inserted into an 18-gauge syringe tube, which will be connected to the grounding plate to shield the bias signal and prevent capacitive coupling using silver epoxy and glued to a Macor piezoelectric cap. The inner syringe tube is then secured in place using a combination of

super glue and epoxy resin (Torr Seal, Varian Vacuum Technologies, Lexington, MA). Finally, the coaxial bias cable is inserted into the outer syringe tube such that the inner conductor connects to the inner syringe tube while the outer conductor is insulated from the inner tube and grounded to the outer syringe tube.

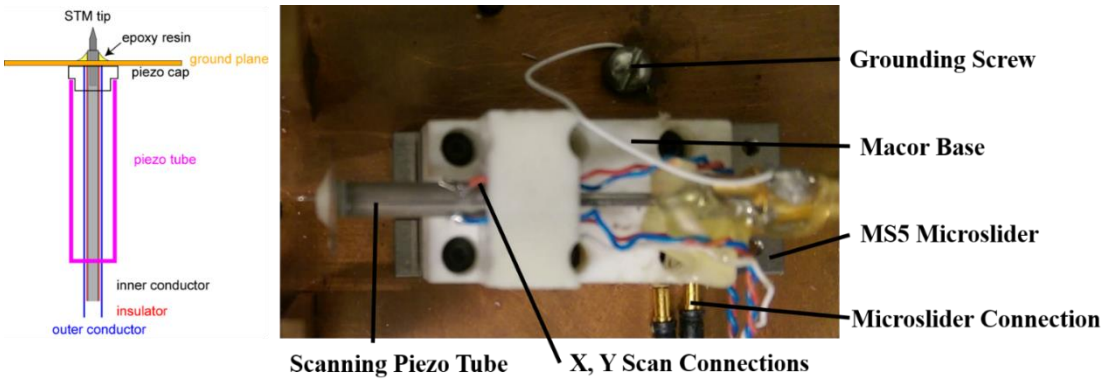

Figure 4.7. Photograph of the assembled scanning tunneling microscope head with schematic of the tip assembly.

4.3.2 Sample Holder

The custom sample holder is constructed from a piece of plastic with a window cut out for the prism substrate to enable access by the STM probe tip and the incident IR light beam. Figure 4.8 shows the rectangular piece of plastic, that measures in this orientation (1.25” × 1” × 0.3”), which is split into two parts, a top and bottom, that are held together by four plastic screws. In the interior, a piece of gold foil is used to make the electrical connection between the sample and the preamplifier. The prism is held in place with enough mechanical force to maintain conductivity by the spring-loaded prism holder. A piece of red paper lines the spring-loaded prism holder to prevent interference from scattered light from the incident infrared beam. The larger

circular pocket seen in the final panel in Figure 4.8 provides room for the copper grounding plate of the tip assembly to penetrate the sample holder enabling shorter tip lengths to be cut and used. The extra screw holes seen on the sides of the prism substrate are no longer in use, but were at one time used for a different prism attachment mechanism.

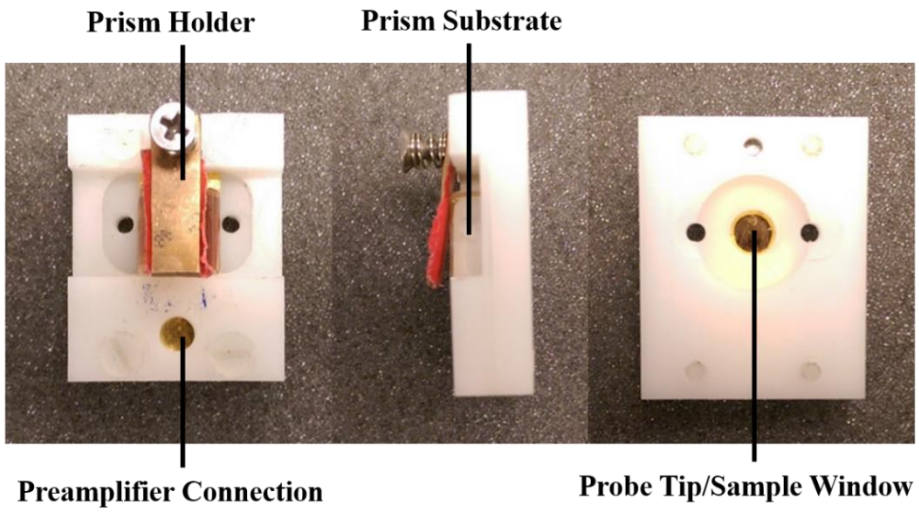

Figure 4.8. Photograph of the assembled scanning tunneling microscope prism sample holder.

4.3.3 Vibration and Acoustic Isolation

Environmental isolation, especially acoustic and vibration, is crucial to making single-molecule measurements. For the FTIR-STM, vibrational isolation is accomplished using an optical table with Gimbal Piston Isolators (TMC, Peabody, MA). Both the optical components and STM are directly screwed into the breadboard surface to minimize shifts in the optical alignment. The dampening mechanism of the optical table is enough to prevent vibrations from coupling into the STM current measurements.

Acoustic noise can also couple into the STM signal during scanning through the preamplifier connection point. In order to minimize interference, multiple layers of cardboard and foam material was used to create the walls and cover of the enclosure. This enclosure is modified to allow the flow of $N_2(g)$ for atmospheric purging, ports for electrical connections, and an entry path/window for the incident IR light beam from the interferometer. Nitrogen gas purging is required to increase the optical signal because atmospheric carbon dioxide and water readily absorb infrared light.[13] However, the enclosure is not perfectly sealed, which directly results in some acoustic noise penetration and purge gas leakage. A suggested improvement to increase the stability of the STM would be a commercial enclosure that can be purchased and customized from companies such as Herzan, LLC (www.herzan.com) or Eckel Industries (www.eckelusa.com).

4.3.4 Substrate and Sample Preparation

Molecular vibrations in ATR-FTIR spectroscopy are excited in sample through the generation of an evanescent wave at the interface. The critical angle, as determined by Snell's law (see Equation 4.2), indicates that the light beam must pass from a region of higher refractive index to a region of lower refractive index thus generating the evanescent wave in the material with a lower refractive index.[26] It is important to consider both, the refractive index of the material and the transmission window, along with the ability for the epitaxial growth of Au{111} on a substrate. There are several common materials that are used in commercial ATR-IR spectrometers including germanium, diamond, zinc selenide, silicon, calcium fluoride, and sapphire. Their respective transmission windows and indices of refraction for many of the most common optical materials are given in Table 4.2.[30] One of the most ideal substrates with the largest transmission windows is calcium fluoride, however, it is expensive and the epitaxial growth procedure for Au{111} has not

been fully optimized.[32] Temporarily, sapphire prisms have been chosen as the ATR substrate due to the fact that the epitaxial growth of Au{111} has been demonstrated with sufficient transmission in the spectral range of interest for cyanide (~3–5 μm wavelength).[33]

Table 4.2. Transmission windows and refractive indices for common infrared attenuated total reflection crystals (ref 30).

ATR Crystal	Transmission Window	Refractive Index (at 4 micron wavelength)
Germanium	2.0 micron - 16.0 micron	4
Zinc Selenide	600 nm - 16 micron	2.7
Sapphire	150 nm - 4.5 micron	1.7
Calcium Fluoride	180 nm - 8.0 micron	1.4
Silicon	1.2 micron - 8 micron	3.4
Diamond	230 nm - 20 micron	2.4

4.4 Data Acquisition and Signal Processing

Light from the interferometer is broadband and intense enough to interact with molecules on the sample surface while enabling collection within a sufficiently fast time period (typically 1–2 s). Spectral acquisition on the order of 0.5 s is necessary as the measurement will be complicated by the thermal drift of the STM probe tip in an ambient environment. Only half of the full power from the Nicolet 6700 FTIR spectrometer (Thermo-Fisher Scientific) will reach the sample without the use of filters or grating, and the interferometer itself acts as a frequency modulator.

Collection of data by the STM probe tip must be done in evenly spaced discrete intervals (Δx) and initially synchronized with the zero path difference (ZPD, Δx=0) of the interferometer mirror. The movement of the mirror is directly linked to the output intensities through the constructive and deconstructive interference of all the frequencies at each data collection step. In this manner, the Fast Fourier transform (FFT) can be used to mathematically transform the recorded spectrum as a function of mirror position, and not time.

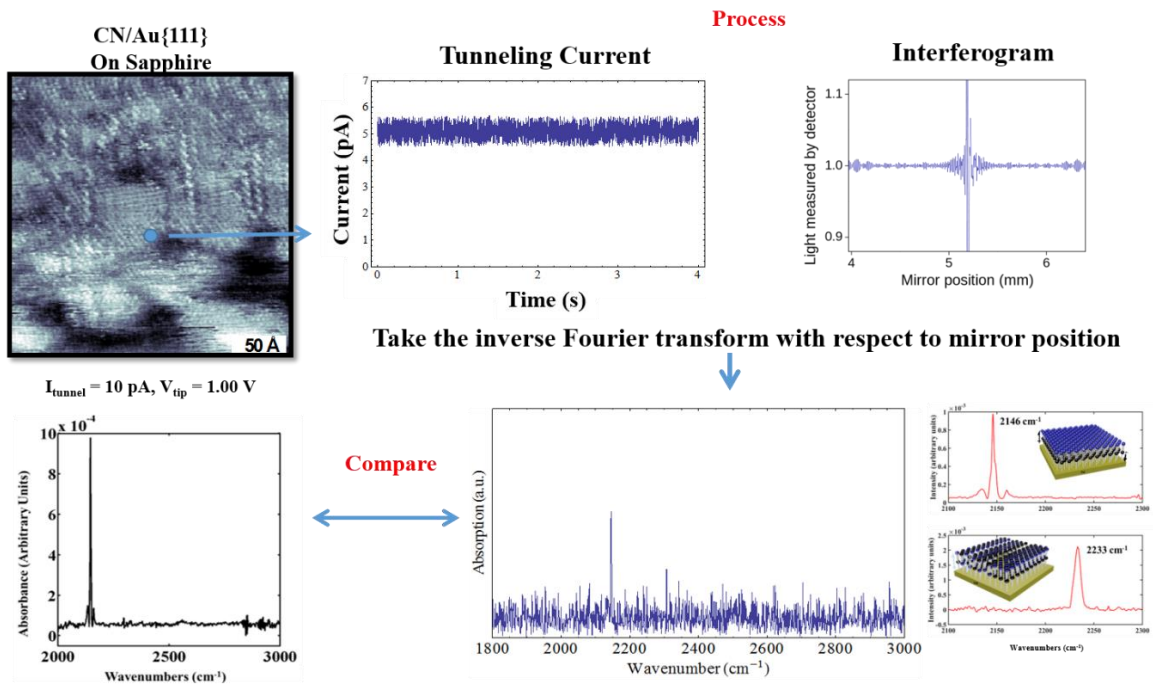

Figure 4.9. A schematic of the process to obtain the scanning tunneling microscope image and record spectra for a single molecule. Collection of the tunneling current must be synchronized with the zero-point difference and sample collection points of the spectrometer. Then fast Fourier transform mathematics can be used to generate the frequency spectrum collected by the probe tip for comparison with the simultaneously acquired infrared spectra.

For the Nicolet 6700 spectrometer (Thermo-Fisher Scientific), as is common in most commercial spectrometers, a HeNe laser is used to trigger and to synchronize data collection. Thus mirror retardation, and resolution, is directly related to the HeNe laser 632 nm wavelength with each ZPD occurring at exactly half of the wavelength. In order to synchronize data acquisition of the STM with the interferometer it is essential to gain access to the signals through the external ports on the interferometer (labeled "TAKE DATA" and "SAMPLE CLOCK" using the remote signal accessory (Thermo-Fisher Scientific). The current control electronics and software are the same as others currently used in our lab while the MATLAB code to perform the measurements is provided elsewhere.[34] A schematic of the experimental process and scheme is shown in Figure 4.9. This process starts with image acquisition by the STM followed by point spectroscopy over a molecule of interest, then the subsequent processing of the signal using an inverse FFT to generate the frequency spectrum for comparison with the simultaneously acquired ATR-FTIR spectrum.

4.5 Results and Discussion

A prototype STM has been developed that directs IR light from an FTIR spectrometer to a sample in an ATR configuration. We have demonstrated, as shown in Figure 4.10, that it is possible to simultaneously record infrared spectra of a surface while imaging with molecular resolution. Cyanide is a small molecule that can form stable monolayers on Au{111} at room temperature[35] and the CN bond vibration is in a relatively barren region of the IR spectrum where it is easily identified and tracked in an open atmosphere,[36] which makes it ideal for further instrument development. There are several places for improvement on the prototype such as substrate (ATR prism) material and improving environmental isolation (vibration, electromagnetic, and acoustic). The next steps to enhancing the STM and developing the capabilities for room temperature

single-molecule vibrational spectroscopy is to manipulate the electronic environment (sample bias/voltage) of CN/Au{111}, monitor the infrared spectrum, and test whether the STM probe tip is able to detect the activated surface vibrational modes.

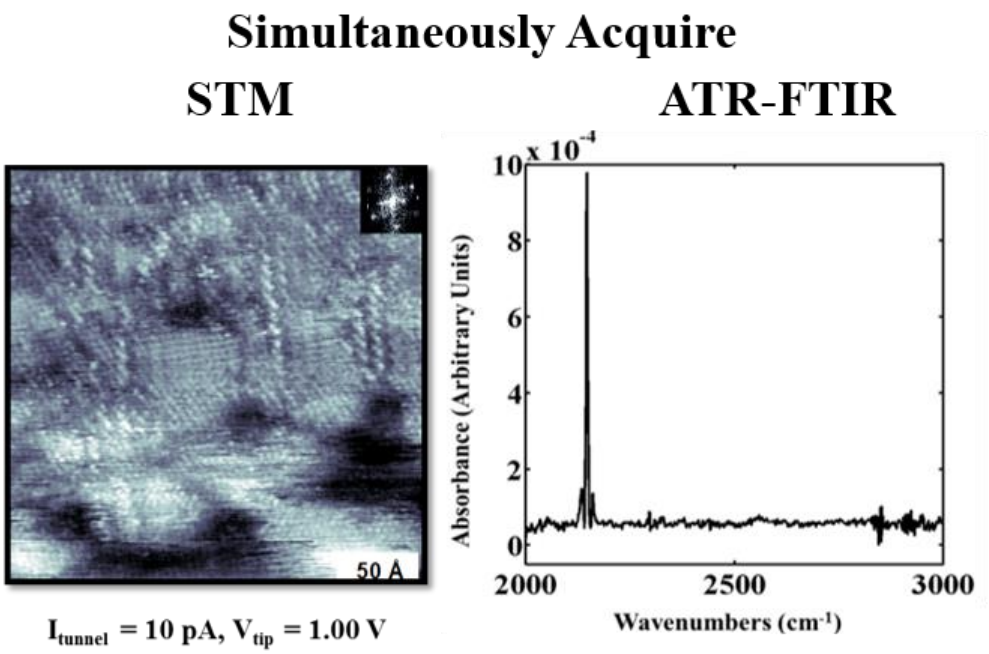

Figure 4.10. Scanning tunneling microscope image and simultaneously acquired attenuated total reflection Fourier transform infrared spectrum of as-deposited CN/Au{111}/Sapphire acquired by the prototype Fourier transform infrared scanning tunneling microscope.

The goal of the FTIR-STM is to develop a more generally applicable, room temperature single molecule vibrational technique enhancing the capabilities of the scanning tunneling microscope. Cyanide has shown to be an ideal small-molecule probe for this type of experiment because it is a relatively simple molecule with a strong dipole moment.[37] In addition, it has been shown to form stable, room temperature monolayers on Au{111} where it is oriented normal to

the substrate surface.[35] The surface orientation is a critical component since the STM probe tip will only detect contributions to the tunneling current that occur due to changes in the tip-sample separation distance.

The CN vibration has been shown to be influenced by the local electronic environment[38] and is predicted to have a vibration resonance with the electronic surface states of Au{111}. Published reports have shown vibration intensity changes and peak shifts with an applied voltage,[38] along with low temperature inelastic tunneling spectroscopy revealing a 'dip' at the frequency location of the CN vibration.[11,39] An analogous experiment using the prototype instrument where spectra are recorded by the STM probe tip at different applied sample bias is expected to yield interesting results.

The coupling of the sensitivity of the CN vibration to the local electronic environment with possible surface enhancements on the order of 10^2 to 10^6 can lead to detectable changes in the tunneling current.[40-43] If we assume that the change in tunneling current with the surface enhancement is similar to that reported in IETS, then we would expect approximately a 4-8% change in tunneling current intensity. Thus, for typical tunneling currents between 1 and 10 pA we could expect the current intensity to change from 0.04 to 0.8 pA. However, the lifetime of an activated vibration is on the order of 10^{-12},[44] and based on the current preamplifier bandwidth of 10^{-3} s, we would need many excitations of a single molecule to detect the signal.

4.6. Summary and Outlook

We have discussed the design and operation of the Fourier transform infrared scanning tunneling microscope, which aims to integrate the chemical information found molecular vibrations with the nanoscale electronic and topographic information of STM. In addition, we have

proposed design of the prototype component schematics, instrument assembly, and method for signal detection. Although we have demonstrate that the FTIR–STM is fully capable of achieving molecular resolution and acquiring infrared spectra, there is room for improvement. For example, there is a need for an improved enclosure for environmental isolation that would increase stability and further reduce acoustic and electromagnetic interference. In addition, a better ATR prism substrate would reduce IR light attenuation, but will require a new method for the epitaxial growth of Au{111}. The inclusion of these technical improvements, along with a software embedded drift control, would enable more stable probing of surface-mediated and intermolecular interactions.

4.7 References

1. Chen, C. J. *Introduction to Scanning Tunneling Microscopy*. OUP Oxford: **2008**.

2. Claridge, S. A.; Schwartz, J. J.; Weiss, P. S. Electrons, Photons, and Force: Quantitative Single-Molecule Measurements from Physics to Biology. *ACS Nano* **2011**, *5*, 693–729.

3. Bonnell, D. A.; Basov, D. N.; Bode, M.; Diebold, U.; Kalinin, S. V.; Madhavan, V.; Novotny, L.; Salmeron, M.; Schwarz, U. D.; Weiss, P. S. Imaging Physical Phenomena with Local Probes: From Electrons to Photons. *Rev. Mod. Phys.* **2012**, *84*, 1343–1381.

4. Claridge, S. A.; Liao, W.-S.; Thomas, J. C.; Zhao, Y.; Cao, H. H.; Cheunkar, S.; Serino, A. C.; Andrews, A. M.; Weiss, P. S. From the Bottom Up: Dimensional Control and Characterization in Molecular Monolayers. *Chem. Soc. Rev.* **2013**, *42*, 2725–2745.

5. Bumm, L. A.; Arnold, J. J.; Charles, L. F.; Dunbar, T. D.; Allara, D. L.; Weiss, P. S. Directed Self-Assembly to Create Molecular Terraces with Molecularly Sharp Boundaries in Organic Monolayers. *J. Am. Chem. Soc.* **1999**, *121*, 8017–8021.

6. Dunbar, T. D.; Cygan, M. T.; Bumm, L. A.; McCarty, G. S.; Burgin, T. P.; Reinerth, W. A.; Jones, L.; Jackiw, J. J.; Tour, J. M.; Weiss, P. S.; Allara, D. L. Combined Scanning Tunneling Microscopy and Infrared Spectroscopic Characterization of Mixed Surface Assemblies of Linear Conjugated Guest Molecules in Host Alkanethiolate Monolayers on Gold. *J. Phys. Chem. B* **2000**, *104*, 4880–4893.

7. Monnell, J. D.; Stapleton, J. J.; Jackiw, J. J.; Dunbar, T.; Reinerth, W. A.; Dirk, S. M.; Tour, J. M.; Allara, D. L.; Weiss, P. S. Ordered Local Domain Structures of Decaneselenolate and Dodecaneselenolate Monolayers on Au{111}. *J. Phys. Chem. B.* **2004**, *108*, 9834–9841.

8. Weiss, P. S. Functional Molecules and Assemblies in Controlled Environments: Formation and Measurements. *Acc. Chem. Res.* **2008**, *41*, 1772–1781.

9. Hoffmann, H.; Mayer, U.; Brunner, H.; Krischanitz, A. Reflection-Absorption Infrared Spectroscopy of Self-Assembled Monolayers on Gold and Silicon Surfaces. *Vib. Spec.* **1995**, *8*, 151–157.

10. Rosenbaum, A. W.; Freedman, M. A.; Darling, S. B.; Popova, I.; Sibener, S. J. Surface Vibrations in Alkanethiol Self-Assembled Monolayers of Varying Chain Length. *J. Chem. Phys.* **2004**, *120*, 3880–3886.

11. Michael, G.; Mark, A. R.; Abraham, N. Molecular Transport Junctions: Vibrational Effects. *J. Phys.: Condens. Matter* **2007**, *19*, 103201.

12. Jiang, N.; Foley, E. T.; Klingsporn, J. M.; Sonntag, M. D.; Valley, N. A.; Dieringer, J. A.; Seideman, T.; Schatz, G. C.; Hersam, M. C.; Van Duyne, R. P. Observation of Multiple Vibrational Modes in Ultrahigh Vacuum Tip-Enhanced Raman Spectroscopy Combined with Molecular-Resolution Scanning Tunneling Microscopy. *Nano Lett.* **2012**, *12*, 5061–5067.

13. Siebert, F.; Hildebrandt, P. *Vibrational Spectroscopy in Life Science*. Wiley: **2008**.

14. Shuster, M. J.; Vaish, A.; Gilbert, M. L.; Martinez-Rivera, M.; Nezarati, R. M.; Weiss, P. S.; Andrews, A. M. Comparison of Oligo(ethylene glycol)alkanethiols versus n-Alkanethiols: Self-Assembly, Insertion, and Functionalization. *J. Phys. Chem. C* **2011**, *115*, 24778–24787.

15. Elliott, A. B. S.; Horvath, R.; Gordon, K. C. Vibrational Spectroscopy as a Probe of Molecule-Based Devices. *Chem. Soc. Rev.* **2012**, *41*, 1929–1946.

16. Zheng, Y. B.; Payton, J. L.; Chung, C.-H.; Liu, R.; Cheunkar, S.; Pathem, B. K.; Yang, Y.; Jensen, L.; Weiss, P. S. Surface-Enhanced Raman Spectroscopy to Probe Reversibly Photoswitchable Azobenzene in Controlled Nanoscale Environments. *Nano Lett.* **2011**, *11*, 3447–3452.

17. Zheng, Y. B.; Payton, J. L.; Song, T.-B.; Pathem, B. K.; Zhao, Y.; Ma, H.; Yang, Y.; Jensen, L.; Jen, A. K. Y.; Weiss, P. S. Surface-Enhanced Raman Spectroscopy To Probe Photoreaction Pathways and Kinetics of Isolated Reactants on Surfaces: Flat versus Curved Substrates. *Nano Letters* **2012**, *12*, 5362–5368.

18. Kirtley, J.; Scalapino, D. J.; Hansma, P. K. Theory of Vibrational Mode Intensities in Inelastic Electron Tunneling Spectroscopy. *Phys. Rev. B* **1976**, *14*, 3177–3184.

19. Knochenmuss, R. Theory of Inelastic Electron Tunneling Intensities which Includes a Nonconstant Barrier Potential. *Phys. Rev. B* **1986**, *33*, 7998–8004.

20. Stipe, B. C.; Rezaei, M. A.; Ho, W. Single-Molecule Vibrational Spectroscopy and Microscopy. *Science* **1998**, *280*, 1732–1735.

21. Stipe, B. C.; Rezaei, M. A.; Ho, W. Localization of Inelastic Tunneling and the Determination of Atomic-Scale Structure with Chemical Specificity. *Phys. Rev. Lett.* **1999**, *82*, 1724–1727.

22. Stipe, B. C.; Rezaei, M. A.; Ho, W. A Variable-Temperature Scanning Tunneling Microscope Capable of Single-Molecule Vibrational Spectroscopy. *Rev. Sci. Instrum.* **1999**, *70*, 137–143.

23. Hipps, K. W.; Mazur, U. Inelastic Electron Tunneling Spectroscopy. In *Handbook of Vibrational Spectroscopy*, John Wiley & Sons, Ltd: **2006**.

24. Max, P. B.; Scott, A. S.; Louis, J. A. The Infrared Spectra of Nitriles and Related Compounds Frozen in Ar and H_2O. *Astrophys. J* **1997**, *476*, 932.

25. Joo, S.-W.; Kim, W.-J.; Yun, W. S.; Hwang, S.; Choi, I. S. Binding of Aromatic Isocyanides on Gold Nanoparticle Surfaces Investigated by Surface-Enhanced Raman Scattering. *App. Spec.* **2004**, *58*, 218–223.

26. Axelrod, D.; Thompson, N. L.; Burghardt, T. P. Total Internal Reflection Fluorescent Microscopy. *J. Microsc.* **1983**, *129*, 19–28.

27. Takashi, W.; Kento, A. Penetration-Depth Characteristics of Evanescent Fields at Metal Attenuated Total Reflection. *Jpn. J. Appl. Phys.* **2005**, *44*, 4272.

28. Gilberd, P. W. The Anomalous Skin Effect and the Optical Properties of Metals. *J. Phys. F.* **1982**, *12*, 1845.

29. Qiang, R.; Chen, R. L.; Chen, J. Modeling Electrical Properties of Gold Films at Infrared Frequency Using FDTD Method. *Int. J. Infrared Milli.* **2004**, *25*, 1263–1270.

30. Basic Properties of Several of the Most Ubiquitous Optical Materials. In *Photonics.com*, Photonics Media: **2011**.

31. Mantooth, B. A. *Nanoscopic Analyses: Single Molecule Characterization in Molecular Electronics and Surface Science*. The Pennsylvania State University, University Park, PA **2004**.

32. Semaltianos, N. G.; Wilson, E. G. Investigation of the Surface Morphology of Thermally Evaporated Thin Gold Gilms on Mica, Glass, Silicon and Calcium Fluoride Substrates by Scanning Tunneling Microscopy. *Thin Solid Films* **2000**, *366*, 111–116.

33. Kästle, G.; Boyen, H. G.; Koslowski, B.; Plettl, A.; Weigl, F.; Ziemann, P. Growth of Thin, Flat, Epitaxial (1 1 1) Oriented Gold Films on C-Cut Sapphire. *Surf. Sci.* **2002**, *498*, 168–174.

34. Saavedra, H. M. *Controlling Adsorbate Interactions for Advanced Chemical Patterning*. Pennsylvania State University, University Park, PA, **2010**.

35. Guttentag, A.; Wächter, T.; Barr, K.; Abendroth, J. M.; Song, T.-B.; Yang, Y.; Allara, D. L.; Zharnikov, M.; Weiss, P. S. Precious Poision: The Self-Assembly of Cyanide on Au{111}. *unpublished* **2016**.

36. Keedy, C. R. The Rotational-Vibrational Spectra of HCN and DCN: A Physical Chemistry Experiment. *J. Chem. Educ.* **1992**, *69*, A296.

37. Iguchi, K. Dipole Moment of the HCN Molecule. *J. Chem. Phys.* **1956**, *25*, 217–219.

38. Kunimatsu, K.; Seki, H.; Golden, W. G.; Gordon, J. G.; Philpott, M. R. A Study of the Gold/Cyanide Solution Interface by In Situ Polarization-Modulated Fourier Transform Infrared Reflection Absorption Spectroscopy. *Langmuir* **1988**, *4*, 337–341.

39. Bayman, A.; Hansma, P. K.; Kaska, W. C. Shifts and Dips in Inelastic-Electron-Tunneling Spectra Due to the Tunnel-Junction Environment. *Phys. Rev. B* **1981**, *24*, 2449–2455.

40. Müller, F.; Müller, A.-D.; Meissner, O.; Heilmann, A.; Hietschold, M. Enhanced Local Surface Conductivity Measurements by Scanning Tunneling Microscopy. *Rev. Sci. Instrum.* **1997**, *68*, 3104–3107.

41. Krishnan, A.; Thio, T.; Kim, T. J.; Lezec, H. J.; Ebbesen, T. W.; Wolff, P. A.; Pendry, J.; Martin-Moreno, L.; Garcia-Vidal, F. J. Evanescently Coupled Resonance in Surface Plasmon Enhanced Transmission. *Optics Communications* **2001**, *200*, 1–7.

42. Pettinger, B.; Picardi, G.; Schuster, R.; Ertl, G. Surface-Enhanced and STM Tip-Enhanced Raman Spectroscopy of CN^- Ions at Gold Surfaces. *J. Electroanal. Chem.* **2003**, *554–555*, 293–299.

43. Lenner, M.; Rácz, P.; Dombi, P.; Farkas, G.; Kroó, N. Field Enhancement and Rectification of Surface Plasmons Detected by Scanning Tunneling Microscopy. *Phys. Rev. B* **2011**, *83*, 205428.

44. Forsblom, M.; Persson, M. Vibrational Lifetimes of Cyanide and Carbon Monoxide on Noble and Transition Metal Surfaces. *J. Chem. Phys.* **2007**, *127*, 154303.

CHAPTER 5:

Conclusions and Prospects

5.1 Summary

In the previous chapters, we described the adsorption of cyanide on Au{111} as a system ideal for the development of room-temperature single-molecule vibrational spectroscopy. We utilized the nanoscale resolution of the STM along with chemical information from both Raman and infrared spectroscopic techniques to characterize surface structure at the single-molecule level. It was elucidated that the system is well behaved, oriented normal to the surface, and exhibits a strong electronic coupling with the gold substrate. Following the structural and vibrational characterization of the as-deposited cyanide monolayers on Au{111}, we demonstrated that we can change the structure both physically and chemically through a dry annealing process. The new structure maintains the normal orientation of the cyanide molecules, but is proposed to change from an all Au-CN bonding scheme to a mixed composition of Au-CN and Au-NC bound molecules through a process similar to the crystallization of solid AuCN. Next, we presented the schematics for a prototype FTIR-STM, which couples IR light with the STM in an ATR configuration to minimize the interaction of the electromagnetic radiation with the STM probe tip. In this configuration, molecules on the surface are excited though an evanescent wave generated at the sample surface when the incident angle meets or exceeds the critical angle. We demonstrate that the prototype FTIR-STM has the ability to image, in space and time, a surface with molecular resolution and simultaneously to acquire vibrational spectra. We then outline the experiment to advance the instrument utilizing FFT mathematics to convert the measured signal from the STM probe tip and synchronized with the FTIR spectrometer to generate the analogous frequency spectrum. This chapter is a summary of the work presented in this dissertation, and briefly describes future experiments that can build off these results.

5.2 Single-Molecule Vibrational Spectroscopy of Cyanide on Au{111}

Cyanide has a predicted resonance between its stretching vibration and the electronic surface states of Au{111} that we have desired to probe in order to increase our understanding of the interactions between molecular vibrations and molecular electronic structure. The strong dipole moment of cyanide[1] coupled with the strength of electronic coupling with the Au{111} surface[2,3] and sensitivity of the CN vibration to the local electronic environment[4,5] support this prediction. Previous IETS experiments have reported agreement between the detected energy of the CN vibration with the IR frequency, but showed it as a 'dip' in the IETS spectrum.[6,7] In the past, we have previously tried to assemble cyanide on the surface through the deposition of cyanogen (C_2N_2) only to discover that it does not dissociate upon adsorption.[8] In chapter 2, we present a new method to form cyanide monolayers on Au{111} that are stable at room temperature where atmospheric O_2 and H_2O react with HCN(g) in a manner similar to the well-known gold cyanidation reaction. The demonstration that this process forms stable, ordered monolayers of CN on Au{111} provides a way to perform the vibrational spectroscopy experiments. Results from these experiments can then be used to guide the development of the room-temperature single-molecule spectroscopy and to enable comparisons that will advance our understanding of the effect of temperature on interaction between molecular vibrations and electronic structure.

5.3 Crystal Growth

The strength of the Au-C bond is slightly stronger than the Au-S and Au-Se bonds.[9-13] In all of these systems, the reconstruction of the bare Au{111} surface is observed through the formation of single-atom deep vacancy islands that are attributed to the 'lifting' of gold adatoms

during monolayer formation.[3,10,13-15] In comparison, the formation of two different apparent heights in the cyanide monolayers, which are not observed in the thiolate and selenolate systems on Au{111} are an indication of the formation of multiple layers on the surface.[3] The bonding between gold atoms in gold-cyanide complexes have been observed to exhibit 'relativistic' effects resulting in larger, 3.4–3.8 Å, spacing than the traditional 2.89 Å close-packed arrangement in Au{111}.[16,17] This spacing has been measured in crystalline AuCN, which is composed of hexagonally bundled, linear AuCN chains[16] and is the measured lattice spacing for cyanide monolayers on Au{111} in chapter 2. It is expected that longer exposure to HCN(g) will result in the formation of crystals on the surface that can undergo a similar change through the thermal annealing process described in chapter 3. It should be noted that the "relativistic" effects of the Au-Au bonding, significant covalent properties of the Au-CN bonding, and strong dipole moment of cyanide are attributed to novel electrical and optical properties of the crystal.[18]

5.4 Surface Polymerization

The vibrational characterization of CN/Au{111} presented in chapters 2 and 3 indicated that the bonding with gold is a similar chemical state to when it is a nitrile functional group in organic molecules.[19,20] Both HCN(g) and acetonitrile are examples of cyanide forms that easily undergo polymerization.[21-23] In some of these cases, the polymer is conductive, and cyanide is sometimes used as an ingredient in the fabrication of 2D conductive carbon nitride nanomaterials.[24] The results presented in this work demonstrate the potential for cyanide surface polymerization as a novel method to fabricate a conductive surface coating. Graphene, the atomically thin conductive material, has been proposed for a wide range of potential applications for conductive 2D nanomaterials.[25,26]

Another type of polymerization is possible that leverages the known affinity of cyanide for transition metals.[27,28] The coordination of cyanide to the iron found in our body's hemoglobin prevents the sequestering of oxygen and is the primary reason for its lethality to humans. In more useful ways, cyanide coordination chemistry has been used to bridge molecular assemblies to create large molecular frameworks.[17,29] It is possible that the use of appropriate transition metal coordination chemistry can induce the growth of similar frameworks orthogonal to the surface. It has been demonstrated that AuCN chains are conductive and can serve as a sort of molecular 'wire'.[30]

5.5 Conclusions

This work in this dissertation directly shows that CN bonds strongly to the gold surface facilitating efficient electron transfer to the substrate. Cyanide monolayers are reactive, which we show by changing the structure through an annealing process and generating a mixed chemical state similar to AuCN crystallization. The self-assembly of cyanide on Au{111} has the potential, through the use of coordination chemistry, to become a route to creating conductive nanomaterials and building larger molecular frameworks. Combining this system with the prototype FTIR-STM, which has been shown to have the capability to image with molecular resolution and to acquire infrared spectra simultaneously demonstrates the potential of this system for developing single-molecule vibrational spectroscopy at room temperature.

5.6 References

1. Iguchi, K. Dipole Moment of the HCN Molecule. *J. Chem. Phys.* **1956**, *25*, 217–219.

2. Zangmeister, C. D.; Robey, S. W.; van Zee, R. D.; Kushmerick, J. G.; Naciri, J.; Yao, Y.; Tour, J. M.; Varughese, B.; Xu, B.; Reutt-Robey, J. E. Fermi Level Alignment in Self-Assembled Molecular Layers: The Effect of Coupling Chemistry. *J. Phys. Chem. B* **2006**, *110*, 17138–17144.

3. Guttentag, A.; Wächter, T.; Barr, K.; Abendroth, J. M.; Song, T.-B.; Yang, Y.; Allara, D. L.; Zharnikov, M.; Weiss, P. S. Precious Poision: The Self-Assembly of Cyanide on Au{111}. *unpublished* **2016**.

4. Kunimatsu, K.; Seki, H.; Golden, W. G.; Gordon, J. G.; Philpott, M. R. A Study of the Gold/Cyanide Solution Interface by In Situ Polarization-Modulated Fourier Transform Infrared Reflection Absorption Spectroscopy. *Langmuir* **1988**, *4*, 337–341.

5. Forsblom, M.; Persson, M. Vibrational Lifetimes of Cyanide and Carbon Monoxide on Noble and Transition Metal Surfaces. *J. Chem. Phys.* **2007**, *127*, 154303.

6. Bayman, A.; Hansma, P. K.; Kaska, W. C. Shifts and Dips in Inelastic-Electron-Tunneling Spectra Due to the Tunnel-Junction Environment. *Phys. Rev. B* **1981**, *24*, 2449–2455.

7. Michael, G.; Mark, A. R.; Abraham, N. Molecular Transport Junctions: Vibrational Effects. *J. Phys.: Condens. Matter* **2007**, *19*, 103201.

8. Han, P.; Sykes, E. C. H.; Pearl, T. P.; Weiss, P. S. A Comparative Scanning Tunneling Microscopy Study of Physisorbed Linear Quadrupolar Molecules: C_2N_2 and CS_2 on Au{111} at 4 K. *J. Phys. Chem. A* **2003**, *107*, 8124–8129.

9. Beltramo, G. L.; Shubina, T. E.; Mitchell, S. J.; Koper, M. T. M. Cyanide Adsorption on Gold Electrodes: A Combined Surface Enhanced Raman Spectroscopy and Density Functional Theory Study. *J. Electroanal. Chem.* **2004**, *563*, 111–120.

10. Love, J. C.; Estroff, L. A.; Kriebel, J. K.; Nuzzo, R. G.; Whitesides, G. M. Self-Assembled Monolayers of Thiolates on Metals as a Form of Nanotechnology. *Chem. Rev.* **2005**, *105*, 1103–1170.

11. Hakkinen, H. The Gold-Sulfur Interface at the Nanoscale. *Nat. Chem.* **2012**, *4*, 443–455.

12. Crudden, C. M.; Horton, J. H.; Ebralidze, I. I.; Zenkina, O. V.; McLean, A. B.; Drevniok, B.; She, Z.; Kraatz, H.-B.; Mosey, N. J.; Seki, T.; Keske, E. C.; Leake, J. D.; Rousina-Webb, A.; Wu, G. Ultra Stable Self-Assembled Monolayers of N-Heterocyclic Carbenes on Gold. *Nat Chem* **2014**, *6*, 409–414.

13. Ossowski, J.; Wächter, T.; Silies, L.; Kind, M.; Noworolska, A.; Blobner, F.; Gnatek, D.; Rysz, J.; Bolte, M.; Feulner, P.; Terfort, A.; Cyganik, P.; Zharnikov, M. Thiolate versus Selenolate: Structure, Stability, and Charge Transfer Properties. *ACS Nano* **2015**, *9*, 4508–4526.

14. Ulman, A. Formation and Structure of Self-Assembled Monolayers. *Chem. Rev.* **1996**, *96*, 1533–1554.

15. Monnell, J. D.; Stapleton, J. J.; Jackiw, J. J.; Dunbar, T.; Reinerth, W. A.; Dirk, S. M.; Tour, J. M.; Allara, D. L.; Weiss, P. S. Ordered Local Domain Structures of Decaneselenolate and Dodecaneselenolate Monolayers on Au{111}. *J. Phys. Chem. B.* **2004**, *108*, 9834–9841.

16. Bowmaker, G. A.; Kennedy, B. J.; Reid, J. C. Crystal Structures of AuCN and AgCN and Vibrational Spectroscopic Studies of AuCN, AgCN, and CuCN. *Inorg. Chem.* **1998**, *37*, 3968–3974.

17. Katz, M. J.; Sakai, K.; Leznoff, D. B. The Use of Aurophilic and Other Metal-Metal Interactions as Crystal Engineering Design Elements to Increase Structural Dimensionality. *Chem. Soc. Rev.* **2008**, *37*, 1884–1895.

18. Li, R.; Kobayashi, H.; Tong, J.; Yan, X.; Tang, Y.; Zou, S.; Jin, J.; Yi, W.; Fan, J. Radical-Involved Photosynthesis of AuCN Oligomers from Au Nanoparticles and Acetonitrile. *J. Am. Chem. Soc.* **2012**, *134*, 18286–18294.

19. Max, P. B.; Scott, A. S.; Louis, J. A. The Infrared Spectra of Nitriles and Related Compounds Frozen in Ar and H_2O. *Astrophys. J* **1997**, *476*, 932.

20. Zharnikov, M. Probing Charge Transfer Dynamics in Self-Assembled Monolayers by Core Hole Clock Approach. *J. Electron. Spectrosc. Relat. Phenom.* **2015**, *200*, 160–173.

21. Gause, E. H.; Montgomery, P. D. Hydrogen Cyanide Stability and Heat of Polymerization. *J. Chem. Eng. Data* **1960**, *5*, 351–354.

22. Oikawa, E.; Mori, K.; Saito, G. The Polymerization of Acetonitrile in the Presence of Acidic and Basic Substances. *Bull. Chem. Soc. Jpn.* **1966**, *39*, 1182–1185.

23. He, C.; Lin, G.; Upton, K. T.; Imanaka, H.; Smith, M. A. Structural Investigation of HCN Polymer Isotopomers by Solution-State Multidimensional NMR. *J. Phys. Chem. A* **2012**, *116*, 4751-4759.

24. Chattopadhyay, S.; Ganguly, A.; Chen, K.-H.; Chen, L.-C. One-Dimensional Group III-Nitrides: Growth, Properties, and Applications in Nanosensing and Nano-Optoelectronics. *Crit. Rev. Solid State Mater. Sci.* **2009**, *34*, 224–279.

25. Zhang, H. Ultrathin Two-Dimensional Nanomaterials. *ACS Nano* **2015**, *9*, 9451–9469.

26. Bhimanapati, G. R.; Lin, Z.; Meunier, V.; Jung, Y.; Cha, J.; Das, S.; Xiao, D.; Son, Y.; Strano, M. S.; Cooper, V. R.; Liang, L.; Louie, S. G.; Ringe, E.; Zhou, W.; Kim, S. S.; Naik, R. R.; Sumpter, B. G.; Terrones, H.; Xia, F.; Wang, Y.; Zhu, J.; Akinwande, D.; Alem, N.; Schuller, J. A.; Schaak, R. E.; Terrones, M.; Robinson, J. A. Recent Advances in Two-Dimensional Materials beyond Graphene. *ACS Nano* **2015**, *9*, 11509–11539.

27. Dehnicke, K. The Chemistry of Cyano Complexes of the Transition Metals. Organometallic Chemistry - A Series of Monographs. Von A. G. Sharpe. Academic Press, London-New York-San Francisco 1976. 1. Aufl., XI, 302 S., geb. £ 10.40. *Angew. Chem.* **1976**, *88*, 774–774.

28. Ahmad, S. The Chemistry of Cyano Complexes of Gold(I) with Emphasis on the Ligand Scrambling Reactions. *Coord. Chem. Rev.* **2004**, *248*, 231–243.

29. Hu, M.; Belik, A. A.; Imura, M.; Yamauchi, Y. Tailored Design of Multiple Nanoarchitectures in Metal-Cyanide Hybrid Coordination Polymers. *J. Am. Chem. Soc.* **2013**, *135*, 384–391.

30. Lee, W. C.; Kim, K.; Park, J.; Koo, J.; Jeong, H. Y.; Lee, H.; Weitz, D. A.; Zettl, A.; Takeuchi, S. Graphene-Templated Directional Growth of an Inorganic Nanowire. *Nat. Nano* **2015**, *10*, 423–428.

Appendix

A.1 Chapter 3 Supplemental Image Analysis

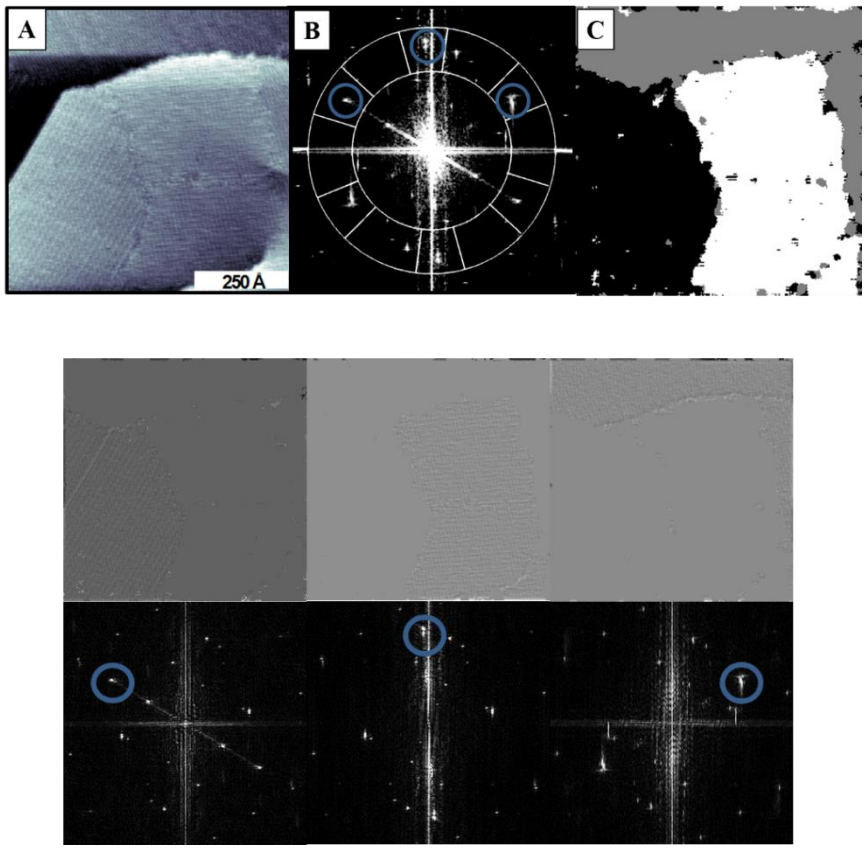

Figure A1. (A) Scanning tunneling microscope image, (B) associated manual curvelet partitioning of the Fourier domain using the empirical wavelet transformation, and (C) the segmentation results for the domains with different orientations. The bottom panels represent the manual 2D fast Fourier transformation filtering of the circled Fourier coefficients and the corresponding image textures for each segmented domain. Relative stripe domain rotation angles are calculated to be multiples of 60° using the dot product of the displacement vectors of the position of the circled coefficients from the origin. Only one of the Fourier coefficients was used for each segmented texture region because of symmetry in the Fourier domain. The Fourier domain plots takes into account all information in the image.

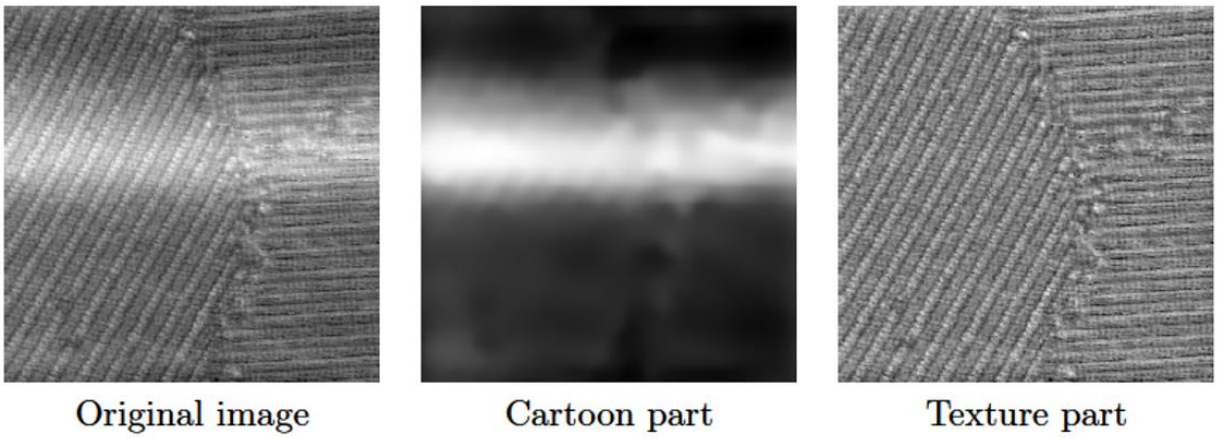

Figure A2. Scanning tunneling microscope image segmented using a combination of cartoon and texture decomposition. Artifacts associated with the imaging were separated from the analyzed image and stored separately to avoid loss of information.

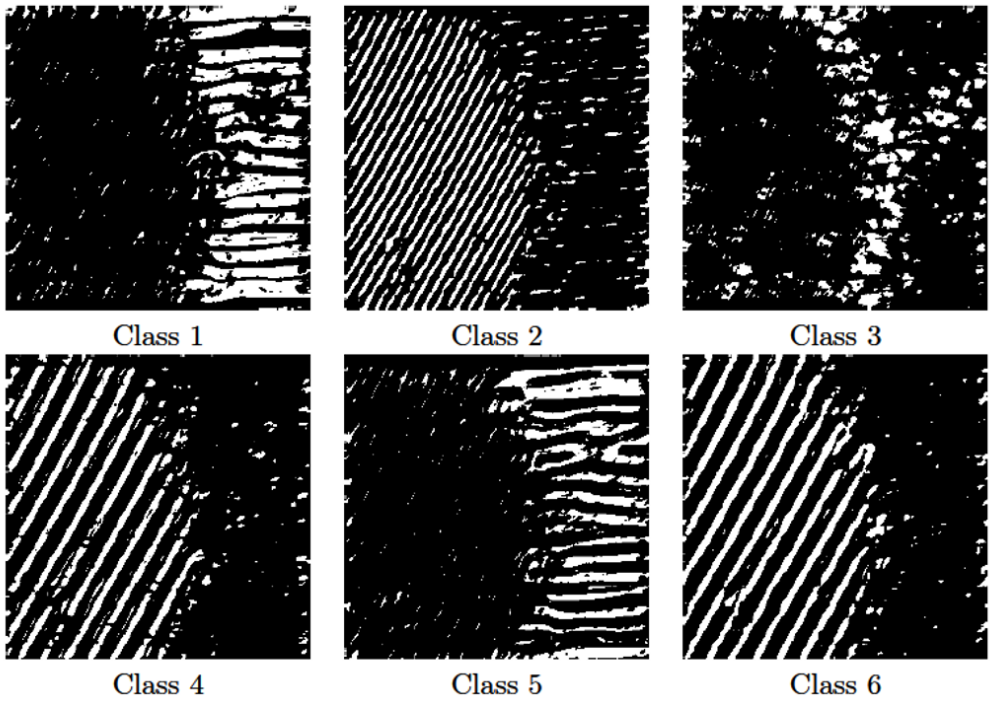

Figure A3. Classes associated with the texture decomposition of the scanning tunneling microscope image shown in Figure A2 that highlight the different regions of the image associated with the ribbon orientation and domain boundary.

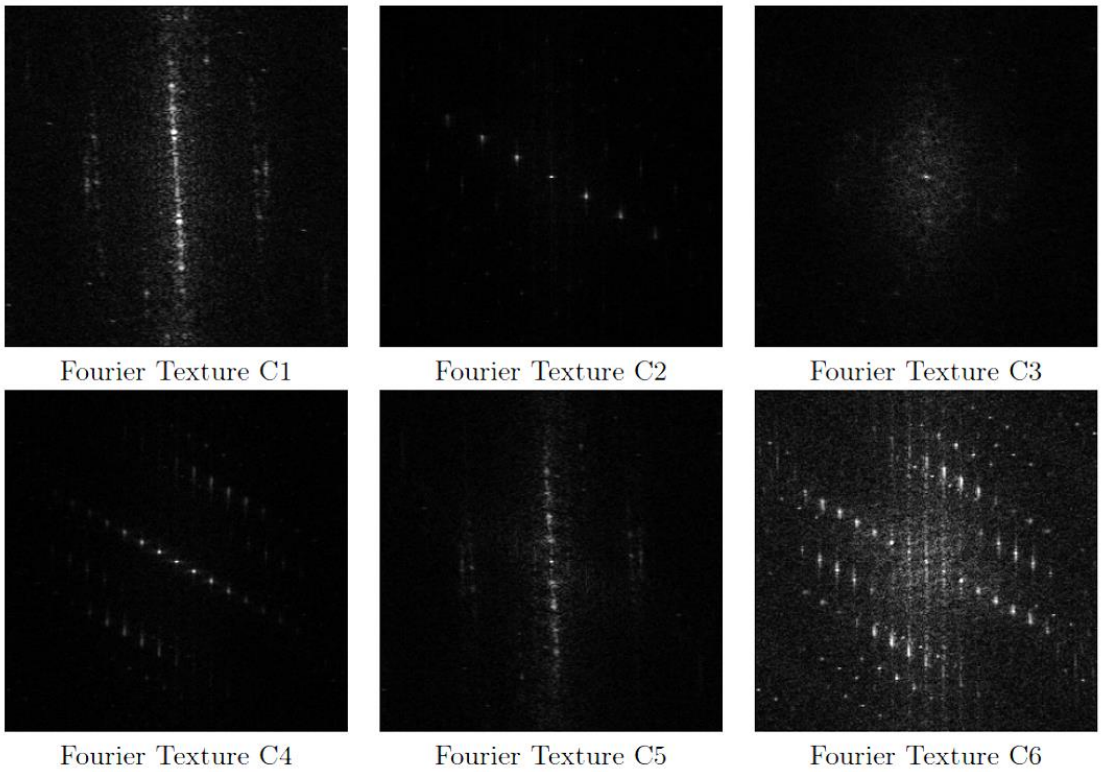

Figure A4. Fourier domain classes associated with the texture decomposition of the scanning tunneling microscope image shown in Figure A2. The angles between different orientation domains, as shown in Figure A1, were calculated using the dot product of the displacement vectors from the farthest and largest Fourier coefficient from the origin. Fourier textures C1 and C2 are examples that represent the two stripe orientation domains, Class 1 and Class 6, highlighted in Figure A3. Equivalently, the Fourier textures from C4 and C5 could be used to calculate the same angle.

A.2 Chapter 3 Supplemental Infrared Spectroscopy

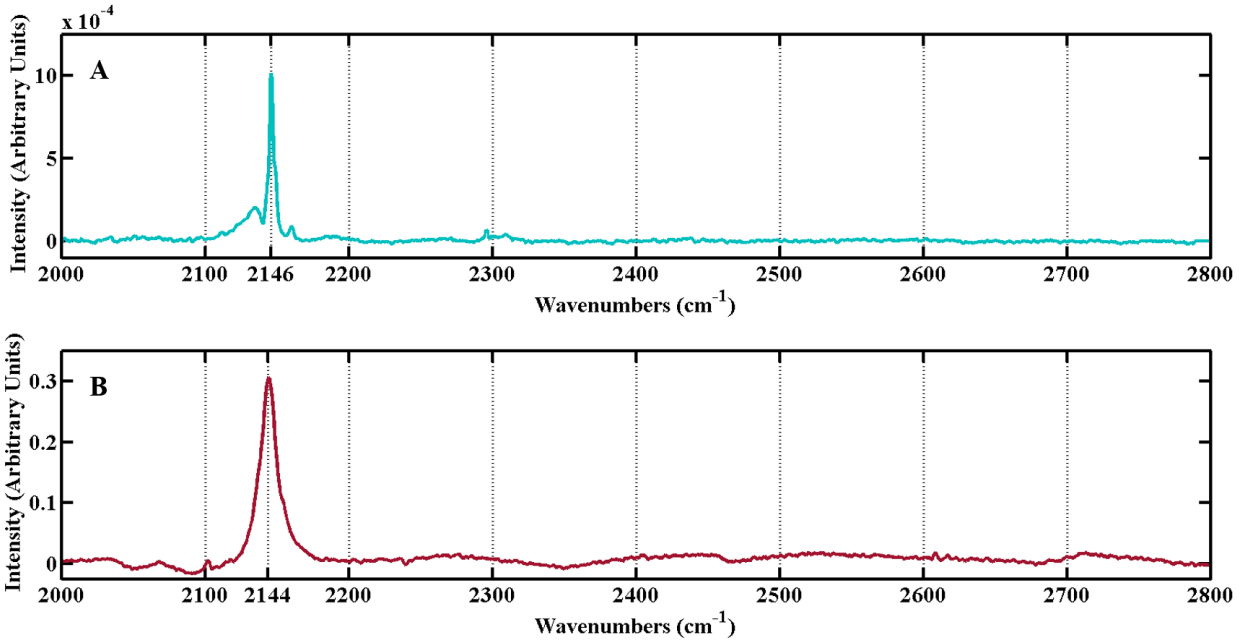

Figure A5. (A) Attenuated total reflection-infrared spectrum of as-adsorbed CN/Au{111} at room temperature. (B) Polarization-modulation infrared absorption spectrum of room temperature as-deposited CN/Au/Si.

A.3 Chapter 3 Supplemental Raman Spectroscopy

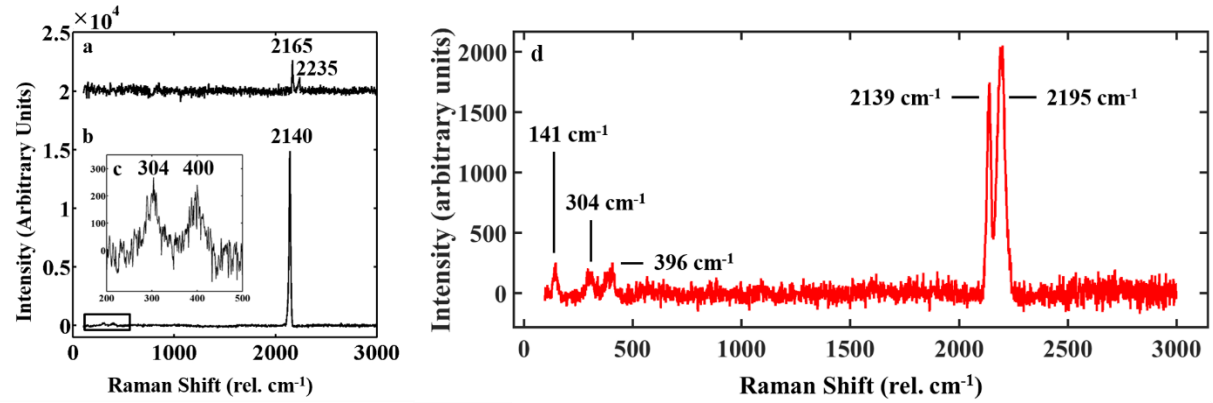

Figure A6. (a) Surface-enhanced Raman spectrum of as-adsorbed CN/Au{111} at room temperature showing the peaks attributed to the CN vibrations. On the Au{111} surface we were unable to detect the low frequency modes, but did detect a splitting of the CN vibration. (b) Surface-enhanced Raman spectrum of as-adsorbed CN on a custom roughened polycrystalline Au substrate on glass with the low frequency vibrations attributed to the Au-CN stretch and bend (shown in the inset, c). (d) Surface-enhanced Raman spectrum of CN on Au after annealing using the same custom polycrystalline nanostructured SERS substrate. (As-deposited Raman spectra shown in (a, b, and c) are reproduced from chapter 2.)

Raman spectra for the as-deposited and annealed cyanide on gold systems are shown in Figure A6. The splitting of the high frequency peak on the as-deposited CN/Au{111}, shown in Figure A6a, are similar to the vibrations for the annealed CN sample. The 2195 and 2235 cm^{-1} are close to the values reported for the crystalline high frequency vibration, while the lower 2140 and 2165 cm^{-1} are closer to the reported value for cyanide adsorbed on the surface of gold. It is unknown why the Au{111} value is shifted by 25 cm^{-1}. We do not observe the CN vibration at a

lower frequency for the weaker Au-NC vibration. In the spectra for the annealed CN we detected the additional low-frequency mode at 141 cm^{-1} that is close to the Au-N vibration detected in crystalline AuCN. One explanation for the observation of the mode on the Au{111} surface is that the single-crystal face enables greater packing and order that results in some stochastic 'flipping' of the cyanide from exposure to the thermal energy at room temperature. (see ref A5 for the AuCN crystalline vibration characterization and ref A6 for the as-adsorbed CN on Au)

A.4 Chapter 3 Supplemental AuCN Crystallographic Data

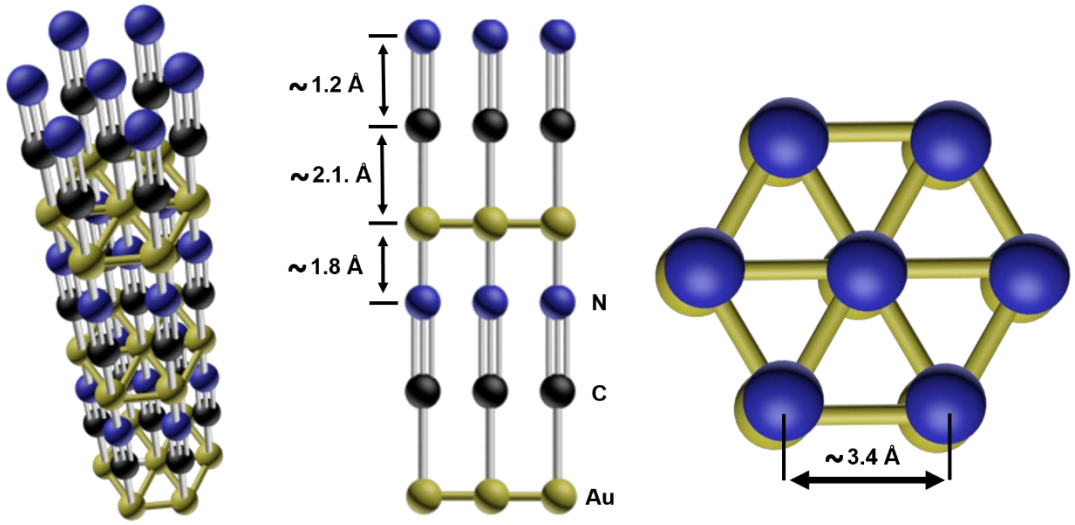

Figure A7. Schematic of the crystal structure and distance measurements for solid AuCN, which is composed of hexagonally bundled, linear AuCN chains with alternating Au-C and Au-N bonds (distances from ref. A5).

A.5 References

A1. Gilles, J. Empirical Wavelet Transform. *Trans. Sig. Proc.* **2013**, *61*, 3999–4010.

A2. Gilles, J.; Tran, G.; Osher, S. 2D Empirical Transforms. Wavelets, Ridgelets, and Curvelets Revisited. *SIAM J. Imaging Sci.* **2014**, *7*, 157–186.

A3. Gilles, J.; Heal, K. A Parameterless Scale-Space Approach to find Meaningful Modes in Histograms — Application to Image and Spectrum Segmentation. *IJWMIP* **2014**, *12*, 1450044.

A4. Bui, K.; Fauman, J.; Kes, D.; Torres, L. Image Segmentation Using Variational Methods and Wavelet Transforms. *unpublished*.

A5. Bowmaker, G. A.; Kennedy, B. J.; Reid, J. C. Crystal Structures of AuCN and AgCN and Vibrational Spectroscopic Studies of AuCN, AgCN, and CuCN. *Inorg. Chem*. **1998**, *37*, 3968–3974.

A6. Senapati, D.; Dasary, S. S. R.; Singh, A. K.; Senapati, T.; Yu, H.; Ray, P. C. A Label-Free Gold-Nanoparticle-Based SERS Assay for Direct Cyanide Detection at the Parts-per-Trillion Level. *Chem. Eur. J.* **2011**, *17*, 8445–8451.